Hydrogen incorporation mechanisms and diffusion of hydrous defects and silicon ions in olivine: the major rock-forming mineral of the Earth's upper mantle

A THESIS

SUBMITTED TO THE FACULTY OF THE GRADUATE SCHOOL

OF THE UNIVERSITY OF MINNESOTA

BY

Yang (Will) Li

IN PARTIAL FULFILLMENT OF THE REQUIREMENTS

FOR THE DEGREE OF

DOCTOR OF PHILOSOPHY

David L. Kohlstedt

December, 2015

Acknowledgements

I am grateful to a number of people that have been helping me through my Ph.D. study in the last few years. Without their great help, I could have not accomplished the present thesis study at the University of Minnesota.

The first person I would like to thank is my advisor Professor David L. Kohlstedt. I could not think of a better advisor than David. He has provided me with every opportunity to teach me how to do scientific work. Through his constantly encouraging and professional guidance, I had the privilege of doing cutting-edge researches collaborating with famous researchers from all over the world. His rigorous scholarship and creative characters in science have greatly impacted me. I am very grateful that David spent countless time discussing with me about our study and offering comments for the thesis. Most importantly, I have learned from him the characters of being humble, curious, and brave to the challenges of science.

I would also like to express my special thanks to the collaborators for the studies present in this thesis: Dr. Stephen J. Mackwell, director of Lunar and Planetary Institute; Professor Sumit Charkraborty and Dr. Ralf Dohmen from Ruhr University Bochum, Germany; Dr. John Craven

from the University of Edinburgh; Dr. Brian Monteleone from Woods Hole Oceanographic Institution. Without their instructions and discussions on instrumental measurements and analyses, I could not have obtained correct measurements nor finished the researches for the results.

My gratitude also goes to my graduate study committee: Professor Marc M. Hirschmann, Professor Justin S. Revenaugh, Professor Donna L. Whitney, Professor Christian Teyssier. Thanks them for the dedication of being as my committee for the written, oral qualifying exams, and my thesis defense. They have driven me through the graduate study and offered a number of valuable comments and suggestions.

I would also like to present my gratitude to Dr. Mark E. Zimmerman, Professor Tony Withers, Dr. Jed Mosenfelder, Dr. Shenghua Mei, Professor Yonghong Zhao for teaching me how to do experiments with their great experience and expertise. Without their instructions, I could not have managed to conduct experiments in the right ways. I strongly thank them for their patient coaching for experiments and spending time supervising me doing researches.

I also need to thank all the colleagues and visiting scholars to the lab for having discussions and helping me in various ways: Dr. Jacob Tielke, Dr. Matej Pec, Dr. Alejandra Quintanilla, Dr. Chao Qi, Dr. Miki Tasaka, Dr. Ayako Suzuki, Dr. Lars Hansen, Dr. Hongluo Zhang, Amanda Dillman, Cameron Meyers, Zhou (Johnny) Zhang, Professor Junfeng Zhang, Professor Yongfeng Wang, Professor Wuming Bai, Jiaying Yang, Guinan Zhang. I have always felt that it is my great fortune that I can work and study in such a lab that everyone is always willing to help without expecting anything in return and, more importantly, we all work as a team.

I am also grateful to my roommates and friends for offering great support when I felt frustrated

about research and for bringing countless pleasure to my life in Minnesota. In addition, I would like to thank my family members for being supportive. With their loving care and encouragement, I have had a tremendous experience in the last few years.

In addition, I would like to thank the University of Minnesota and the School of Earth Science for offering me the opportunity of studying here. I also want to thank NSF for funding the research projects, and the people that offered the following fellowships: Samuel Goldich Footsteps fellowship, V. Rama Murthy/Janice Noruk fellowship, John Gruner fellowship.

Above all of these, I thank God for bringing these great people and great experiences through my Ph.D. study. I feel truly blessed and have gained much more than I could have ever imaged.

Contents

List of Tables

List of Figures

Chapter 1

Introduction

1.1 Background

The physical and chemical properties of the upper portion of Earth's mantle play a key role in the geophysical, geochemical, and geodynamic processes from the deep portion of the mantle to the crust on the Earth's surface. Olivine and its high-pressure polymorphs (wadsleyite and ringwoodite) constitute up to $\sim 60\%$ by average volume proportion ranging from the MOHO down to the transition zone (e.g., *Jackson*, 2000). Olivine is also one of the most widespread silicate minerals with presence ranging from shallow volcanoes on continents and oceans to deepest accessible samples from the mantle. Thus, physical and chemical properties of olivine have been the subjects of a great number of studies since these properties potentially are critical components in the development of plate tectonics, and consequently influence the geophysical, geochemical, and geodynamic phenomena observed on the Earth's surface.

Olivine is one of the nominally anhydrous minerals (NAMs). A trace amount of water (hydrogen) in olivine has a great effect on its physical and chemical properties, such as viscosity (*Chopra and Paterson*, 1984; *Mackwell et al.*, 1985; *Karato et al.*, 1986; *Hirth and Kohlstedt*, 1996; *Mei and Kohlstedt*, 2000a; *Smyth and Frost*, 2002), ionic diffusivities (*Hier-Majumder et al.*, 2005; *Costa and Chakraborty*, 2008; *Fei et al.*, 2012, 2013), electrical conductivity (*Karato*, 1990; *Wang et al.*, 2006; *Yoshino et al.*, 2006; *Poe et al.*, 2010), and seismic attenuation (*Karato*, 1995; *Karato and Jung*, 1998; *Aizawa et al.*, 2008). Small or large scale heterogeneity in water distribution can potentially have a strong effect on those geochemical and geophysical properties. Thus, fundamental knowledge of the incorporation mechanisms of hydrogen and its kinetic properties in olivine is of great importance not only to the understanding of theories for influences of hydrogen on those physical properties but also to the interpretations of measurements from natural samples combined with observations from laboratories.

Theories of water (hydrogen) distribution and water cycle between various layers of the Earth (e.g., *Bell and Rossman*, 1992, *Bercovici and Karato*, 2003, *Ohtani et al.*, 2004, and *Hirschmann*, 2006) have been proposed based on the water contents obtained from minerals in xenoliths or calculated from rheological properties. Features of water distribution and water cycling processes are very important to the understanding of geodynamic processes in the Earth. However, these models for the water cycle are highly dependent on the knowledge of the dependence of water content on thermodynamic conditions and the reaction between volatile, melt, and minerals. Unfortunately, experimental results of these properties have not yet shown good agreement. Thus, water distribution and transport processes in various layers of the Earth remain ambiguous, and need further

experimental study.

To obtain knowledge of water distribution in the Earth, we need to acquire fundamental understanding of the mechanisms of hydrogen incorporation in minerals. One way to study hydrogen incorporation mechanisms in olivine is by investigating the dependence of water solubility on thermodynamic parameters, such as oxygen fugacity, water fugacity (*Bai*, 1992; *Bai and Kohlstedt*, 1993), chemical activity (*Matveev et al.*, 2001; *Smyth et al.*, 2006), temperature and pressure (e.g., *Kohlstedt et al.*, 1996, *Mosenfelder et al.*, 2006, and *Withers and Hirschmann*, 2008). Water solubility for a mineral is the maximum water content that can be associated in the mineral under water-saturated condition. Water solubility depends on chemical compositions ranging from the major constituent ions, such as iron content (*Zhao et al.*, 2004), to trace element compositions, such as Ti, Cr, Ni (e.g., *Berry et al.*, 2007 and *Walker et al.*, 2007). Measurement of dependence of water solubility on these compositional or thermodynamic parameters can help place constraints on the incorporation mechanisms of hydrogen in olivine.

Natural olivine samples from xenoliths often contain melt inclusions and hydrogen concentration gradients resulting from water gain or loss through the ascent process from deep mantle to the surface at eruption. On the one hand, water content in minerals from xenoliths can help estimate the water content at their original locations; on the other hand, it can also help reveal the kinetic properties of host magma providing the time of xenoliths to ascend to Earth's surface. Previous studies have measured hydrogen diffusion profiles in olivine grains from xenoliths (*Demouchy et al.*, 2006; *Peslier and Luhr*, 2006; *Peslier et al.*, 2008; *Chen et al.*, 2011, 2013; *Denis et al.*, 2013; *Peslier et al.*, 2015). Interpretation of hydrogen profiles in natural sample requires knowledge of hydrogen

diffusion properties. However, results of the diffusivity of hydrogen ions and associated hydrous defects have exhibited a discrepancy of 2 to 3 orders of magnitude (*Mackwell and Kohlstedt*, 1990; *Kohlstedt and Mackwell*, 1998; *Padrón-Navarta et al.*, 2014). Such a difference in hydrogen diffusivity will result in a difference of 2 to 3 orders of magnitude in the time scale associated with the geodynamic processes. Thus, it is critical to have a clear knowledge of hydrogen diffusion properties in olivine to interpret observations from natural samples. Further experimental studies are needed to reconcile the earlier results with such a significant discrepancy.

Silicon diffusivity is another important physical property for understanding the point defect chemistry in olivine. Rates of silicon diffusion play a key role in the rheology of olivine since silicon has the lowest diffusivity among the major component ions of olivine (*Buening and Buseck*, 1973; *Hermeling and Schmalzried*, 1984; *Gérard and Jaoul*, 1989; *Ryerson and Durham*, 1989; *Houlier et al.*, 1990; *Chakraborty*, 1997; *Dohmen et al.*, 2002a; *Dohmen and Chakraborty*, 2007). Thus silicon diffusivity is a critical property for the creep deformation of olivine (e.g., *Kohlstedt*, 2006). More importantly, silicon ions diffuse through vacancies in olivine, and silicon diffusivity is a good indicator of the concentration of silicon vacancies. Thus, results of silicon diffusivity can help understand the overall point defect chemistry in olivine. However, experimental results of silicon diffusivity exhibit significant difference in terms of the magnitude of silicon diffusivity and the activation energy obtained from each data set. So knowledge of silicon diffusion has not concluded, and it needs further experimental studies to interpret the differences among earlier results.

1.2 Outline of the work presented here

Chapter 2 presents my results on water incorporation mechanisms of olivine with the constraints from the dependence of water solubility of olivine on pyroxene activity at 1473 K from 0.3 GPa to 5 GPa. Models for water incorporation in olivine are proposed based on the dependence of water solubility on water fugacity and pyroxene activity to interpret the experimental observations together with the results from earlier experimental studies under similar conditions.

Chapter 3 is a study of hydrogen diffusion properties using both hydration and dehydration experiments for olivine. The diffusion coefficient is obtained from the diffusion profiles of hydroxyl content associated with individual peak present in IR spectra. We compare the results of hydrogen diffusion with the diffusivity of electron holes and metal vacancies in olivine from earlier studies, and discuss how hydrogen diffusion modifies the point defect chemistry of olivine through hydration and dehydration processes .

Chapter 4 presents the results of silicon diffusivity from silicon self-diffusion experiments. Discrepancy between earlier data sets for silicon diffusivity of olivine in terms of values of diffusivity and activation energy are discussed, and we propose reasons for the different values obtained from other studies. In addition, we discuss indications from the results of silicon diffusivity to the point defect chemistry of olivine under dry condition.

Chapter 5 is a summary of the results and proposes future directions following the work present in this thesis.

Chapter 2

Dependence of water solubility in olivine on pyroxene activity at high pressures

[Abstract] Single crystals of Fe-bearing olivine were hydrothermally annealed at 1473 K and 0.3, 3, and 5 GPa with controlled pyroxene activity under water saturated conditions. Pyroxene activity was buffered by the presence of either pyroxene (high a_{px}) or periclase (low a_{px}), and f_{O_2} was buffered by the presence of mixed powders of Ni and NiO or of Fe and FeO. Buffer powders were identified with x-ray diffraction in the run products. The hydroxyl content, $\mathrm{C_{OH}}$, in olivine was measured using infrared spectroscopy. Hydrogen solubility increases with increasing a_{px} at low pressure, 0.3 GPa, but decrease with increasing a_{px} at higher pressures of 3 and 5 GPa. Combined with published results on water solubility with different a_{px} buffers, our results yield a power law dependence of hydrogen concentration on water fugacity, $C_{\mathrm{OH}} \propto f^r_{\mathrm{H_2O}}$, with an exponent of

$r_{\mathrm{px}} = 1.0 \pm 0.1$ and an activation volume $\Delta V_{\mathrm{px}} = (12 \pm 1) \times 10^{-6}$ m^3/mol for samples buffered with pyroxene; and a water fugacity exponent $r_{\mathrm{pc}} = 1.8 \pm 0.5$ and $\Delta V_{\mathrm{pc}} = (25 \pm 8) \times 10^{-6}$ m^3/mol for those buffered with periclase at 3 to 8 GPa. Together with the dependence on a_{px}, these parameters indicate that hydrogen associated with vacant metal sites is the dominant mechanism of water incorporation in olivine buffered with pyroxene, while a different incorporation mechanism, such as hydrogen associated with vacant silicon sites, competes with proton-metal vacancy defect associate in the case of samples buffered with periclase at 3 to 8 GPa. Thus, these factors need to be taken into account to evaluate the hydrogen solubility and incorporation mechanisms in Fe-bearing olivine in order to study the water weakening effect observed for olivine.

2.1 Introduction

Olivine and its high-pressure polymorphs, wadsleyite and ringwoodite, are the most abundant minerals in Earth's upper mantle and transition zone. Their physical properties are thus important to understanding of large-scale geodynamic processes. Trace amounts of water (hydrogen) in these nominally anhydrous minerals (NAMs) greatly alter their physical properties. For olivine, previous experimental studies investigated the influences of water on viscosity (*Chopra and Paterson*, 1984; *Mackwell et al.*, 1985; *Karato et al.*, 1986; *Mei and Kohlstedt*, 2000a; *Karato and Jung*, 2003), ionic diffusivities (*Hier-Majumder et al.*, 2005; *Costa and Chakraborty*, 2008; *Fei et al.*, 2012), and electrical conductivity (*Karato*, 1990; *Wang et al.*, 2006; *Yoshino et al.*, 2006; *Poe et al.*, 2010).

Thus, it is critical to have a clear understanding of the mechanisms of the incorporation of water in NAMs. The mechanism(s) by which water affects concentrations of point defects on the constituent-ion (Me, Si and O) sites and thus influences physical properties remains controversial. In particular, there has been an extended discussion concerning the relative roles of silicon vacancies and metal vacancies as the dominant defects with which hydrogen is associated in Fe-bearing olivine. Clues of the mechanisms can be drawn from the dependencies of water solubility on thermodynamic parameters including water fugacity, pyroxene activity, pressure and temperature. In the literature, the effect of pyroxene activity has been investigated by hydrothermally annealing either natural or synthetic crystals of olivine and forsterite over a limited range of pressure (*Matveev et al.*, 2001; *Lemaire et al.*, 2004; *Smyth et al.*, 2006). To help place constraints on the mechanism of incorporation of hydrogen in olivine, we have investigated water solubility by hydrothermally annealing olivine single crystals buffered at two different pyroxene activities at pressures from 0.3 to 5 GPa.

2.2 Water solubility experiments

Hydrothermal annealing experiments were performed at a confining pressure, P, of 0.3 GPa in a gas-medium apparatus and at 3 to 8 GPa in a multi-anvil solid-medium apparatus. For all experiments, gem quality single crystals of San Carlos olivine that were free of apparent flaws were oriented using Laue back-reflection x-ray diffraction.

The chemical composition of the crystals, measured with an electron microprobe, is listed in

Table 2.1: Chemical composition of San Carlos olivine single crystals in wt.%.

Crystal #	Al_2O_3	TiO_2	SiO_2	NiO	FeO	MgO	CaO	MnO	Cr_2O_3	Mg#
1	0.01	0.00	39.98	0.30	10.44	48.99	0.13	0.14	0.01	91.3
2	0.02	0.02	40.39	0.34	10.88	48.15	0.05	0.13	0.01	88.9
3	0.02	0.02	40.80	0.36	8.79	49.79	0.07	0.10	0.04	91.0
4	0.01	0.01	40.36	0.33	10.58	48.51	0.06	0.12	0.01	89.6

Table 2.1.

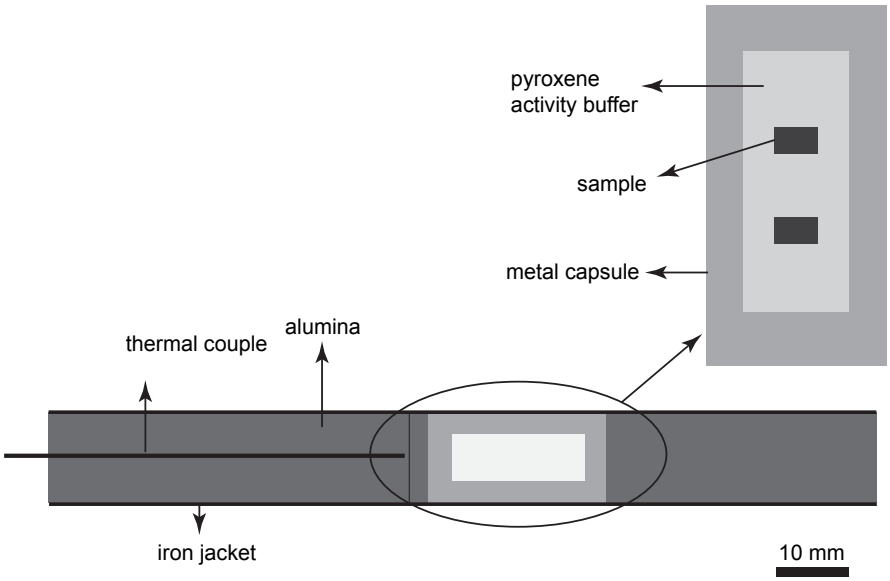

Figure 2.1: Experimental assembly for gas-medium apparatus.

For experiments at P = 0.3 GPa, crystals were cut along the [100], [010] and [001] crystallographic directions with dimensions $x_a \approx 2$ mm, $x_b \approx 1.5$ mm, and $x_c \approx 1$ mm. The [001] direction dimension was set with the smallest length to minimize the duration of hydrothermal experiment since hydrogen diffuses fastest along that direction (*Kohlstedt and Mackwell*, 1998). Crystals were cold-pressed with mixtures of talc plus brucite powders and 0.08 g of distilled water

into a metal capsule with a wall thickness of 2 mm, an inner diameter of 7.5 mm, and a length of 15 mm, as illustrated in Figure 2.1. The ratio of talc to brucite was set to either 2:1 or 1:1 by weight, producing forsterite plus pyroxene, px, or forsterite plus periclase, pc, which fixes pyroxene activity at $a_{\text{px}} = 1$ or $a_{\text{pc}} = 1$. To calculate a_{px} in the case of samples buffered with periclase ($a_{\text{pc}} = 1$), we used the Gibbs free energy of formation of iron-bearing olivine (Fo_{93}) from Mg-Fe oxide and enstatite, -25.7 kJ/mol (*Hobbs*, 1983), and obtained $a_{\text{px}} \approx 0.14$ at 1600 K and room pressure. Oxygen fugacity was controlled at Ni/NiO or Fe/FeO by using either nickel or iron as the capsule material. Each metal capsule was sealed by laser welding; the quality of the weld seam was checked by monitoring any weight lost associated with keeping the capsules in a vacuum oven at 393 K for half an hour. To finish the assembly, the sealed capsule was positioned between alumina spacers and zirconia pistons, and this assembly was inserted into an iron jacket. For each hydrothermal annealing experiments, temperature and pressure were increased synchronously to 0.3 GPa and 1473 K. The length of annealing process was fixed at 5 h based on reported values of hydrogen diffusivity (*Kohlstedt and Mackwell*, 1998), in order to saturate the single crystals. Samples were cooled by turning off the power to the furnace, which decreased the temperature to 773 K in about one minute. Capsules were pierced with a drill to test for the presence of free water as proof of a sufficient water supply to provide a water-saturated environment. Buffer powders and single crystals were retrieved for further analyses.

For hydrothermal annealing experiments at higher pressures of 3, 5 and 8 GPa, a multi-anvil solid-medium apparatus was used. For these experiments, cylinders were cored from San Carlos olivine single crystals along [010] with a diameter of 1.5 mm from which discs were cut with

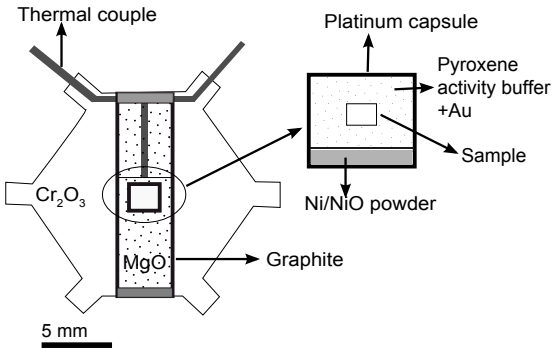

Figure 2.2: Experimental assembly and capsule design for multi-anvil apparatus.

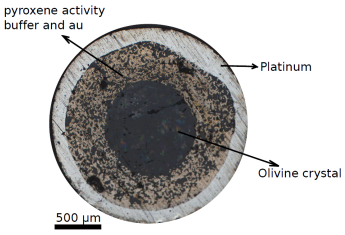

Figure 2.3: Reflected light optical microscope image of sample M713 and capsule after polishing.

thicknesses of 0.5 to 1 mm. Each single crystal disc was packed into a platinum capsule with the pyroxene activity buffer, 0.002 g of distilled water, nickel foil, and an oxygen fugacity buffer of Ni/NiO powder mixture, as shown in Figure 2.2. The pyroxene activity buffer was chosen from among mixtures of fine ground, natural orthopyroxene and gold powders, mixtures of brucite and gold powders, or periclase powder; the presence of gold mechanically softens the medium. Each platinum capsule was sealed by arc welding with the capsule mounted in a water-cooled vice. Capsule weight was recorded both before and after the welding process to guarantee that free water did not evaporate during the process. After the pressure reached a stable target level for at least 1 h, the sample was heated to 1473 K. After 5 h, temperature was decreased at a rate of 60 K/min to 773 K before cooling to room temperature by turning off the power to furnace. Pressure typically was ramped down overnight to minimize formation of cracks in the crystals. Capsules were drilled open to check for free water as evidence of a water-saturated environment, and the presence of

green NiO powder plus the nickel foil provided evidence that the oxygen fugacity was buffered at Ni/NiO.

Intact rectangular blocks of the single crystal, retrieved from the experiments at 0.3 GPa, were polished on both (010) surfaces with diamond lapping film down to 0.5 μm size. The orientation uncertainty is within 2° after polishing. Samples from experiments at higher pressures, retrieved without removing the platinum capsule to minimize cracking, were polished using the procedure described above for samples from the experiments at 0.3 GPa. An optical micrograph of one sample is shown in Figure 2.3. All samples were kept in acetone overnight to dissolve any remaining crystal bond that was applied during the polishing processes and then dried in a vacuum oven at $\sim$373 K for $>$1 h to eliminate any moisture on either surface or in cracks before infrared analysis.

2.3 Analytical methods

2.3.1 Fourier transform infrared spectroscopy

A Fourier transform infrared (FTIR) spectrometer equipped with a Nic-Plan IR microscope and a KBr beam splitter was used to analyze the hydrogen content in olivine single crystals. An unpolarized beam in transmittance mode was used with an aperture from 50×50 to 150×150 μm^2. The detector was set to 128 scans per spectrum with a resolution of 2 cm^{-1}. The spectrometer was equipped with an enclosed sample chamber with flowing dry air. Profile measurements were collected along the sample diameter to check the homogeneity of the hydrogen distribution, another indicator of a water-saturated environment. A smooth spline was fit to each IR spectrum in regions

away from OH-stretching bands as baseline and subtracted from original spectrum. Absorption coefficient was obtained by normalizing absorption to a thickness of 1 cm. To compare with the published results, hydroxyl content was calculated using the calibration of *Paterson* (1982) for each sample

$$C_{OH} = \frac{B_i}{150\zeta} \int \frac{H(\nu)}{(3780 - \nu)} d\nu, \tag{2.1}$$

where C_{OH} is hydroxyl concentration in $H/10^6$Si, B_i is the unit cell volume (4.39×10^4 $H/10^6$Si was used based on published data), ζ is the orientation factor (a value of $1/2$ was used for unpolarized radiation (*Mackwell and Kohlstedt*, 1990)), ν is the wavenumber and $H(\nu)$ is the absorption coefficient. The reported water solubility of a sample is the average of a series of measurements made along a sample diameter, multiplied by a factor of 3.5 (*Bell et al.*, 2003) for comparison with other water content measurement techniques.

Hydroxyl content was also calculated by integrating the area in cm^{-2} for the region from 3650 to 3000 cm^{-1} in the IR spectra. Individual peaks with specific wavenumbers were fitted with a Gaussian distribution function. We quantified the hydroxyl content associated with each peak as the integrated area of a Gaussian curve in cm^{-2} in order to determine the intensity of each peak and compare their relative contributions to the overall hydrogen content in the samples.

2.3.2 X-ray diffraction

Buffer powders from the experiments at 0.3 GPa were identified with x-ray diffraction. Characteristic peaks for pyroxene or periclase were confirmed so as to guarantee their presence as the pyroxene activity buffer, which is the product from the reaction between talc and brucite.

2.3.3 Water fugacity calculation

In a chemical system with an oxygen fugacity buffer and a pyroxene activity buffer, water fugacity, f_{H_2O}, is a function of oxygen fugacity, f_{O_2}, as well as of pressure and temperature. From the reaction of water formation (Equation 2.2), *Mackwell and Kohlstedt* (1990) obtained the solutions for hydrogen fugacity, f_{H_2}, and water fugacity shown in Equation 2.4 and 2.5 since $f_{O_2} \ll f_{H_2}$ and f_{H_2O}

$$\frac{f_{H_2O}}{f_{O_2}^{1/2} f_{H_2}} = K_{H_2O}, \tag{2.2}$$

$$P = P_{H_2O} + P_{H_2} + P_{O_2} \approx P_{H_2O} + P_{H_2} = \frac{f_{H_2O}}{\gamma_{H_2O}} + \frac{f_{H_2}}{\gamma_{H_2}}, \tag{2.3}$$

$$f_{H_2} \approx \frac{P\gamma_{H_2O}\gamma_{H_2}}{\gamma_{H_2O} + \gamma_{H_2} K_{H_2O} f_{O_2}^{1/2}}, \tag{2.4}$$

$$f_{H_2O} \approx \frac{P\gamma_{H_2O}\gamma_{H_2} K_{H_2O} f_{O_2}^{1/2}}{\gamma_{H_2O} + \gamma_{H_2} K_{H_2O} f_{O_2}^{1/2}}, \tag{2.5}$$

where K_{H_2O} is the equilibrium constant of the formation reaction of water; γ_{H_2}, γ_{H_2O}, and γ_{O_2} are hydrogen, water and oxygen fugacity coefficients; P is pressure. As expressed in Equation 2.5, water fugacity is a function of f_{O_2}, γ_{H_2}, γ_{H_2O}, γ_{O_2}, and K_{H_2O}, which are also functions of temperature and pressure. Unfortunately, there are no reported explicit thermal parameters at the conditions of this study. If we extrapolate the values of γ_{H_2}, γ_{H_2O}, and K_{H_2O} from *Shaw and Wones* (1964), *Tödheide* (1972), and *Robie et al.* (1978), respectively, we can calculate water fugacity for the cases of samples buffered with Ni/NiO and Fe/FeO. Values of water fugacity at 1473 K and 0.3 GPa for these two cases are 302 MPa and 190 MPa, respectively, different by a factor of $\sim$1.5.

Alternatively, with equation of state for water (*Pitzer and Sterner*, 1994), a water fugacity of

325 MPa is obtained at the same temperature and pressure condition regardless of oxygen fugacity (e.g., Ni/NiO vs Fe/FeO). In this study, we calculated water fugacity using the equation of state for water (*Pitzer and Sterner*, 1994). However, we should keep in mind that in a system with controlled oxygen fugacity and pyroxene activity, water fugacity differs from that of a pure water system.

2.4 Water solubility results

Hydroxyl contents were determined for ten samples hydrothermally annealed at 0.3 GPa with f_{O_2} buffered by Ni/NiO or Fe/FeO and a_{px} buffered by either magnesium oxide or pyroxene. The results are summarized in Table 2.2. In addition, hydroxyl contents were determined for thirteen samples hydrothermally annealed at 3 to 8 GPa with f_{O_2} buffered by Ni/NiO and a_{px} buffered by either magnesium oxide or orthopyroxene. The results are summarized in Table 2.3.

At 0.3 GPa, the absorption peaks in the IR spectrum from samples buffered by pyroxene have higher amplitudes than those from samples buffered by periclase for both f_{O_2} buffers, as shown in Figures 2.4 and 2.5. In the case with f_{O_2} fixed at Ni/NiO, the hydroxyl content in samples buffered with pyroxene is 750 to 800 $H/10^6Si$, while the hydroxyl content of samples buffered with periclase is 350 to 400 $H/10^6Si$. With f_{O_2} fixed at Fe/FeO, the hydroxyl content is smaller than if f_{O_2} is fixed at Ni/NiO, both for samples buffered with pyroxene, $\sim$ 300$H/10^6Si$, and for those buffered with periclase, $\sim$180$H/10^6Si$.

Table 2.2: Water solubility of the samples hydrothermally annealed at 0.3 GPa and 1473 K for 5 h. Pyroxene activity was buffered with either pyroxene, px, or periclase, pc. $*$: Hydroxyl content calculated with the *Paterson* (1982) calibration and magnified by a factor of 3.5 (*Bell et al.*, 2003). $**$: Hydroxyl content calculated as the integrated area under each spectrum. Values in the columns labeled with wavenumber are the integrated area of each peak in cm^{-2} as a proxy of hydroxyl content.

Run #	f_{O_2}	a_{px}	C_{OH}^{*} ($H/10^6Si$)	C_{OH}^{**} (cm^{-2})	C_{OH}^{3572} (cm^{-2})	C_{OH}^{3566} (cm^{-2})	C_{OH}^{3543} (cm^{-2})	C_{OH}^{3525} (cm^{-2})	C_{OH}^{3485} (cm^{-2})	C_{OH}^{3355} (cm^{-2})	C_{OH}^{3329} (cm^{-2})	C_{OH}^{3225} (cm^{-2})
PI-1676[a]	Ni/NiO	px	7.5×10^2	7.3×10^1	7.5	14.3	1.4	20.0	4.5	8.8	11.2	7.4
PI-1676	Ni/NiO	px	7.7×10^2	8.2×10^1	7.7	14.7	1.4	20.5	4.6	9.1	11.5	7.6
PI-1712	Ni/NiO	px	8.0×10^2	9.4×10^1	8.0	15.2	1.5	21.3	4.8	9.4	11.9	7.9
PI-1674[a]	Ni/NiO	pc	3.8×10^2	4.0×10^1	5.3	6.4	1.1	9.0	2.8	0.5	0.5	7.2
PI-1674	Ni/NiO	pc	4.0×10^2	4.3×10^1	5.5	6.8	1.1	9.4	3.0	0.6	0.5	7.6
PI-1715	Ni/NiO	pc	3.5×10^2	3.8×10^1	4.8	5.9	1.0	8.3	2.6	0.5	0.5	6.3
PI-1680	Fe/FeO	px	3.1×10^2	2.8×10^1	5.9	4.3	0.3	7.0	2.2			
PI-1708	Fe/FeO	px	2.8×10^2	2.5×10^1	5.3	3.9	0.3	6.3	2.0			
PI-1691	Fe/FeO	pc	2.1×10^2	1.6×10^1	3.2	2.1	0.1	2.5	0.3			
PI-1706	Fe/FeO	pc	1.6×10^2	1.4×10^1	2.4	1.6	0.1	1.9	0.2			

a: sample wrapped with nickel foil and natural orthopyroxene and not in direct contact with talc and brucite buffer powders.

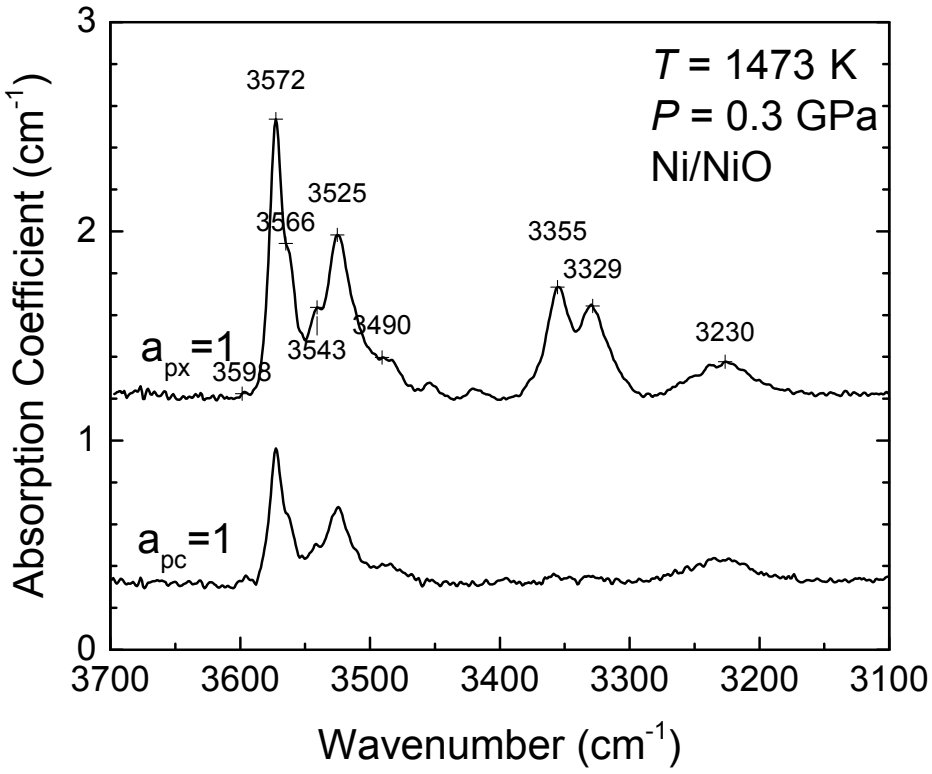

Figure 2.4: Unpolarized FTIR spectra from samples hydrothermally annealed at 0.3 GPa, 1473 K and buffered by either pyroxene (PI-1712) or periclase (PI-1715). Oxygen fugacity was buffered with Ni/NiO.

For both pyroxene and periclase buffered samples, the largest peaks are located at the wavenumbers of 3566 and 3525 cm^{-1} (see Table 2.2). For pyroxene buffered samples at the higher f_{O_2}, significant peaks also occur at 3355 and 3329 cm^{-1}, as shown in Figure 2.4; for periclase buffered samples, these peaks are absent. In the case with f_{O_2} fixed at Fe/FeO, peaks at 3355 and 3329 cm^{-1} are absent in both spectra, as shown in Figure 2.5. The hydrogen concentration in samples buffered with pyroxene is larger than those buffered with periclase.

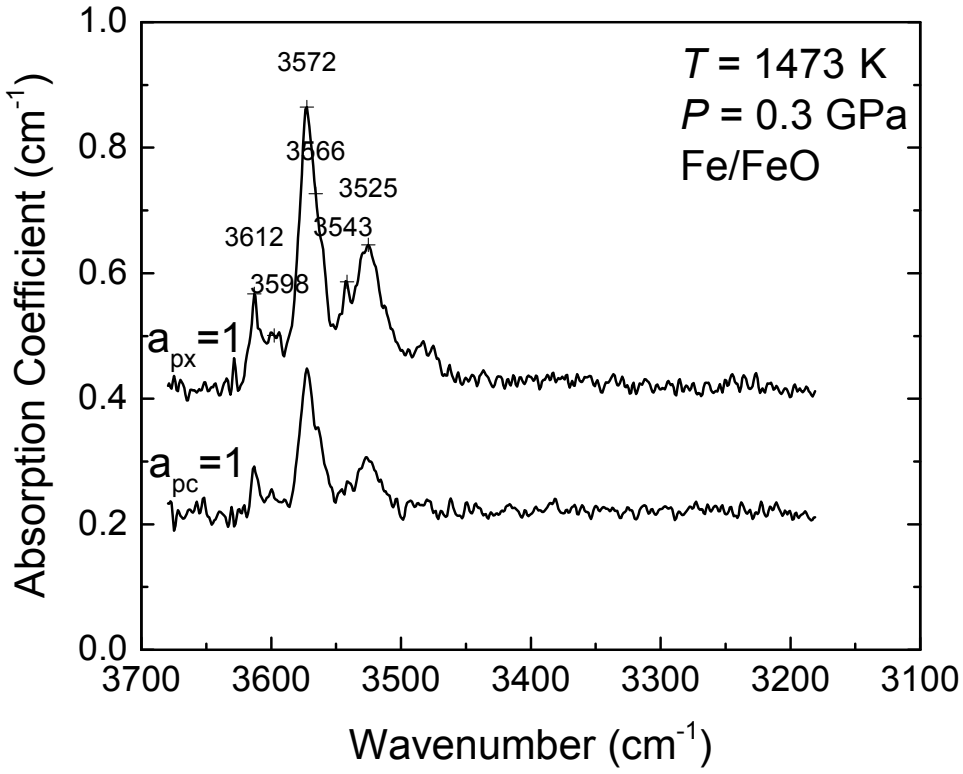

Figure 2.5: Unpolarized FTIR spectra from samples hydrothermally annealed at 0.3 GPa, 1473 K and buffered by either pyroxene (PI-1708) or periclase (PI-1706). Oxygen fugacity was buffered with Fe/FeO.

At higher pressures, 3 and 5 GPa, the dependence of hydrogen concentration on pyroxene activity differs from the case at 0.3 GPa. Samples buffered with periclase exhibit higher hydroxyl contents than samples buffered with pyroxene, as illustrated in Figure 2.6 and 2.7.

Table 2.3: Water solubility of the samples hydrothermally annealed at 3, 5 and 8 GPa, 1473 K for 5 hours. Pyroxene activity was buffered with either pyroxene, px, or periclase, pc. Oxygen fugacity was buffered with Ni/NiO. $*$: Hydroxyl content calculated with *Paterson* (1982) calibration and magnified by a factor of 3.5 (*Bell et al.*, 2003). $**$: Hydroxyl content calculated as the integrated area under each spectrum. Values in the columns labeled with wavenumber are the integrated area of each peak in cm^{-2} as a proxy of hydroxyl content.

Run #	P (GPa)	a_{px}	H_2O present	C_{OH}^{*} ($H/10^6Si$)	C_{OH}^{**} (cm^{-2})	C_{OH}^{3612} (cm^{-2})	C_{OH}^{3598} (cm^{-2})	C_{OH}^{3572} (cm^{-2})	C_{OH}^{3566} (cm^{-2})	C_{OH}^{3550} (cm^{-2})	C_{OH}^{3535} (cm^{-2})	C_{OH}^{3525} (cm^{-2})	C_{OH}^{3511} (cm^{-2})	C_{OH}^{3485} (cm^{-2})	C_{OH}^{3355} (cm^{-2})	C_{OH}^{3329} (cm^{-2})
M647	3	px	×	$> 1.4 \times 10^3$	2.0×10^2	4	4	8	16			1	23	45	20	34
M666	3	px	√	1.6×10^3	2.1×10^2	9	7	16	22			19	16	22	15	38
M708	3	px	√	1.9×10^3	2.6×10^2	6	8	12	24			38	23	25	23	56
M713	3	px	√	2.2×10^3	3.1×10^2	7	9	14	27			44	27	28	27	64
M648	3	pc	×	$> 1.6 \times 10^4$	1.5×10^3											
M709	3	pc	√	2.6×10^4	2.6×10^3	463	183	979	113	323	251					
M671	3	pc	√	1.6×10^4	1.7×10^3	256	92	565	197	149	178					
M712	3	pc	√	3.1×10^4	3.1×10^3	473	143	1219	115	502	357					
M670	5	px	√	4.0×10^3	4.5×10^2	63	40	60	24						43	54
M682	5	px	√	4.4×10^3	5.1×10^2	69	43	66	27						48	59
M625	5	pc	√	1.1×10^4	1.2×10^3	226			229							
M650	5	pc	√	1.1×10^4	1.2×10^3	145	156		374		120					
M704	8	px	×	$> 1.7 \times 10^3$	4.5×10^2											

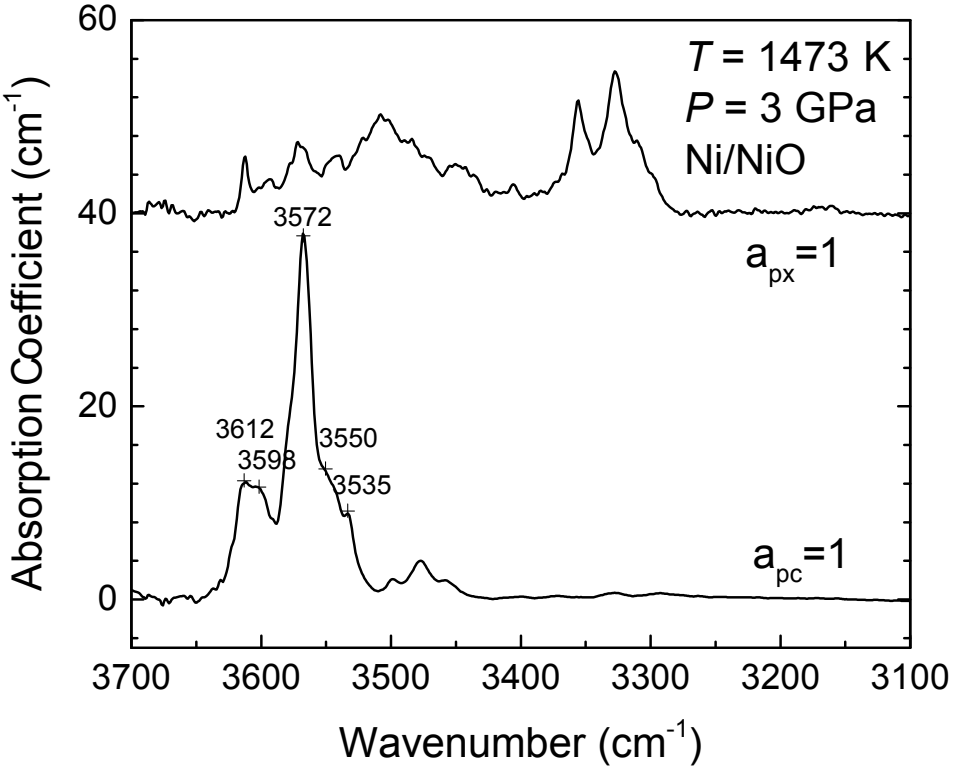

Figure 2.6: Unpolarized FTIR spectra from samples hydrothermally annealed at 3 GPa, 1473 K and buffered with either pyroxene (M713) or periclase (M671). Oxygen fugacity was buffered with Ni/NiO.

At 3 GPa, for samples buffered with pyroxene, the heights of the peaks at 3566 and 3525 cm^{-1} are similar to those of the peaks at 3355 and 3329 cm^{-1}. The latter group of peaks is absent in IR spectra from samples buffered with periclase, and the peaks of highest hydroxyl content are located at the wavenumbers of 3612, 3572 and 3550 cm^{-1}, as shown in Figure 2.6.

At 5 GPa, for samples buffered with pyroxene as well as samples buffered with periclase, the largest peaks are located at 3612, 3598, 3572, 3566, and 3550 cm^{-1}. For pyroxene buffered

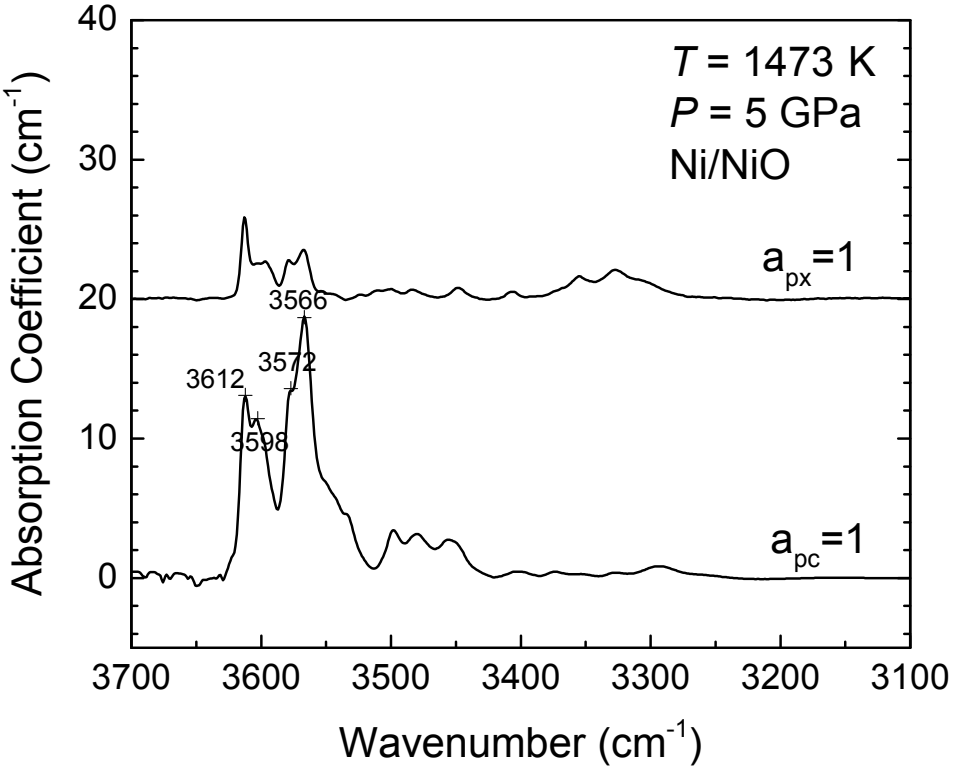

Figure 2.7: Unpolarized FTIR spectra from samples hydrothermally annealed at 5 GPa, 1473 K and buffered with either pyroxene (M670) or periclase (M650). Oxygen fugacity was fixed by Ni/NiO.

samples, similar to the observation of 0.3 GPa, smaller peaks at 3355 and 3329 cm^{-1} are again clearly present; for periclase buffered samples, these peaks are absent, as shown in Figure 2.7.

As illustrated in Figure 2.8, at pressures of 3 and 5 GPa, for samples buffered with pyroxene, water solubility increases with increasing pressure. However, as shown in Figure 2.9, for samples buffered with periclase, water solubility is higher at 3 GPa than that at 5 GPa.

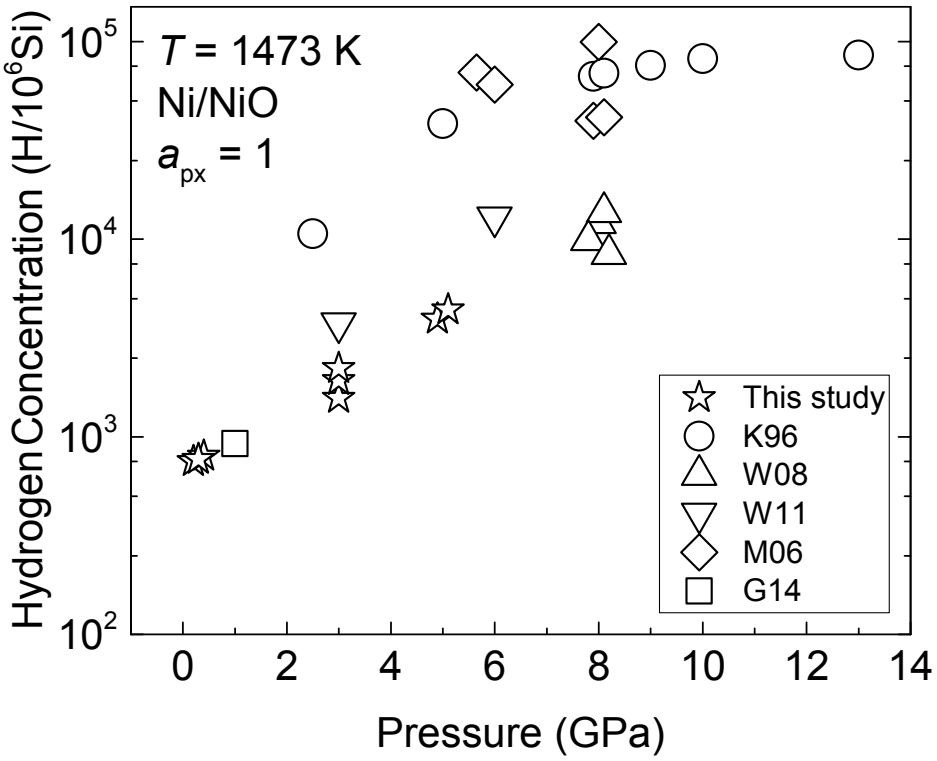

Figure 2.8: Water solubility of olivine buffered with pyroxene versus pressure. All referenced data were normalized to 1473 K and $X_{\mathrm{Fa}} = 0.1$ using equation 7(b) of *Zhao et al.* (2004). Stars are data from this study for the samples buffered with pyroxene and the circle, diamond, up-pointing triangle, down-pointing triangle, and square are data from *Kohlstedt et al.* (1996), *Mosenfelder et al.* (2006), *Withers and Hirschmann* (2008), *Withers et al.* (2011), and *Gaetani et al.* (2014), respectively.

2.5 Discussion

Water solubility (hydroxyl content) of olivine depends on various thermodynamic parameters. Here we expand this relationship by including the pyroxene activity in the expression from (*Zhao et al.*,

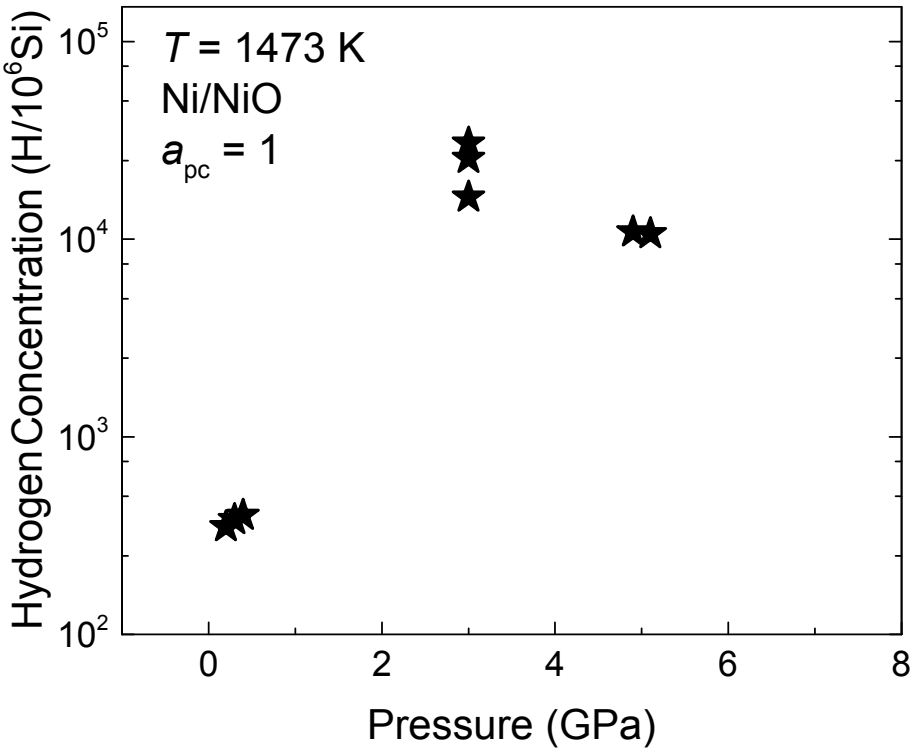

Figure 2.9: Water solubility of olivine buffered with periclase versus pressure.

2004) to obtain the following equation:

$$C_{OH} = A f_{H_2O}^{r} f_{O_2}^{m} a_{px}^{q} \exp(\frac{\alpha X_{Fa}}{RT}) \exp(-\frac{\Delta E^{\circ} + P\Delta V^{\circ}}{RT}), \tag{2.6}$$

where a_{px} is the pyroxene activity and X_{Fa} is the iron content;ΔE° and ΔV° are the changes of internal energy and molar volume due to the incorporation of H in olivine; r, m, and q are the exponents of water and oxygen fugacity and pyroxene activity. The dependencies on these parameters (values of the exponents) provide constrains on the mechanism(s) by which hydrogen

is incorporated in olivine.

Hydrogen ions associated with the defects on metal sites can be described by reactions such as

$$H_2O(\text{fl}) + 2O_O^{\times} + Me_{Me}^{\times} + MeSiO_3 \Longleftrightarrow \{2(OH)_O^{\bullet} - V_{Me}^{//}\}^{\times} + Me_2SiO_4 \quad (\text{srg}), \tag{2.7}$$

or

$$H_2O(\text{fl}) + 2O_O^{\times} + Me_{Me}^{\times} + MeSiO_3 \Longleftrightarrow \{(OH)_O^{\bullet} - V_{Me}^{//}\}^{/} + (OH)_O^{\bullet} + Me_2SiO_4 \quad (\text{srg}), \tag{2.8}$$

where fl means in the fluid phase, and srg means site of repeatable growth. By applying the law of mass action to the point defect reaction in Equation 2.7, we obtain

$$[\{2(OH)_O^{\bullet} - V_{Me}^{//}\}^{\times}] \propto f_{O_2}^0 f_{H_2O}^1 a_{px}^1. \tag{2.9}$$

and for Equation 2.8, with charge neutrality governed by $[(OH)_O^{\bullet}] = [\{(OH)_O^{\bullet} - V_{Me}^{//}\}^{/}]$, we obtain

$$[(OH)_O^{\bullet}] = [\{(OH)_O^{\bullet} - V_{Me}^{//}\}^{/}] \propto f_{O_2}^0 f_{H_2O}^{\frac{1}{2}} a_{px}^{\frac{1}{2}}. \tag{2.10}$$

An example of hydrogen ions associated with Si vacancies can be described by the reaction

$$2H_2O(\text{fl}) + Si_{Si}^{\times} + 4O_O^{\times} + Me_2SiO_4 \Longleftrightarrow \{4(OH)_O^{\bullet} - V_{Si}^{////}\}^{\times} + 2MeSiO_3 \quad (\text{srg}). \tag{2.11}$$

Again, by applying the law of mass action, the concentration of defect associates is

$$[\{4(OH)_O^{\bullet} - V_{Si}^{////}\}^{\times}] \propto f_{O_2}^0 f_{H_2O}^2 a_{px}^{-2}. \tag{2.12}$$

A more complete summary of the dependencies of hydrogen concentration on each parameter for a certain mechanism is presented in Table 2.4. As shown in Equation 2.9, 2.10 and 2.12,

the concentration of hydrogen ions associated with metal vacancies (e.g., $\{2(\mathrm{OH})_{\mathrm{O}}^{\bullet} - \mathrm{V}_{\mathrm{Me}}^{//}\}^{\times}$) increases linearly with increasing water fugacity and concentration of hydrogen ions associated with silicon vacancy (e.g., $\{4(\mathrm{OH})_{\mathrm{O}}^{\bullet} - \mathrm{V}_{\mathrm{Si}}^{////}\}^{\times}$) increases with increasing water fugacity to the power of two. We can also notice that these two defect associates have different dependencies on pyroxene activity; the concentration of hydrogen ions associated with metal vacancies increases with increasing pyroxene activity, while the concentration of hydrogen ions associated with silicon vacancies decreases with increasing pyroxene activity.

Table 2.4: Possible charge neutrality conditions; intrinsic and water-derived point defects dependencies on thermodynamic parameters of concentrations in olivine under dry and wet conditions. The numbers in each cell are m, r, q and p, respectively, where [defect] $\propto f_{O_2}^m f_{H_2O}^r a_{px}^q x^p$ for $(Mg_{1\text{-}x}Fe_x)_2SiO_4$. For all charge neutrality conditions, $[\{2(OH)_O^\bullet - V_{Me}^{//}\}^\times] \propto f_{H_2O}^1 a_{px}^1$ and $[\{4(OH)_O^\bullet - V_{Si}^{////}\}^\times] \propto f_{H_2O}^2 a_{px}^{\text{-}2}$.

Charge Neutrality	$[Fe_{Me}^\bullet]$	$[V_{Me}^{//}]$	$[(OH)_O^\bullet]$	$[\{(OH)_O^\bullet - V_{Me}^{//}\}^/]$	$[\{3(OH)_O^\bullet - V_{Si}^{////}\}^/]$	$[Fe_{Si}^/]$
$[Fe_{Me}^\bullet] = 2[V_{Me}^{//}]$	$\frac{1}{6}$ 0 $\frac{1}{3}$ $\frac{2}{3}$	$\frac{1}{6}$ 0 $\frac{1}{3}$ $\frac{2}{3}$	-$\frac{1}{12}$ $\frac{1}{2}$ $\frac{1}{3}$ -$\frac{1}{3}$	$\frac{1}{12}$ $\frac{1}{2}$ $\frac{2}{3}$ $\frac{1}{3}$	$\frac{1}{12}$ $\frac{3}{2}$ -$\frac{7}{3}$ $\frac{1}{3}$	$\frac{1}{3}$ 0 -$\frac{10}{3}$ $\frac{4}{3}$
$[(OH)_O^\bullet] = 2[V_{Me}^{//}]$	$\frac{1}{4}$ -$\frac{1}{6}$ $\frac{1}{3}$1	0 $\frac{1}{3}$ $\frac{1}{3}$ 0	0 $\frac{1}{3}$ $\frac{1}{3}$ 0	0 $\frac{2}{3}$ $\frac{2}{3}$ 0	0 $\frac{5}{3}$ -$\frac{7}{3}$ 0	$\frac{1}{4}$ $\frac{1}{6}$ -$\frac{10}{3}$ 1
$[Fe_{Me}^\bullet] = [\{(OH)_O^\bullet\text{-}V_{Me}^{//}\}^/]$	$\frac{1}{8}$ $\frac{1}{4}$ $\frac{1}{2}$ $\frac{1}{2}$	$\frac{1}{4}$ -$\frac{1}{2}$ 0 1	-$\frac{1}{8}$ $\frac{3}{4}$ $\frac{1}{2}$ -$\frac{1}{2}$	$\frac{1}{8}$ $\frac{1}{4}$ $\frac{1}{2}$ $\frac{1}{2}$	$\frac{1}{8}$ $\frac{5}{4}$ -$\frac{5}{2}$ $\frac{1}{2}$	-$\frac{3}{8}$ -$\frac{1}{4}$ -$\frac{7}{2}$ $\frac{3}{2}$
$[(OH)_O^\bullet] = [\{(OH)_O^\bullet\text{-}V_{Me}^{//}\}^/]$	$\frac{1}{4}$ 0 $\frac{1}{2}$ 1	0 0 0 0	0 $\frac{1}{2}$ $\frac{1}{2}$ 0	0 $\frac{1}{2}$ $\frac{1}{2}$ 0	0 $\frac{3}{2}$ -$\frac{5}{2}$ 0	$\frac{1}{4}$ 0 -$\frac{7}{2}$ 1
$[(OH)_O^\bullet] = [Fe_{Si}^/]$	$\frac{3}{8}$ -$\frac{1}{4}$ -$\frac{3}{2}$ $\frac{2}{3}$	-$\frac{1}{4}$ $\frac{1}{2}$ 4 -1	$\frac{1}{8}$ $\frac{1}{4}$ -$\frac{3}{2}$ $\frac{1}{2}$	-$\frac{1}{8}$ $\frac{3}{4}$ $\frac{2}{5}$ -$\frac{1}{2}$	-$\frac{1}{8}$ $\frac{7}{4}$ -$\frac{1}{2}$ -$\frac{1}{2}$	$\frac{1}{8}$ $\frac{1}{4}$ -$\frac{3}{2}$ $\frac{1}{2}$
$[(OH)_O^\bullet] = [\{3(OH)_O^\bullet\text{-}V_{Si}^{////}\}^/]$	$\frac{1}{4}$ $\frac{1}{2}$ -1 1	0 -1 3 0	0 1 -1 0	0 0 2 0	0 1 -1 0	$\frac{1}{4}$ -$\frac{1}{2}$ 2 1

Base on the results of this study, at 0.3 GPa, water solubility increases with pyroxene activity, yielding a positive pyroxene activity exponent. This observation indicates that hydrogen ions associated with metal vacancies are the dominant mechanism at that temperature and pressure condition. In the literature, *Bai* (1992) reported a water fugacity exponent of about 1, consistent with hydrogen ions associated with metal vacancies as the major incorporation mechanism at 0.05 to 0.3 GPa and 1573 K. Recall from Figures 2.4 and 2.5 in the results section of this paper, at 0.3 GPa, the dominant peaks appear at 3566 and 3525 cm^{-1}, so these peaks are likely related to hydrogen ions associated with metal vacancies.

In addition, in the case with oxygen fugacity buffered at Ni/NiO, IR spectra from samples buffered with pyroxene also exhibit peaks at 3355 and 3329 cm^{-1}, but these peaks are almost invisible in the IR spectra from samples buffered with periclase (Figure 2.4). IR peaks in the 3400-3300 cm^{-1} regions are correlated with the content of trivalent cations in olivine (*Berry et al.*, 2007). Thus, our results indicate that the presence of periclase has an effect on the incorporation of hydrogen ions with trivalent ions in olivine single crystals.

For samples with oxygen fugacity buffered at Fe/FeO (Figure 2.5), the positions of dominant peaks are the same as those present in the IR spectra of samples with oxygen fugacity buffered at Ni/NiO. However, a minor peak is present at 3612 cm^{-1}, which is absent in the other case. In addition, no peak is any obvious in the 3400-3300 cm^{-1} region.

Oxygen fugacity values are 2.3×10^{-6} Pa and 1.8×10^{-2} Pa for samples buffered with Fe/FeO and Ni/NiO, respectively. Based on Equation 2.5, the water fugacity, as well as oxygen fugacity, is different for these two cases even though temperature and pressure are the same. Thus, the

incorporation of hydrogen ions with trivalent cations (IR peaks at 3355 and 3329 cm^{-1}) is dependent on either oxygen fugacity, water fugacity, or both under the experimental conditions.

At 3 and 5 GPa, the locations of the primary peaks for samples buffered with periclase are at 3612 and 3572 cm^{-1} as opposed to 3566 and 3525 cm^{-1} as observed in the case of 0.3 GPa. These peaks are higher than those of samples buffered with pyroxene. Data from *Withers and Hirschmann* (2008) and *Aubaud et al.* (2007) similarly show a higher water solubility at 8 GPa for sample buffered with ferropericlase than those buffered with pyroxene, indicating a negative dependence of water solubility of olivine on pyroxene activity. These observations suggest that a different mechanism of water incorporation in olivine will start to compete at pressure $\geq$ 3 GPa.

As shown in Figure 2.8, for comparison purpose with previous studies, hydroxyl concentration for olivine samples buffered with pyroxene from the studies of *Kohlstedt et al.* (1996), *Withers and Hirschmann* (2008), *Withers et al.* (2011), and *Gaetani et al.* (2014) are plotted normalized to 1473 K and $X_{\mathrm{Fa}} = 0.1$ using the formula 7(b) from *Zhao et al.* (2004), with water fugacity calculated with the equation of state for water from *Pitzer and Sterner* (1994) (Table 2.5). Water solubility of olivine buffered with pyroxene at 1 GPa (*Gaetani et al.*, 2014), 3 GPa and 6 GPa (*Withers and Hirschmann*, 2008; *Withers et al.*, 2011) agrees well with that of this study. Meanwhile water solubility at 2.5 to 13 GPa from *Kohlstedt et al.* (1996) and *Mosenfelder et al.* (2006) is systematically larger than the results of this study by a factor of 2 to 3. Possibly the pyroxene activity buffer powders used in those experiments produced periclase due to a ratio of 1.4:1 between talc and brucite.

Similar to Equation 2.6, water solubility can be expressed

$$C_{OH} = A(a_{px}, f_{O_2}^m, X_{Fa}) f_{H_2O}^r \exp(-\frac{\Delta E^\circ + P\Delta V^\circ}{RT}). \quad (2.13)$$

To study the water fugacity exponent *r*, the solubility of water in olivine samples buffered with pyroxene at 1473 K from this study and those from *Mosenfelder et al.* (2006), *Withers et al.* (2011), and *Gaetani et al.* (2014) were chosen based on sample's chemical composition and similar experimental conditions to calculate $C_{OH} \times \exp(\frac{\Delta E^\circ + P\Delta V^\circ}{RT})$. A value of $\Delta V = 10.0 \times 10^{-6}\,m^3/mol$ was previously determined from the study of *Zhao et al.* (2004) for samples buffered with pyroxene, and is used in this study to plot $C_{OH} \times \exp(\frac{\Delta E^\circ + P\Delta V^\circ}{RT})$ versus water fugacity in Figure 2.10. A least-squares linear fit yields a slope of $r_{px} = 1.0 \pm 0.1$ for samples buffered with pyroxene. This value agrees well with the water fugacity exponent from earlier studies with similar pyroxene activity buffer (*Bai*, 1992; *Kohlstedt et al.*, 1996).

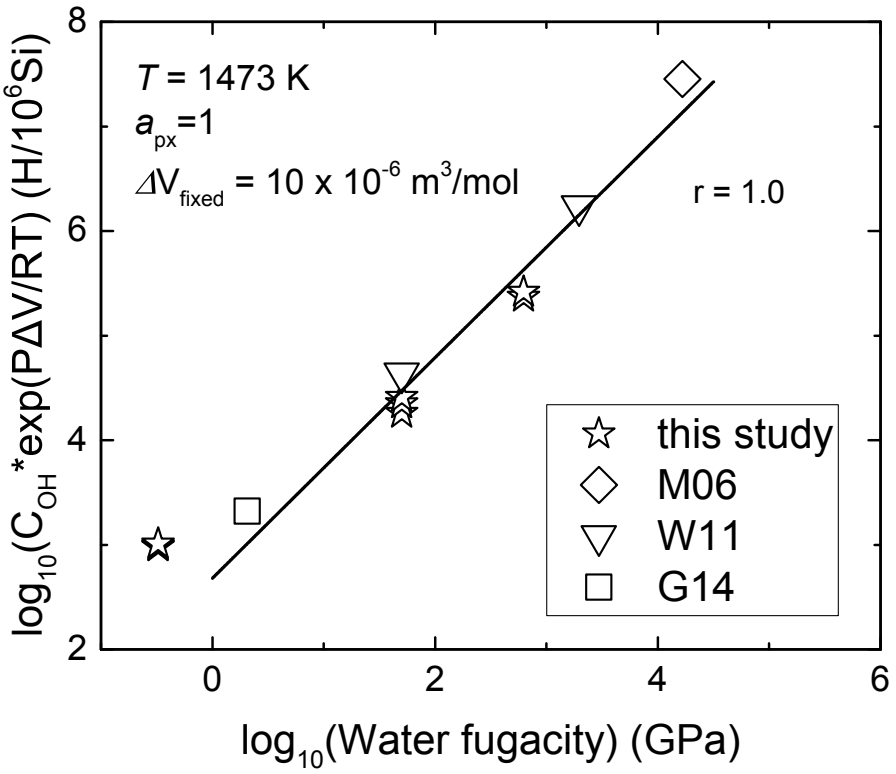

Figure 2.10: Log-log plot of pressure and temperature weighted water solubility in olivine buffered with pyroxene versus water fugacity. Stars are data obtained in the present study including runs from both gas-medium and solid-medium experiments. Diamonds, triangles, and square are data from solid-medium experiments of *Mosenfelder et al.* (2006), *Withers et al.* (2011), and *Gaetani et al.* (2014), respectively. The solid line is a linear least-squares fit of the data to Equation 2.13, as described in the Discussion section.

If water fugacity exponent is fixed at $r_{\mathrm{px}} = 1$, the activation volume can be evaluated by plotting $\log_{10}(\mathrm{C_{OH}} \times f_{\mathrm{H_2O}}^{-r})$ against pressure (see Equation 2.13), which yields an activation volume of $\Delta V_{\mathrm{px}} = (12 \pm 1) \times 10^{-6}\,\mathrm{m^3/mol}$, as shown in Figure 2.11. This value of activation volume is approximately equal to the MgO molar volume (*Karato*, 2006), consistent with an incorporation

mechanism of hydrogen associated with metal vacancies. Thus, the positive dependence on pyroxene activity at low pressure, the value of the water fugacity exponent, and the activation volume all suggest that hydrogen incorporates in olivine buffered with pyroxene through association with vacant metal sites at pressure from 0.3 to 8 GPa.

Meanwhile, for the case of samples buffered with periclase, we fit water fugacity exponent r_{pc} and the activation volume ΔV_{pc} simultaneously with the results from this study and that of *Withers and Hirschmann* (2008) and obtained $r_{\mathrm{pc}} = 1.8 \pm 0.5$ and $\Delta V_{\mathrm{pc}} = (25 \pm 8) \times 10^{-6}\,\mathrm{m}^3/\mathrm{mol}$. With the different values for water fugacity exponent and the activation volume combined with the negative dependence on pyroxene activity at high pressure, we suggest that a different water incorporation mechanism competes with that of hydrogen associated with metal vacancies in the case of samples buffered with periclase at high pressure (3 to 8 GPa), such as hydrogen associated with silicon vacancies. Thus, hydrogen ions associated with the peaks at 3612 and 3572 cm^{-1} are incorporated through a different mechanism than those associated with the peaks at 3566 and 3535 cm^{-1}. However, further results are needed to constrain fully the incorporation mechanism that dominates in the case of samples buffered with periclase at high pressure.

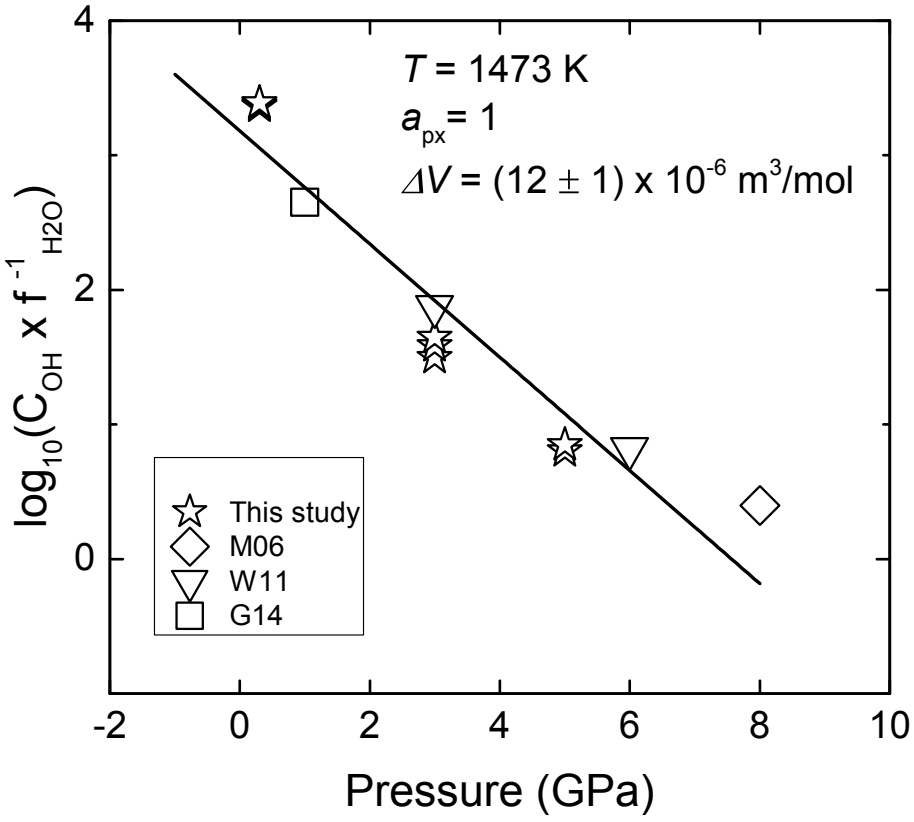

Figure 2.11: Semi-log plot of $C_{\mathrm{OH}} \times f_{\mathrm{H_2O}}^{-1}$ versus pressure of data from this study, *Mosenfelder et al.* (2006), *Withers et al.* (2011), and *Gaetani et al.* (2014) for samples buffered with pyroxene at 1473 K. The solid line is a linear least-squares fit of all the data to Equation 2.13, which yields an activation volume of $(12 \pm 1) \times 10^{-6}\,(\mathrm{m}^3/\mathrm{mol})$.

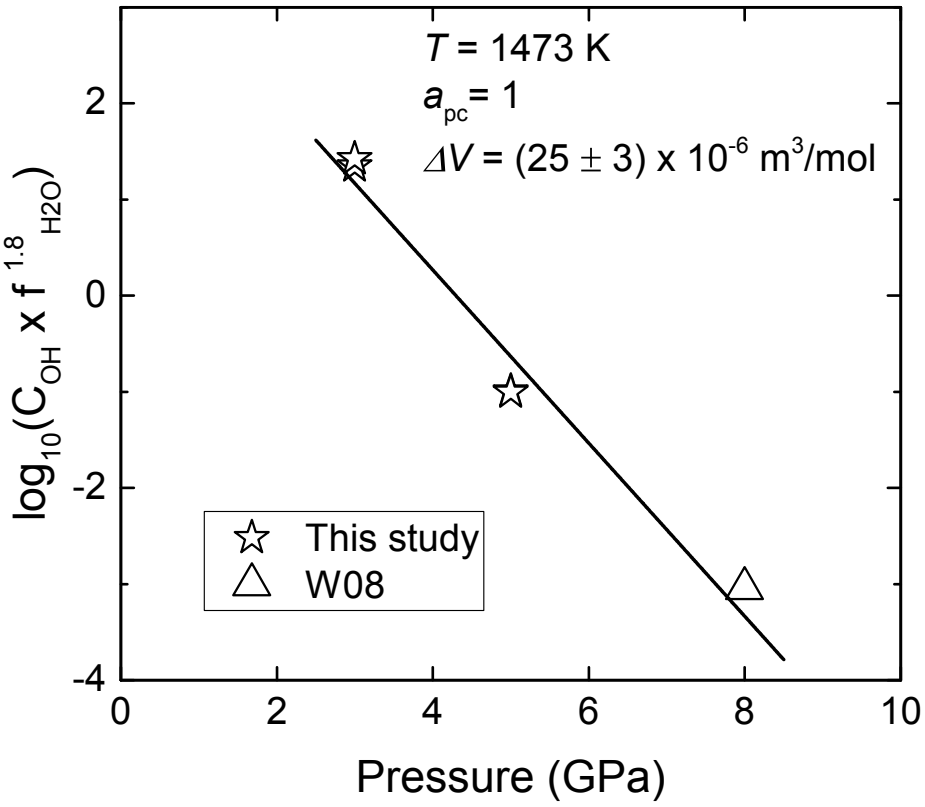

Figure 2.12: Semi-log plot of $C_{\mathrm{OH}} \times f_{\mathrm{H_2O}}^{-1.8}$ versus pressure of data from this study and *Withers and Hirschmann* (2008) for samples buffered with periclase at 1473 K. The solid line is a linear least-squares fit of all the data to Equation 2.13, which yields an activation volume of $(25 \pm 8) \times 10^{-6}$ $(\mathrm{m}^3/\mathrm{mol})$.

Table 2.5: Results of water solubility from earlier studies. C^*_{OH} is hydroxyl content normalized to 1473 K and Fo_{90} using the formula from *Zhao et al.* (2004). Pyroxene activity buffers: en, px, and pc are enstatite, pyroxene, and periclase, respectively.

T (K)	P (GPa)	a_{px} buffer	C_{OH} ($H/10^6Si$)	C^*_{OH} ($H/10^6Si$)	Reference
1373	2.5	en	7.70×10^3	1.07×10^4	*Kohlstedt et al.* (1996)
1373	5	en	2.82×10^4	3.84×10^4	*Kohlstedt et al.* (1996)
1373	8	en	4.94×10^4	6.67×10^4	*Kohlstedt et al.* (1996)
1373	8	en	5.11×10^4	6.91×10^4	*Kohlstedt et al.* (1996)
1373	9	en	5.60×10^4	7.57×10^4	*Kohlstedt et al.* (1996)
1373	10	en	6.09×10^4	8.21×10^4	*Kohlstedt et al.* (1996)
1373	12	en	8.61×10^4	1.18×10^5	*Kohlstedt et al.* (1996)
1373	13	en	6.23×10^4	8.53×10^4	*Kohlstedt et al.* (1996)
1273	5.65	en	2.99×10^4	6.96×10^4	*Mosenfelder et al.* (2006)
1273	6	en	2.60×10^4	6.05×10^4	*Mosenfelder et al.* (2006)
1273	8	en	4.30×10^4	9.95×10^4	*Mosenfelder et al.* (2006)
1373	8	en	2.48×10^4	3.98×10^4	*Mosenfelder et al.* (2006)
1473	8	en	3.53×10^4	4.14×10^4	*Mosenfelder et al.* (2006)
1793	8	en	1.93×10^4	1.20×10^4	*Withers and Hirschmann* (2008)
1673	8	px	1.94×10^4	1.37×10^4	*Withers and Hirschmann* (2008)
1773	8	px	1.61×10^4	9.88×10^3	*Withers and Hirschmann* (2008)
1823	8	px	1.45×10^4	8.43×10^3	*Withers and Hirschmann* (2008)
1673	8	pc	3.56×10^4	2.56×10^4	*Withers and Hirschmann* (2008)
1473	6	px	1.29×10^4	1.29×10^4	*Withers et al.* (2011)
1473	3	px	3.75×10^3	3.75×10^3	*Withers et al.* (2011)
1473	1	px	1.03×10^3	9.2×10^2	*Gaetani et al.* (2014)

2.6 Geological implications

★Based on the results in this study, pyroxene activity plays an important role in water solubility and incorporation mechanisms in olivine. Water solubility increases with increasing pyroxene activity at 0.3 GPa and decreases with increasing pyroxene activity at pressures greater than 1 GPa. Water solubility differs by up to an order of magnitude between pyroxene and periclase buffers, so different chemical and compositional conditions are capable of creating a strong water distribution anomaly throughout the upper mantle in the Earth. One should evaluate pyroxene activity carefully when analyzing the water content present to derive thermodynamic conditions at the formation of water incorporation in olivine samples.

★If pyroxene is present as a chemical activity buffer, two protons associated with a metal vacancy is the dominant incorporation mechanism under the thermodynamic conditions of the upper mantle. Although, the incorporation of hydrogen ions with a silicon vacancy will increase the concentration of silicon vacancy and greatly change the rheological creep behavior of rock-forming minerals in the upper mantle, the concentration of the hydrogen associated with silicon vacancies has not been found to be dominant from the observations in this study.

Chapter 3

Diffusion rates of hydrous defects associated with site-specific IR spectra wavenumbers for natural olivine

[Abstract] Hydration and dehydration experiments were carried out using naturally occurring, iron-bearing single crystals of San Carlos olivine under 200 to 300 MPa at 1173 to 1303 K for hydration anneals and under 1 atm at 1191 to 1358 K for dehydration anneals. Chemical diffusion coefficients were determined from diffusion profiles for individual OH-stretching bands from a series of IR spectra. Within experimental uncertainty, the diffusivities associated with the individual bands are in good agreement with one another in both the hydration and the dehydration experiments. The center wavenumbers of these bands include 3598, 3572, 3566, 3543, 3525, 3490, 3372,

3355, 3329 cm^{-1}. Hydration proceeds by two diffusion mechanisms, as reported previously. The faster process involves diffusion of hydrogen coupled with a counter flux of electron holes with hydrogen diffusion rate-limiting hydration. For this mechanism, diffusion is faster along the [100] direction than along [010] and [001]. The slower process involves hydrogen diffusion coupled with a parallel flux of metal vacancies with vacancy diffusion rate-limiting hydration. For this mechanism, diffusion is faster along [001] than along [100] and [010], consistent with the anisotropy reported for the diffusion of metal cations. The dehydration process exhibits similar slower diffusion kinetics. The anisotropy in diffusion rate is consistent with hydrogen diffusion out of the olivine single crystals with a parallel flux of metal vacancies. The good agreement between the diffusivities determined from dehydration experiments and those obtained from hydration experiments demonstrates the validity of analyzing hydrogen diffusion profiles in naturally occurring olivine grains to obtain rates of ascent of xenoliths.

3.1 Introduction

The incorporation of a small amount of water (hydrogen) in nominally anhydrous minerals (NAMs) profoundly influences the kinetic properties of the materials that compose Earth's upper mantle including viscosity (*Mackwell et al.*, 1985; *Karato et al.*, 1986; *Hirth and Kohlstedt*, 1996; *Mei and Kohlstedt*, 2000a,b; *Dixon et al.*, 2004; *Karato*, 2006; *Kohlstedt*, 2006; *Karato*, 2010), electrical conductivity (*Karato*, 1990, 2006; *Simpson and Tommasi*, 2005; *Poe et al.*, 2010; *Du Frane and Tyburczy*, 2012; *Wang et al.*, 2006; *Yoshino et al.*, 2009; *Wang et al.*, 2012), ionic diffusion (*Wang*

et al., 2004; *Hier-Majumder et al.*, 2005; *Costa and Chakraborty*, 2008; *Chakraborty*, 2010; *Fei et al.*, 2013), and attenuation of seismic waves (*Karato and Spetzler*, 1990; *Karato and Jung*, 1998; *Karato*, 2003; *Aizawa et al.*, 2008; *Jacobsen et al.*, 2008). As the smallest and lightest element, the hydrogen ion (proton) has the highest mobility through crystal lattice, and this property enables it to create water-derived defects in rock-forming minerals at a very fast rate (*Mackwell and Kohlstedt*, 1990; *Kohlstedt and Mackwell*, 1998). Since olivine is the most abundant mineral in Earth's upper mantle, the mechanism of incorporation of water in olivine and the associated alteration of its point defect chemistry has been the subject of a number of studies and vigorous debate over the last three decades.

Although hydrogen ions are bonded to oxygen ions in olivine and observed as OH stretching bands in infrared spectra, the specific mechanisms by which hydrogen is incorporated into the lattice remains under discussions. Studies have focused on the dependence of water solubility on various thermodynamic parameters (*Bai*, 1992; *Kohlstedt et al.*, 1996; *Mosenfelder et al.*, 2006; *Withers and Hirschmann*, 2008; *Kovács et al.*, 2010; *Gaetani et al.*, 2014). These analyses provide some insights into the mechanisms of water incorporation mechanisms under water-saturated, thermodynamic equilibrium conditions. However, diffusion processes of hydrogen in olivine have not been fully understood. On one hand, knowledge of the mechanisms by which hydrogen diffuses in olivine can help in understanding the hydration process that leads to a water-saturated condition and thus interpretation of the observed dependence of the water solubility on specific thermodynamic parameters. On the other hand, under most thermochemical conditions in Earth's mantle, rocks are not under water-saturation conditions (*Peslier*, 2010) and constantly undergo dynamic hydrogen

compositional exchange with the ambient environment, such as in the transition zone and at the lithosphere-asthenosphere boundary (LAB) (*Hirschmann*, 2006; *Green et al.*, 2010; *Karato*, 2011). Thus, it is of great importance to investigate the kinetics of hydrogen transport processes and the mechanisms by which hydrogen diffuses into or out of olivine grains.

Recent studies have discussed site-specific hydrogen incorporation mechanisms (*Berry et al.*, 2005; *Walker et al.*, 2007; *Kovács et al.*, 2010). These authors have argued that there are four different substitution mechanisms in forsterite, including hydrogen ions associated with Si vacancies $(4H)^{\times}_{Si}$, hydrogen ions associated with metal vacancies $(2H)^{\times}_{Me}$, hydrogen ions involved with titanium substitution $(Ti^{4+})^{\bullet\bullet}_{Me}(2H)^{//}_{Si}$, and hydrogen ions associated with trivalent cations $(Me^{3+})^{\bullet}_{Me}(H^{/}_{Me})$.

In a recent study on synthetic samples of forsterite and Ti-doped forsterite, *Padrón-Navarta et al.* (2014) reported a unique diffusivity for each of the site-specific species based on analyses of IR spectra measured following dehydration experiments with a series of time. From their results, the hydrous defects that they associate with trivalent cations and metal vacancies exhibited the highest diffusivity, while those that they associate with silicon vacancies had the lowest diffusivity.

In the present study, experiments were carried out using natural iron-bearing single crystals of olivine to investigate the hydration and dehydration kinetics for site-specific hydrous defects. Our goal is to improve our knowledge of diffusion processes of the hydrous defects based on experimental observations and address the issue of hydrogen diffusion results reported for forsterite and the titanium-doped forsterite. The results test the applicability of diffusivities obtained on Fe-free samples to naturally occurring rocks. In addition, the observations reported here examine the

appropriateness of calculating rates of ascent of mantle xenoliths determined from dehydration profiles using hydrogen diffusivities obtained from hydration experiments.

3.2 Hydrogen diffusion experiment methods

Naturally occurring single crystals of iron-bearing San Carlos (Arizona, USA) olivine with no cracks or optically visible inclusions were prepared for hydrogen diffusion experiments. The crystals were orientated using Laue X-ray diffraction, and the orientations were checked with EBSD pole figures.

3.2.1 hydration experiments

For hydration experiments, five samples (SC14-6, SC16-4, SC31-2, SC31-3, and SC31-5) were cut with faces perpendicular to each of the crystallographic axes ($\pm 5^{\circ}$) and polished using diamond lapping films from 30 to 0.5 μm. Samples sizes were roughly $3 \times 5 \times 3$ mm parallel to [100], [010], and [001], respectively. FTIR analyses were performed to confirm the dry state of the samples prior to hydration experiments. Two samples, SC14-6 and SC16-4 were hydrothermally annealed for relatively short times of $\leq$1 h in iron and nickel capsules at temperatures of 1173 and 1273 K, respectively, and a confining pressure of 300 MPa using a gas-medium pressure vessel. Oxygen fugacity was buffered by either Fe/FeO or Ni/NiO powders. Silica activity was buffered by a mixture of olivine plus orthopyroxene powders. The other three samples, SC31-2, SC31-3, and SC31-5, were hydrothermally annealed for relatively long times of $\geq$5 h in platinum capsules at

temperatures of 1173 to 1303 K and a confining pressure of 200 MPa in a cold-seal pressure vessel. Oxygen fugacity was buffered by Ni/NiO powders. Silica activity was buffered by orthopyroxene powders. Experimental conditions are summarized in Table 3.1.

Table 3.1: Experimental conditions and results of hydration experiments. $logD_a$, $logD_b$, and0 $logD_c$ represent the chemical diffusion coefficients obtained from the diffusion profiles of full IR spectra along [100], [010], and [001]. Diffusivities of hydrogen ions from the faster mechanism were obtained from samples SC14-6 and SC16-4, and diffusivities of metal vacancies from the slower mechanism were obtained from samples SC31-2, SC31-3, and SC31-5.

Sample #	T (K)	P (MPa)	t (h)	P_{O_2} buffer	$a \times b \times c$ (mm^3)	$logD_a$ (m^2/s)	$logD_b$ (m^2/s)	$logD_c$ (m^2/s)
SC14-6	1173	300	1	Fe/FeO	$3.32 \times 4.07 \times 3.19$	-10.0	-11.5	-10.9
SC16-4	1273	300	0.58	Ni/NiO	$2.84 \times 5.03 \times 3.23$	-9.8	-11.7	-11.1
SC31-2	1173	200	21.1	Ni/NiO	$2.82 \times 4.72 \times 3.38$	-14.2	-13.6	-12.5
SC31-3	1273	200	8	Ni/NiO	$2.82 \times 4.76 \times 3.02$	-12.8	-12.4	-11.3
SC31-5	1303	200	5	Ni/NiO	$2.70 \times - - \times 2.82$	-12.0	—	-10.8

At the end of each experiment, temperature was decreased at a constant pressure to 973 K at $\sim$150 K/min, and then decreased to room temperature at $\sim$30 K/min. A fast initial cooling was used to prevent the formation of a secondary hydrous phase and limit the precipitation of the hydrous defects as fluid inclusions (*Mackwell et al.*, 1985; *Kohlstedt and Mackwell*, 1998). Metal capsules were pierced to verify the presence of water.

3.2.2 Dehydration experiments

For the dehydration experiments, the first step was to obtain water-saturated olivine single crystals with a uniform distribution of hydrogen throughout the samples. Olivine single crystals were pressed with talc and brucite (2:1 by weight) and 10 to 14 drops of distilled water into cylindrical nickel capsules with an inner diameter of 1.2 mm and a length of 2.0 mm. A nickel disc was then laser welded onto each end of the capsule to prevent direct loss of water. Hydrothermal anneals were carried out at 1473 K and 300 MPa for 5 h using a gas-medium apparatus (*Paterson*, 1990). Water-saturation was confirmed with FTIR spectra that revealed a uniform hydrogen content along all three crystallographic axes. The second step of a dehydration experiment involved annealing slices of water-saturated olivine samples in a one-atmosphere furnace with a thermocouple monitoring the temperature at the sample. Temperature was set within the range 1191 to 1358 K. The experimental conditions for each of four runs are summarized in Table 3.2. Oxygen fugacity was set at $\sim 10^{-7}$ atm with a flowing mixture of CO and CO_2 and monitored with an oxygen fugacity sensor. Samples were quickly retracted from the furnace at the end of experiments and cooled to room temperature. Samples were cut perpendicular to [010] to extract the center slab with [010] as the normal vector, as shown schematically in Figure 3.1. Chemical diffusion profiles along [100] and [001] were generated by collecting IR spectra along two crossed straight lines from and to the outer edges of the sample slab. The other two center slabs from the side slices of previous cutting step were cut perpendicular to [001] direction (Figure 3.1) to obtain hydrogen diffusion profiles along [010] by collecting IR spectra on the these two side slices.

Table 3.2: Experimental conditions and results of dehydration experiments. $logD_a$, $logD_b$, and0 $logD_c$ represent the chemical diffusion coefficients obtained from the diffusion profiles of full IR spectra along [100], [010], and [001].

Sample #	T	t	$a \times b \times c$	$logD_a$	$logD_b$	$logD_c$
#	(K)	(h)	(mm^3)	(m^2/s)	(m^2/s)	(m^2/s)
PI-1914	1253	5	$3.07 \times 4.42 \times 3.65$	-12.3	-12.3	-11.2
PI-1918-1	1322	3	$2.99 \times 0.67 \times 2.28$	-12.0	—	-11.1
PI-1918-2	1358	2	$2.71 \times 0.94 \times 2.67$	-11.8	—	-11.0
PI-1918-3	1191	20	$1.83 \times 2.50 \times 1.83$	-13.4	—	-11.5

3.3 Analytical methods for chemical diffusion profiles

3.3.1 Fourier transform infrared spectroscopy

Hydration chemical diffusion profiles

The hydroxyl distribution within samples was analyzed using Fourier transform infrared (FTIR) spectroscopy. Infrared spectra were collected on samples from edge to edge along center axis, as shown in Figure 3.2, over the wavenumber range 2000 to 4000 cm^{-1} with a Bruker™ IFS 120 HR high resolution FTIR spectrometer coupled with a Bruker™ IR microscope and a KBr beam splitter. Two hundred scans were accumulated for each spectrum at a resolution of 1 cm^{-1}. A polarized IR beam (E//a) was focused at the center depth along the sample thickness. Other aspects of the technical setup are identical to those described by *Demouchy and Mackwell* (2003). IR

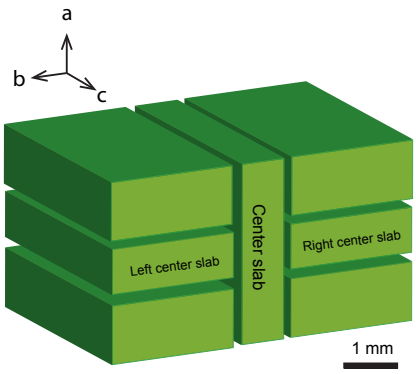

Figure 3.1: Sketch of sections extracted from samples of both hydration and dehydration experiments used to measure diffusion profiles along crystallographic axes. Center slice is used for the [100] and [001] profiles, left and right centered slices are used for the [010] profile.

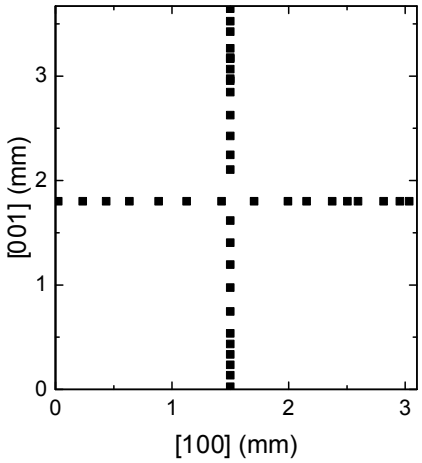

Figure 3.2: Map of locations at which IR spectra were collected on the center slice (3.07 × 3.65 mm) of the sample PI-1914. A denser spacing was chosen near the edges. Measurements on other samples have a similar pattern for locations.

spectra of hydration samples at various locations are shown in the Appendix B.1 in Figures B.1.1 to B.1.5.

Dehydration chemical diffusion profiles

For the dehydration diffusion samples, a Fourier transform infrared spectrometer equipped with a Nic-Plan IR microscope and a KBr beam splitter at the University of Minnesota was used to analyze hydrogen diffusion profiles. An unpolarized beam in transmittance mode was used and IR spectra were recorded in the wavenumber range of 1000 to 4000 cm^{-1}. One-hundred twenty-eight scans were accumulated with a resolution of 2 cm^{-1}. A window size of 20×200 μm with the long dimension perpendicular to the profile direction was chosen to minimize the convolution

effect due to the gradient in water concentration along the diffusion profile, thus optimizing the signal-to-noise ratio. Air purged of H_2O and CO_2 was flowed into the FTIR sample chamber to limit contamination due to atmospheric moisture. A background spectrum was collected before measurements on samples to remove the interference from the residual moisture in the air. IR spectra of dehydration samples at various locations are shown in the Appendix B.1 in Figures B.1.6 to B.1.8.

3.3.2 IR individual peak fitting method

Raw IR spectra were processed with OriginLab® software. Each spectrum was firstly smoothed using 20 points Savitzky-Golay filtering method to increase the signal-to-noise ratio. Each IR spectrum was baseline corrected by fitting the regions away from OH- stretching bands and normalized to a thickness of 1 cm. The spectrum was then deconvolved as the summation of a series of peaks, each with a Gaussian distribution of the form

$$A^i = A_0^i + \frac{C^i}{\sigma^i\sqrt{2\pi}} e^{-\frac{(\nu-\nu_c^i)^2}{2\sigma^{i2}}}, \tag{3.1}$$

where ν is wavenumber in cm^{-1}, ν_c^i is the center wavenumber from ith peak, A^i and A_0^i are the IR absorption coefficient and residual background level in cm^{-1}, and C^i and σ^i are the integral area and standard deviation of the ith Gaussian distribution. The total number and the wavenumber of the selected primary peaks, ν_c^i, were identified with the "pick-peak" function in OriginLab® software; the picked-peak wavenumber was compared with values reported in previous studies. The wavenumbers of six to nine primary peaks were chosen as the input of fitting parameters so

as to obtain optimal fitting results. Figure 3.3 is an example of fitting the overall spectrum from sample SC31-3C with 9 individual peaks, each with a Gaussian distribution, with the wavenumber labeled above each peak. The other chemical diffusion profiles are shown in the Appendix B.3 in Figures B.3.1 to B.3.5 and in the Appendix B.4 in Figures B.4.1 to B.4.4.

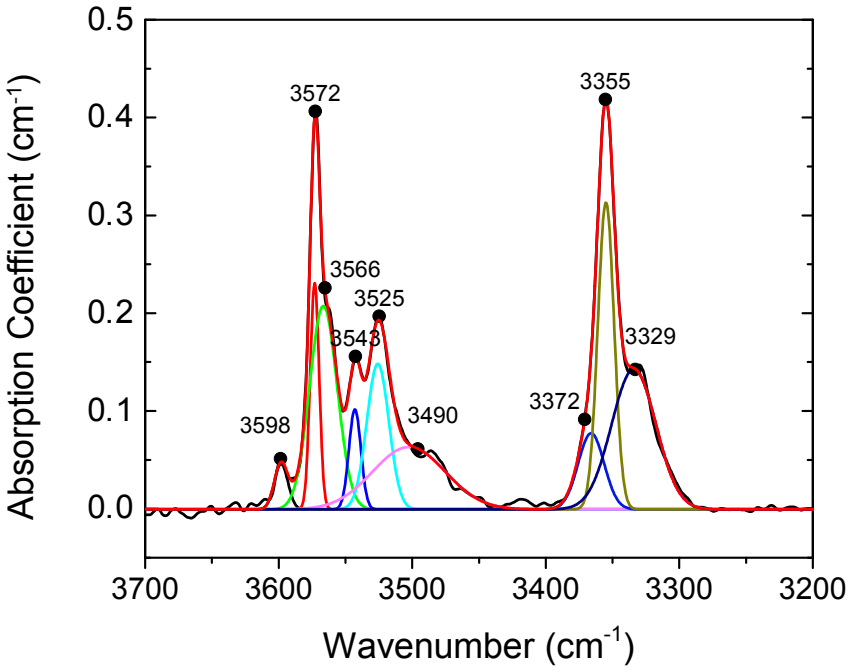

Figure 3.3: An IR spectrum from sample SC31_3C decomposed into 9 Gaussian peaks. Red curve is the fit to the full spectrum, which is shown as the black curve.

3.3.3 Determining the diffusivities for water-derived point defects

The hydroxyl concentration, [OH], associated with each site-specific hydrous defect (in ppm by site) is proportional to the integrated area C^i (in cm^{-2}) under that peak in the IR spectrum. Thus we treat integrated area under a peak in an IR spectrum as the corresponding hydroxyl concentration.

Hydroxyl concentration evolves with time and position according to Fick's second law

$$\frac{\partial C}{\partial t} = \widetilde{D}\nabla^2 C, \tag{3.2}$$

where C is hydroxyl concentration, [OH], $\widetilde{D}$ is chemical diffusion coefficient, and t is time. For a one-dimensional diffusion profile in a hydration experiment, data were fitted with the solution to Equation 3.2 for an infinite source into a finite slab for a short period of time (*Carslaw and Jaeger*, 1959);

$$C = C_0 + (C_1 - C_0) \times \{\text{erfc}(\frac{x}{2\sqrt{\widetilde{D} \cdot \text{t}}}) + \text{erfc}(\frac{\text{w} - x}{2\sqrt{\widetilde{D} \cdot \text{t}}})\}, \tag{3.3}$$

where w is width of the sample, C_0 is the initial [OH] before the diffusion process, and C_1 is [OH] at the surface of the sample. Values for C_0 and C_1 were obtained from fitting the diffusion profiles with Equation 3.3. For the samples from hydration experiments, C_0 was near zero. For the samples from dehydration experiments, C_1 was constrained at 0 corresponding to the fully depleted condition at the surface of the sample.

Interpretation of a measured value for a chemical diffusivity requires understanding the charge coupling condition associated with the diffusion process. Previous studies identified two distinct chemical diffusivities associated with hydrogen diffusion based on the kinetics and anisotropy of the diffusion of water-derived point defects (*Mackwell and Kohlstedt*, 1990; *Kohlstedt and Mackwell*, 1998). At relatively low temperatures and short experimental durations, a fast diffusion process occurs that these authors associated with the exchange of protons with polarons (electron holes created by ferric iron ions occupying octahedrally coordinated metal cation sites); this process was referred to as redox exchange. At higher temperature and longer experimental durations, a slower

diffusion process dominates that was attributed to hydrogen diffusion coupled with a parallel flux of metal vacancies; this process was termed hydrous defect incorporation.

Under anhydrous conditions iron-bearing olivine has a maximum polaron content $\sim$100 ppm in one-atmosphere, controlled-p_{O_2}-experiments (*Nakamura and Schmalzried*, 1983; *Tsai and Dieckmann*, 1997, 2002); this value sets a limit on the amount of hydrogen that can be incorporated through the redox exchange mechanism. This process is rate limited by the diffusion of hydrogen ions, which is strongly anisotropic with the fastest diffusion direction parallel to [100] (e.g., *Yoshino et al.*, 2006; *Poe et al.*, 2010). Thus the chemical diffusivity, $\widetilde{D}$, obtained from the OH concentration profiles associated with the redox exchange process is given by

$$\widetilde{D} = \frac{2D_{\mathrm{p}} \cdot D_{\mathrm{H}}}{D_{\mathrm{p}} + D_{\mathrm{H}}}, \tag{3.4}$$

where D_{p} is the polaron diffusivity and D_{H} is the hydrogen ion diffusivity. Since $D_{\mathrm{p}} \gg D_{\mathrm{H}}$, $\widetilde{D} \approx 2D_{\mathrm{H}}$.

The slow mechanism involves metal vacancies, and is referred as the proton-vacancy incorporation mechanism. This process is rate limited by the diffusion of metal vacancies, which is anisotropic with the fastest diffusion direction parallel to [001] (e.g., *Du Frane et al.*, 2005; *Dohmen et al.*, 2007; *Dohmen and Chakraborty*, 2007). In this case, the chemical diffusivity is thus described by

$$\widetilde{D} = \frac{3D_{\mathrm{V_{Me}}} \cdot D_{\mathrm{H}}}{2D_{\mathrm{V_{Me}}} + D_{\mathrm{H}}}, \tag{3.5}$$

where $D_{\mathrm{V_{Me}}}$ is the metal vacancy diffusivity. Since $D_{\mathrm{H}} \gg D_{\mathrm{V_{Me}}}$, $\widetilde{D} \approx 3D_{\mathrm{V_{Me}}}$.

3.4 Point defect diffusivity results

3.4.1 Inward (hydration) diffusion

A series of IR spectra from which the chemical diffusion coefficients were obtained for sample SC31-3 along the three principal axes are shown in Figure 3.4. The chemical diffusion data in the Appendix B.2 in Figures B.2.1 to B.2.5 illustrate the anisotropy observed in the hydration experiments. Included in these figures are the chemical diffusion coefficients derived from the full IR spectra and the chemical diffusion coefficients for the individual peaks, as well as the experimental uncertainty associated with each diffusion coefficient. For the two samples hydrothermally annealed for less than 1 h with oxygen fugacity buffered by either Fe/FeO (SC14-6) or Ni/NiO (SC16-4), the chemical diffusion coefficient obtained along [100] for the full IR spectra is roughly 1.5 orders of magnitude larger than those for diffusion along [010] and [001]. For the samples hydrothermally annealed longer than 5 h (SC31-2, SC31-3, and SC31-5), the largest chemical diffusivity is associated with diffusion along [001], with diffusion along [100] and [010] occurring at similar rates to one another but both slower by at least a factor of 10 than diffusion along [001]. The chemical diffusivities obtained by analyzing the full FTIR spectra for diffusion along the principal crystallographic directions are listed in Table 3.1. These results are consistent with those reported in previous studies (*Kohlstedt and Mackwell*, 1998; *Demouchy and Mackwell*, 2006). Thus, hydration is characterized by two time scales. The faster hydration step occurs more quickly along [100] than along [010] and [001]. The slower one occurs more quickly along [001] than along [100] and [010].

Figure 3.4: Series of polarized (E//a) IR spectra from sample SC31-3 hydrothermally annealed at 1273 K and 200 MPa for 8 h with oxygen fugacity buffered by Ni/NiO. The numbers on the left are the distance from the edge along each principal direction on the sample: (a) parallel to [100], (b) parallel to [010], (c) parallel to [001].

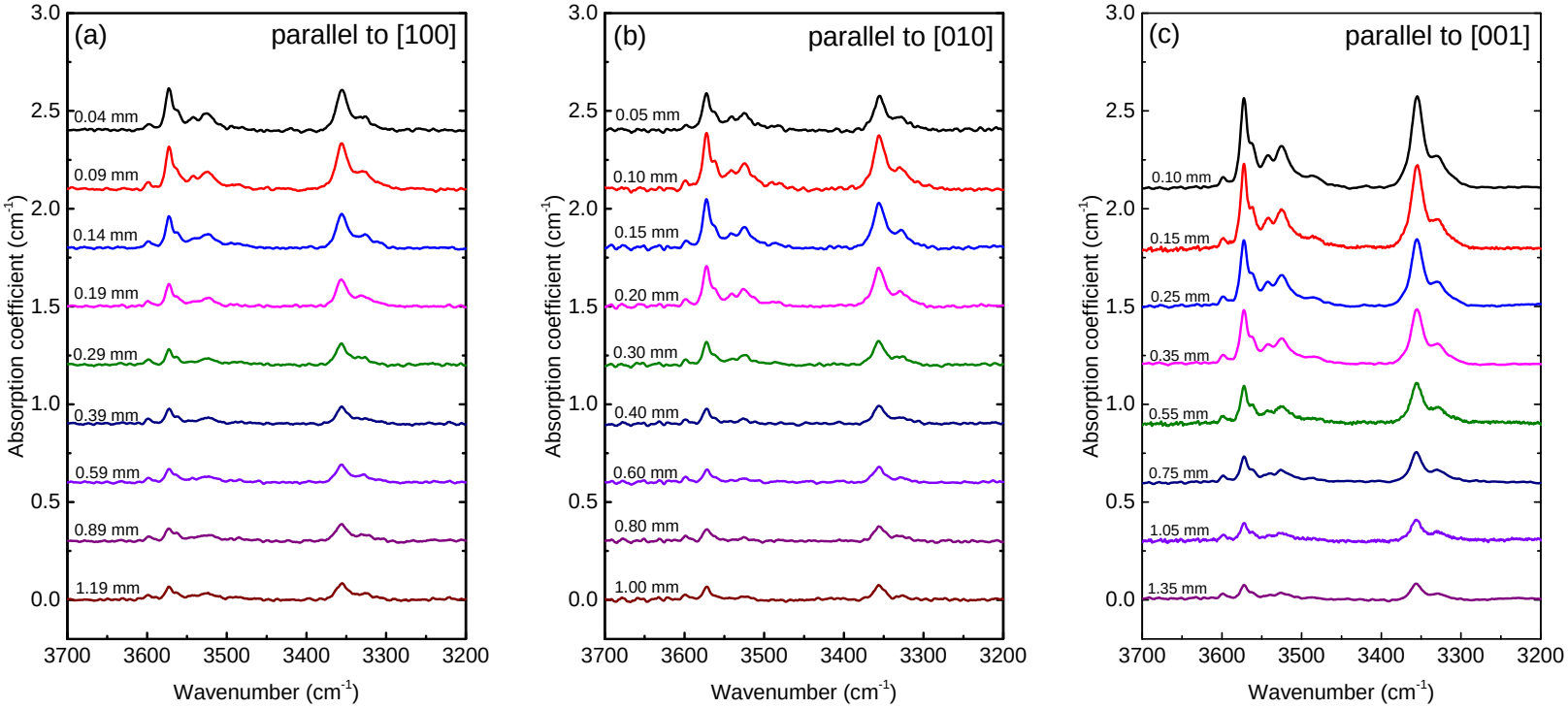

Figure 3.5: OH concentration versus positions (x, y, z) along [100], [010], and [001] of sample SC31-3. Title of each plot has the format of "SC31-3" + "diffusion profile direction (a, b, or c)" + "wavenumber". First three plots in the top row are diffusion profiles of the overall region, 3650-3200 cm^{-1}, in IR spectra along [100], [010], and [001].

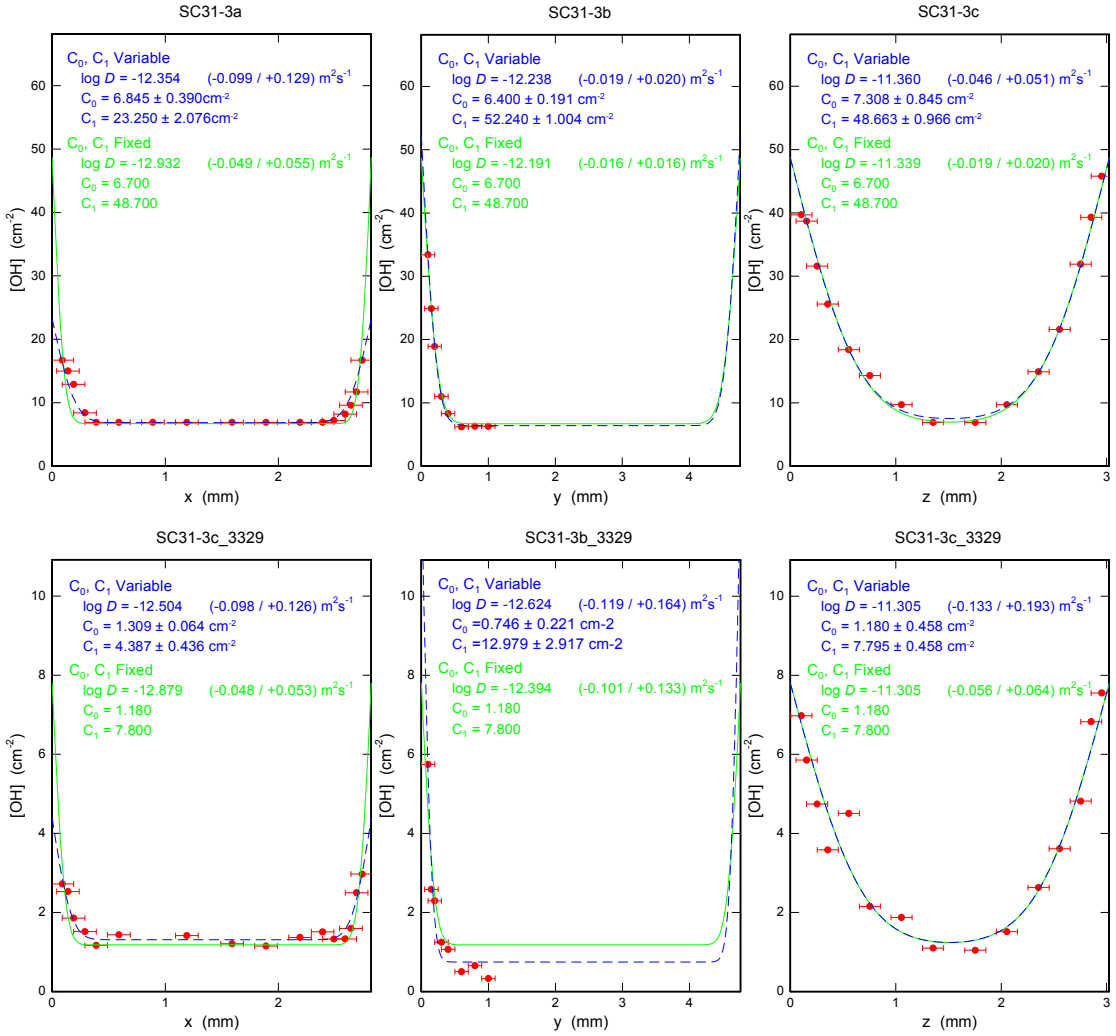

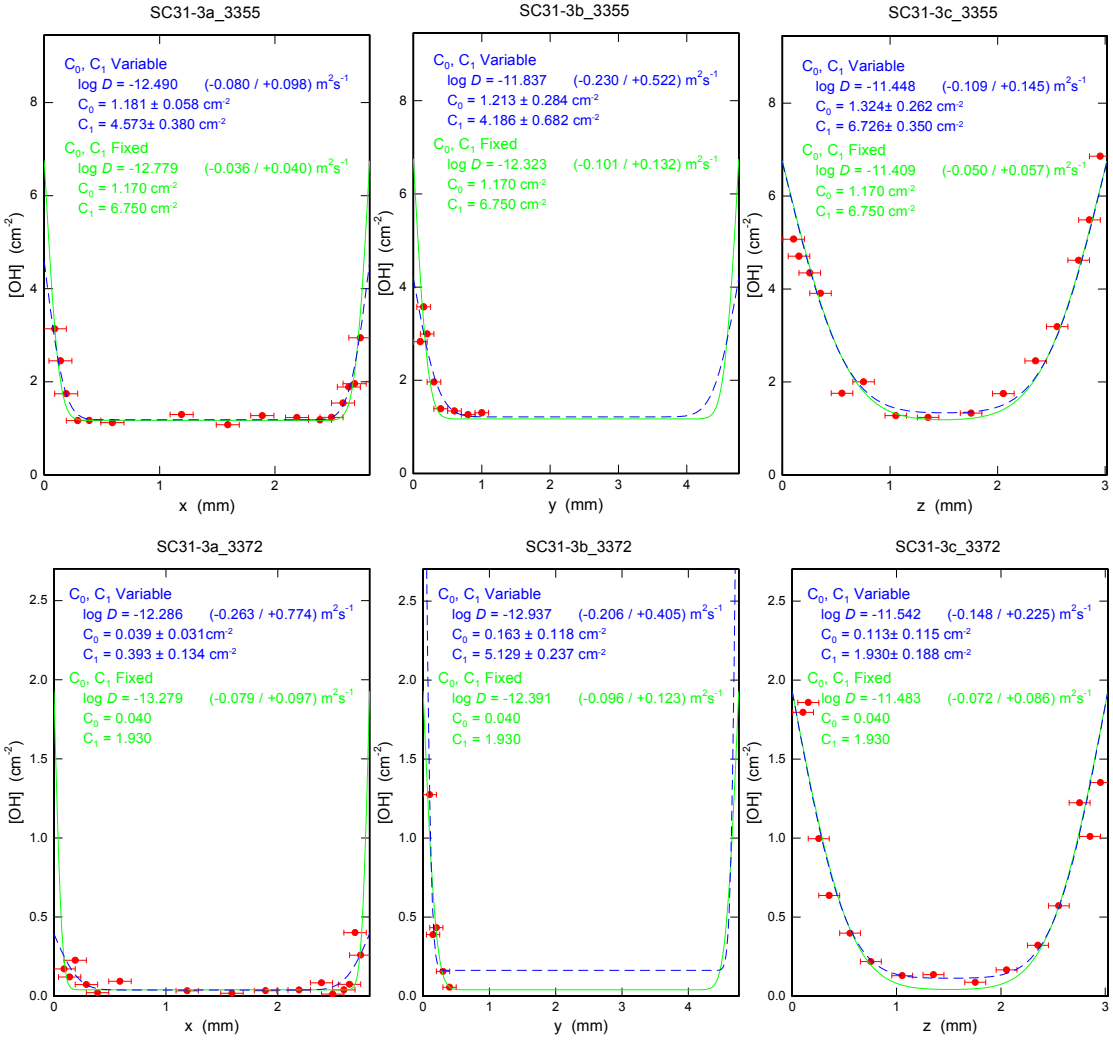
SC31-3a_3355
C0, C1 Variable
log D = -12.490 (-0.080 / +0.098) m2s-1
C0 = 1.181 ± 0.058 cm-2
C1 = 4.573± 0.380 cm-2
C0, C1 Fixed
log D = -12.779 (-0.036 / +0.040) m2s-1
C0 = 1.170 cm-2
C1 = 6.750 cm-2
[OH] (cm-2)
x (mm)
SC31-3b_3355
C0, C1 Variable
log D = -11.837 (-0.230 / +0.522) m2s-1
C0 = 1.213 ± 0.284 cm-2
C1 = 4.186 ± 0.682 cm-2
C0, C1 Fixed
log D = -12.323 (-0.101 / +0.132) m2s-1
C0 = 1.170 cm-2
C1 = 6.750 cm-2
[OH] (cm-2)
y (mm)
SC31-3c_3355
C0, C1 Variable
log D = -11.448 (-0.109 / +0.145) m2s-1
C0 = 1.324± 0.262 cm-2
C1 = 6.726± 0.350 cm-2
C0, C1 Fixed
log D = -11.409 (-0.050 / +0.057) m2s-1
C0 = 1.170 cm-2
C1 = 6.750 cm-2
[OH] (cm-2)
z (mm)
SC31-3a_3372
C0, C1 Variable
log D = -12.286 (-0.263 / +0.774) m2s-1
C0 = 0.039 ± 0.031cm-2
C1 = 0.393 ± 0.134 cm-2
C0, C1 Fixed
log D = -13.279 (-0.079 / +0.097) m2s-1
C0 = 0.040
C1 = 1.930
[OH] (cm-2)
x (mm)
SC31-3b_3372
C0, C1 Variable
log D = -12.937 (-0.206 / +0.405) m2s-1
C0 = 0.163 ± 0.118 cm-2
C1 = 5.129 ± 0.237 cm-2
C0, C1 Fixed
log D = -12.391 (-0.096 / +0.123) m2s-1
C0 = 0.040
C1 = 1.930
[OH] (cm-2)
y (mm)
SC31-3c_3372
C0, C1 Variable
log D = -11.542 (-0.148 / +0.225) m2s-1
C0 = 0.113± 0.115 cm-2
C1 = 1.930± 0.188 cm-2
C0, C1 Fixed
log D = -11.483 (-0.072 / +0.086) m2s-1
C0 = 0.040
C1 = 1.930
[OH] (cm-2)
z (mm)

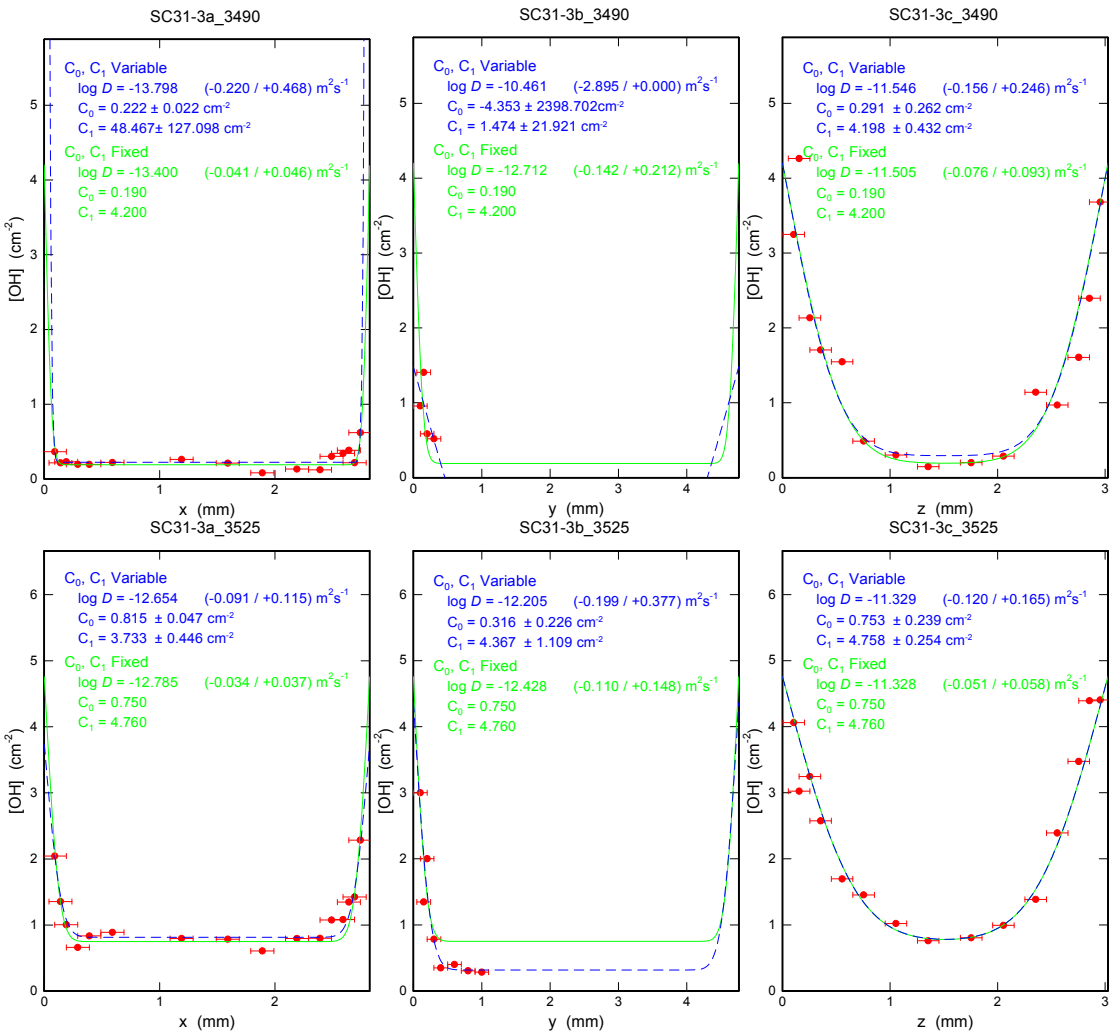
SC31-3a_3490
C0, C1 Variable
log D = -13.798 (-0.220 / +0.468) m2s-1
C0 = 0.222 ± 0.022 cm-2
C1 = 48.467± 127.098 cm-2
C0, C1 Fixed
log D = -13.400 (-0.041 / +0.046) m2s-1
C0 = 0.190
C1 = 4.200
[OH] (cm-2)
x (mm)
SC31-3b_3490
C0, C1 Variable
log D = -10.461 (-2.895 / +0.000) m2s-1
C0 = -4.353 ± 2398.702cm-2
C1 = 1.474 ± 21.921 cm-2
C0, C1 Fixed
log D = -12.712 (-0.142 / +0.212) m2s-1
C0 = 0.190
C1 = 4.200
[OH] (cm-2)
y (mm)
SC31-3c_3490
C0, C1 Variable
log D = -11.546 (-0.156 / +0.246) m2s-1
C0 = 0.291 ± 0.262 cm-2
C1 = 4.198 ± 0.432 cm-2
C0, C1 Fixed
log D = -11.505 (-0.076 / +0.093) m2s-1
C0 = 0.190
C1 = 4.200
[OH] (cm-2)
z (mm)
SC31-3a_3525
C0, C1 Variable
log D = -12.654 (-0.091 / +0.115) m2s-1
C0 = 0.815 ± 0.047 cm-2
C1 = 3.733 ± 0.446 cm-2
C0, C1 Fixed
log D = -12.785 (-0.034 / +0.037) m2s-1
C0 = 0.750
C1 = 4.760
[OH] (cm-2)
x (mm)
SC31-3b_3525
C0, C1 Variable
log D = -12.205 (-0.199 / +0.377) m2s-1
C0 = 0.316 ± 0.226 cm-2
C1 = 4.367 ± 1.109 cm-2
C0, C1 Fixed
log D = -12.428 (-0.110 / +0.148) m2s-1
C0 = 0.750
C1 = 4.760
[OH] (cm-2)
y (mm)
SC31-3c_3525
C0, C1 Variable
log D = -11.329 (-0.120 / +0.165) m2s-1
C0 = 0.753 ± 0.239 cm-2
C1 = 4.758 ± 0.254 cm-2
C0, C1 Fixed
log D = -11.328 (-0.051 / +0.058) m2s-1
C0 = 0.750
C1 = 4.760
[OH] (cm-2)
z (mm)

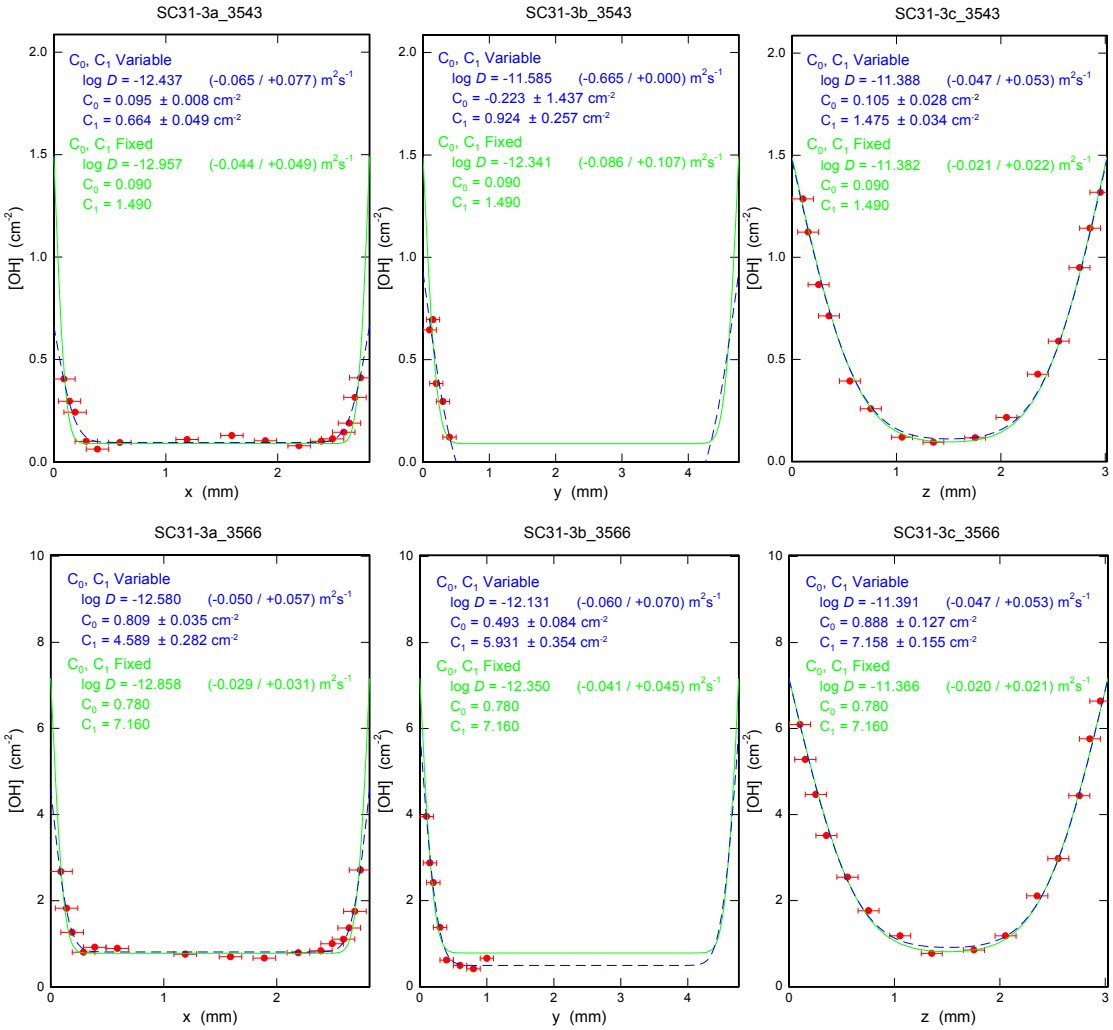
SC31-3a_3543
C0, C1 Variable
log D = -12.437 (-0.065 / +0.077) m2s-1
C0 = 0.095 ± 0.008 cm-2
C1 = 0.664 ± 0.049 cm-2
C0, C1 Fixed
log D = -12.957 (-0.044 / +0.049) m2s-1
C0 = 0.090
C1 = 1.490
[OH] (cm-2)
x (mm)
SC31-3b_3543
C0, C1 Variable
log D = -11.585 (-0.665 / +0.000) m2s-1
C0 = -0.223 ± 1.437 cm-2
C1 = 0.924 ± 0.257 cm-2
C0, C1 Fixed
log D = -12.341 (-0.086 / +0.107) m2s-1
C0 = 0.090
C1 = 1.490
[OH] (cm-2)
y (mm)
SC31-3c_3543
C0, C1 Variable
log D = -11.388 (-0.047 / +0.053) m2s-1
C0 = 0.105 ± 0.028 cm-2
C1 = 1.475 ± 0.034 cm-2
C0, C1 Fixed
log D = -11.382 (-0.021 / +0.022) m2s-1
C0 = 0.090
C1 = 1.490
[OH] (cm-2)
z (mm)
SC31-3a_3566
C0, C1 Variable
log D = -12.580 (-0.050 / +0.057) m2s-1
C0 = 0.809 ± 0.035 cm-2
C1 = 4.589 ± 0.282 cm-2
C0, C1 Fixed
log D = -12.858 (-0.029 / +0.031) m2s-1
C0 = 0.780
C1 = 7.160
[OH] (cm-2)
x (mm)
SC31-3b_3566
C0, C1 Variable
log D = -12.131 (-0.060 / +0.070) m2s-1
C0 = 0.493 ± 0.084 cm-2
C1 = 5.931 ± 0.354 cm-2
C0, C1 Fixed
log D = -12.350 (-0.041 / +0.045) m2s-1
C0 = 0.780
C1 = 7.160
[OH] (cm-2)
y (mm)
SC31-3c_3566
C0, C1 Variable
log D = -11.391 (-0.047 / +0.053) m2s-1
C0 = 0.888 ± 0.127 cm-2
C1 = 7.158 ± 0.155 cm-2
C0, C1 Fixed
log D = -11.366 (-0.020 / +0.021) m2s-1
C0 = 0.780
C1 = 7.160
[OH] (cm-2)
z (mm)

Hydration diffusion profiles for sample SC31-3 obtained for IR absorption bands at 3598, 3572, 3566, 3543, 3525, 3490, 3372, 3355, and 3329 cm^{-1} for the three orthogonal directions are shown in Figure 3.5, and diffusion profiles for the other samples are included in Appendix B.3 in Figures B.3.1 to B.3.5. Some profiles do not have results for all the wavenumbers listed above because the concentration of OH associated with these peaks dropped below the detection limit. Each diffusion profile was fit to Equation 3.3 in two ways: First, each profile was fit with C_0, C_1 and $\widetilde{D}$ as variable parameters. Second, profiles for the three orthogonal directions were fit with fixed values of the largest C_0 and C_1 chosen from the values obtained in the first step for all three directions so that diffusion profiles for the three directions have the same values of C_0 and C_1; $\widetilde{D}$ was then allowed to vary independently for the three directions. Two significant observations require emphasis: (1) All of the IR bands in samples from the hydration anneals yield similar chemical diffusion coefficients, and (2) the directional anisotropy in diffusion is the same for all of the bands for any given sample. All diffusivities fall within a factor of 2 of the average diffusion coefficient. The scale of each error bar depends on the resolution of the peak height derived from the fitting processes.

For the fast mechanism in the hydration diffusion process, the chemical diffusivity was divided by a factor of 2 to obtain the hydrogen diffusivity D_H based on Equation 3.4. For diffusion parallel to the three crystallographic axes, diffusion coefficients were then fit to the Arrhenius relation

$$D^j = D_0^j \quad \exp(-\Delta H^j/\mathrm{R}T), \tag{3.6}$$

where R and T are the gas constant and temperature, D^j is the hydrous defect diffusion coefficient parallel to $j = a,\ b$, or c for diffusion parallel to [100], [010], and [001], respectively, and D_0^j and

ΔH^j are the preexponential term and the activation enthalpy for the diffusion parallel to the jth crystallographic axis.

In Figure 3.6, we combine published data for the proton diffusivity (*Mackwell and Kohlstedt*, 1990) and the results from present study to obtain the best fit values from the $p^\bullet - h^\bullet$ (redox) mechanism with Equation 3.6. The Arrhenius relations are given by

$$D^a_{\mathrm{H}} = 10^{-4.0\pm1.4}\,(\mathrm{m}^2/\mathrm{s}) \times \exp(-\frac{140 \pm 30\,(\mathrm{kJ/mol})}{\mathrm{R}T}) \tag{3.7}$$

$$D^b_{\mathrm{H}} = 10^{-3.8\pm1.4}\,(\mathrm{m}^2/\mathrm{s}) \times \exp(-\frac{180 \pm 30\,(\mathrm{kJ/mol})}{\mathrm{R}T}) \tag{3.8}$$

$$D^c_{\mathrm{H}} = 10^{-6.9\pm3.2}\,(\mathrm{m}^2/\mathrm{s}) \times \exp(-\frac{110 \pm 70\,(\mathrm{kJ/mol})}{\mathrm{R}T}) \tag{3.9}$$

where D^a_{H}, D^b_{H}, and D^c_{H} are the diffusion coefficients of hydrogen ions along [100], [010], and [001], respectively.

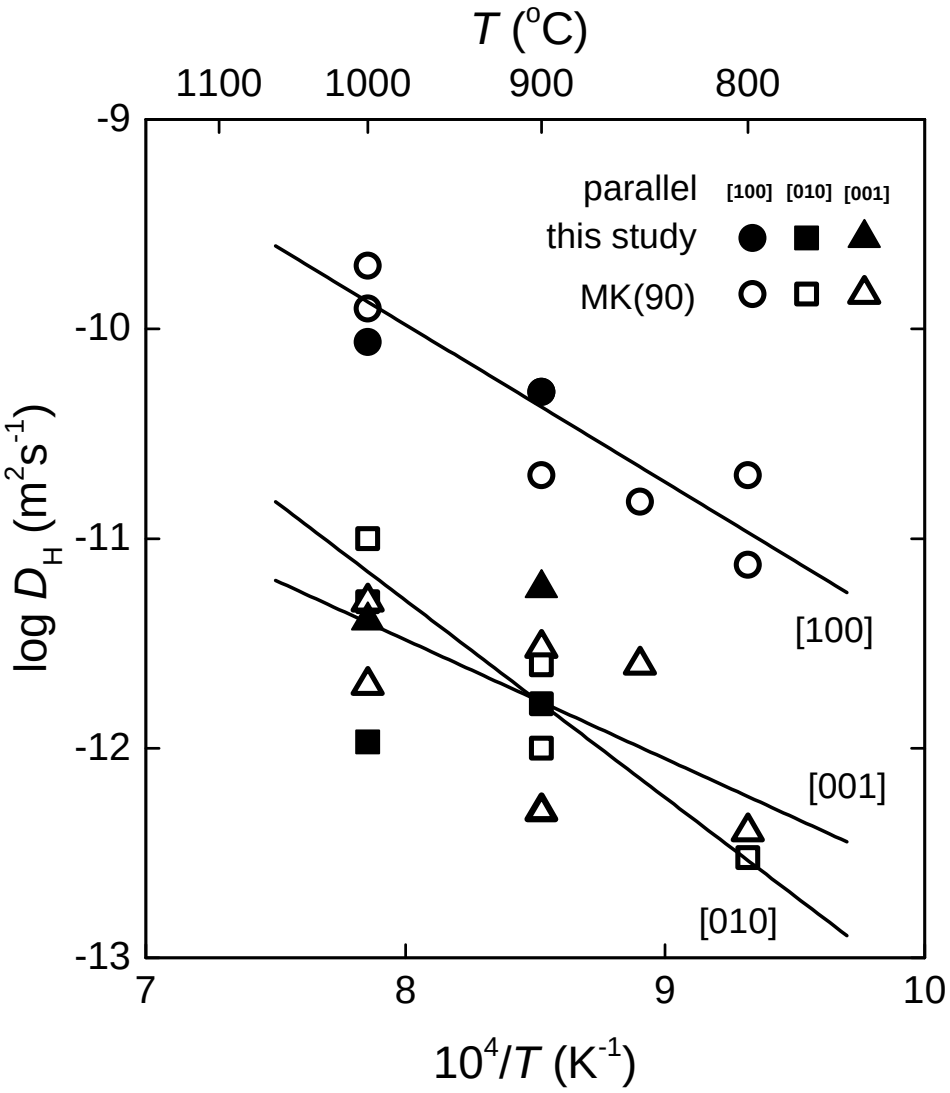

Figure 3.6: Arrhenius plot of diffusivity of hydrogen ions parallel to [100], [010], and [001] from hydration experiments. Open symbols are data from *Mackwell and Kohlstedt* (1990), and the solid symbols are the results of samples SC14-6 and SC16-4 from this study.

For the slow mechanism of hydration, the measured chemical diffusivities were divided by a factor of 3 to obtain the diffusivities for metal vacancies, $D_{\mathrm{V_{Me}}}$, based on Equation 3.5. As illustrated in Figure 3.7, a least-squares fit to the data from present study and results from *Kohlstedt and Mackwell* (1998) and *Demouchy and Mackwell* (2006) yield metal vacancy diffusion coefficients for the $\mathrm{p}^{\bullet} - \mathrm{V}_{\mathrm{Me}}^{//}$ incorporation mechanism in olivine of

$$D^{a}_{\mathrm{V_{Me}}} = 10^{\text{-}2.9\pm6.5}\,(\mathrm{m}^2/\mathrm{s}) \times \exp(-\frac{250 \pm 150\,(\mathrm{kJ/mol})}{\mathrm{R}T}) \tag{3.10}$$

$$D^{b}_{\mathrm{V_{Me}}} = 10^{\text{-}0.3\pm1.3}\,(\mathrm{m}^2/\mathrm{s}) \times \exp(-\frac{310 \pm 30\,(\mathrm{kJ/mol})}{\mathrm{R}T}) \tag{3.11}$$

$$D^{c}_{\mathrm{V_{Me}}} = 10^{1.3\pm1.5}\,(\mathrm{m}^2/\mathrm{s}) \times \exp(-\frac{320 \pm 40\,(\mathrm{kJ/mol})}{\mathrm{R}T}.) \tag{3.12}$$

where $D^{a}_{\mathrm{V_{Me}}}$, $D^{b}_{\mathrm{V_{Me}}}$, and $D^{c}_{\mathrm{V_{Me}}}$ represent the diffusion coefficients of metal vacancy along [100], [010], and [001], respectively. These diffusivity results yield higher values for activation enthalpy than those for the fast diffusion mechanism (Equation 3.7, 3.8, and 3.9).

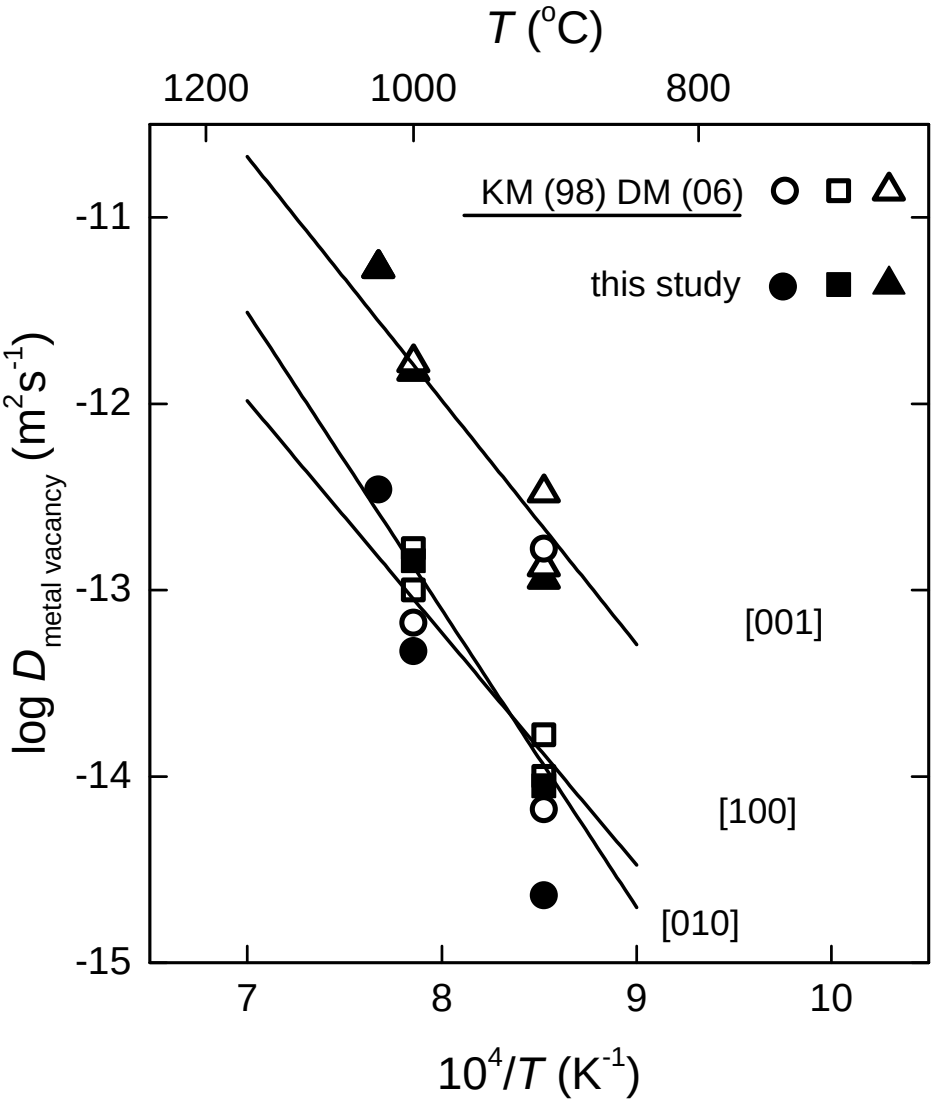

Figure 3.7: Arrhenius plot of diffusivity of metal vacancies parallel to [100], [010], and [001] from hydration experiments. Open symbols are data from *Kohlstedt and Mackwell* (1998) and from *Demouchy and Mackwell* (2006), and the solid symbols are the results of samples SC31-2, SC31-3, and SC31-5 from this study.

3.4.2 Outward (dehydration) diffusion

Chemical diffusion profiles obtained from samples of dehydration diffusion experiments (PI-1914, PI-1918-1, PI-1918-2, and PI-1918-3) illustrate anisotropy similar to that observed for the slower mechanism discussed for hydration experiments, as shown in Appendix B.4, Figures B.4.1 to B.4.4. Due to the resolution limit, we cannot retrieve diffusion profiles for the faster (redox exchange) mechanism in hydration experiments. A series of IR spectra from sample PI-1914 collected along [100] and [001] are shown in Figures 3.8. The diffusion coefficients for the full IR spectra along two principal crystallographic directions were derived from the wavenumber range 3650-3200 cm^{-1}. Due to the relatively small signal-to-noise ratio, we separate the OH-bond related peaks into only two groups, 3650-3450 cm^{-1} and 3450-3200 cm^{-1}, rather than analyzing each individual peaks. This approach is justified based on the results from the hydration experiments in which all of the peaks yield similar values of diffusivity and on visual inspection of the IR spectra from dehydration experiments. Chemical diffusivities were obtained from the diffusion profiles for each group of peaks (Figure B.4.1 to B.4.4) using Equation 3.3 with C_0 and $\tilde{D}$ as variables, and C_1 constrained at 0 corresponding to the depleted condition of hydroxyl concentration at the surface of the sample. The chemical diffusion coefficients for the two groups of peaks agree within experimental uncertainty and exhibit the same anisotropy, as demonstrated in Figure 3.9 and summarized in Table 3.2).

Figure 3.8: Series of unpolarized IR spectra from sample PI-1914 dehydrated at 1253 K and 1 atmosphere for 5 hour with an oxygen fugacity of 10^{-11} Pa. The numbers on the left are the distance from the edge along each principal direction on the sample: (a) parallel to [100], (b) parallel to [001].

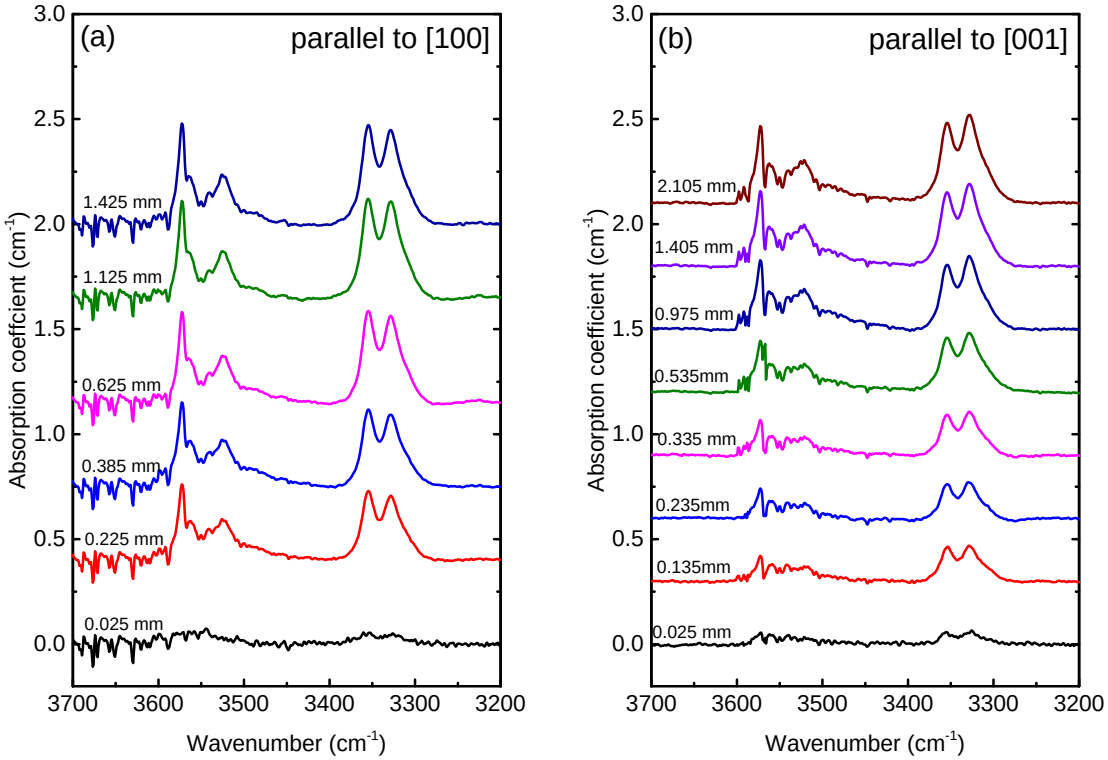

The chemical diffusivities obtained from the dehydration experiments exhibit similar values and the same anisotropy as the slow mechanism in the hydration diffusion experiments, suggesting that dehydration occurs by the process as hydration, that is, through a flux of protons coupled with a parallel flux of metal vacancies. Thus the chemical diffusivities obtained for the full region 3650-3200 cm^{-1} and for the separated groups 3650-3450 cm^{-1} and 3450-3200 cm^{-1} were divided by a factor of 3 to obtain the metal vacancy diffusivity (Equation 3.5). The results are plotted in Figure 3.9. We fit the diffusivities from the overall regions of 3650-3200 cm^{-1} for [100] and [001] with Equation 3.6 to obtain the following results:

$$D^{a}_{V_{Me}}(dehydration) = 10^{-3.4\pm1.7}\,(m^2/s) \times \exp(-\frac{240 \pm 40\,(kJ/mol)}{RT}) \tag{3.13}$$

$$D^{c}_{V_{Me}}(dehydration) = 10^{-5.6\pm1.1}\,(m^2/s) \times \exp(-\frac{150 \pm 30\,(kJ/mol)}{RT}) \tag{3.14}$$

The diffusivities for diffusion along both [100] and [001] agree well with the results from the hydration experiments, thus indicating that dehydration is the counter-process of the slower mechanism in hydration diffusion process, which is rate-limited by the diffusion of metal vacancies in olivine single crystal. Due to detection limit, we did not have the resolution to quantify the faster diffusion process through these diffusion profiles. The faster (redox exchange) diffusion mechanism decreases overall hydroxyl content by only a small amount, such that the diffusion profiles associated with the mechanism are buried in the noise of hydroxyl content measured with IR spectra. For hydration experiments, we can detect a small increase in hydroxyl concentration above near zero starting value, but a small drop of hydroxyl content from an elevated level cannot

be retrieved due to the detection limit.

We fit the metal vacancy diffusivity data based on results from both hydration experiments (the present study, *Kohlstedt and Mackwell* (1998), and *Demouchy and Mackwell* (2006)), and dehydration experiments (the present study). Thus we obtain the following results:

$$D^{a}_{\mathrm{V_{Me}}}(dehydration + hydration) = 10^{-3.3\pm3.3}\,(\mathrm{m}^2/\mathrm{s}) \times \exp(-\frac{240 \pm 80\,(\mathrm{kJ/mol})}{\mathrm{R}T}) \quad (3.15)$$

$$D^{c}_{\mathrm{V_{Me}}}(dehydration + hydration) = 10^{-1.6\pm0.2}\,(\mathrm{m}^2/\mathrm{s}) \times \exp(-\frac{250 \pm 30\,(\mathrm{kJ/mol})}{\mathrm{R}T}) \quad (3.16)$$

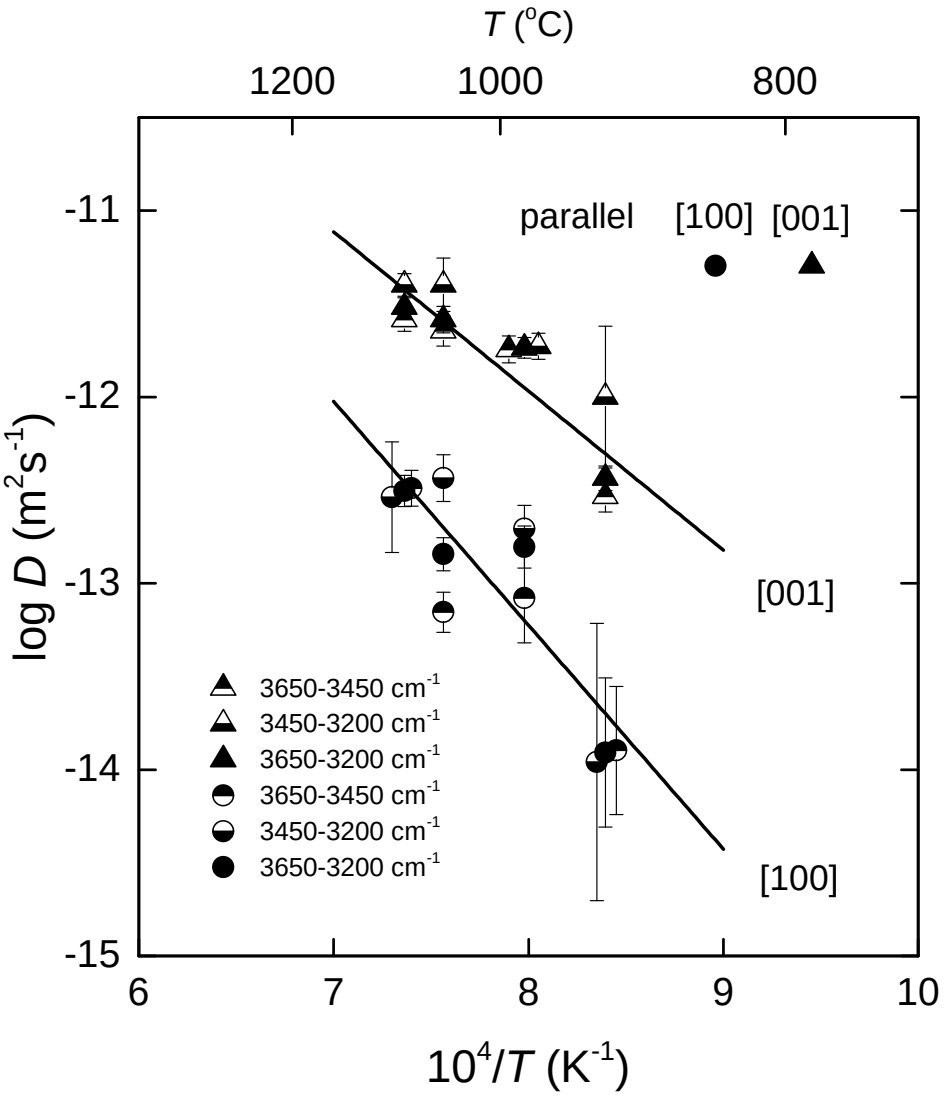

Figure 3.9: Arrhenius plot of metal vacancy diffusivity from dehydration experiments.

3.5 Discussion

3.5.1 Diffusivities of water-derived defects

The diffusivity of electron holes and self-diffusivity of hydrogen were measured in a number of studies. *Sato* (1986) calculated values of $10^{-7.5}$ and $10^{-8.0}$ m^2/s for the diffusivity of electron holes parallel to [010] and [001] based on the diffusivity of metal vacancies and the ratio of mobility of electron holes and metal vacancies obtained from electrical conductivity experiments with the Fe-Mg interdiffusion results of *Misener* (1973) at 1673 K. Extrapolation of proton diffusivities for transport along [010] and [001] from the present study to 1673 K with Equations 3.8 and 3.9 yields smaller values than the calculated polaron diffusivities along [010] and [001] (*Sato*, 1986) by 1.8 and 2.3 log units, respectively. *Hirsch et al.* (1993) measured electrical conductivity of iron-bearing olivine single crystals and obtained a mobility of electron holes as a function of iron content. Calculated diffusivity of electron hole at 1473 K with an iron content of 0.1 is larger than the diffusivity of protons obtained from the present study at the same condition by at least 1.7 log units. Thus, these differences between the diffusivities of polarons and protons justify the assumption used with Equation 3.4 to obtain proton diffusivities from the chemical diffusivities. In addition, *Du Frane and Tyburczy* (2012) reported hydrogen self-diffusion coefficients in olivine, between 1023 and 1173 K at 2 GPa, that are roughly a factor of 0.8 log units lower than the proton diffusivities from this study. The difference indicates that an activation volume, $\sim 7 \times 10^{-6}$ m^3, is required for hydrogen-self diffusion results at high pressure.

Results for the diffusivity of metal vacancies obtained from the slower (incorporation) mechanism are in good agreement with results from other experimental studies, as illustrated in Figure 3.10. The diffusivity of metal vacancies, $D_{V_{Me}}$, can be calculated from the relation $D_{V_{Me}} = D_{Me}/X(V_{Me})$. We used the values for self-diffusivity of metal ions parallel to [100], [010], and [001] from *Dohmen and Chakraborty* (2007) and metal vacancy concentrations, $X(V_{Me})$, from thermogravimetric experiments expressed by Equation 18(b) of *Nakamura and Schmalzried* (1983) to calculate $D_{V_{Me}}$. Values of self-diffusivity obtained at $f_{O_2} = 10^{-7}$ Pa were chosen and normalized to the oxygen fugacity of Ni/NiO with an oxygen fugacity exponent of 1/5 (*Dohmen and Chakraborty*, 2007) for comparison with the results for the diffusivity of metal vacancies from hydration and dehydration experiments in present study. Same calculation has been applied to the results of self-diffusivity of metal ions parallel to [001] from Table 3 in *Chakraborty* (1997). Results for the chemical diffusivity of metal vacancies in polycrystalline olivine obtained by using the parameter in Table 2 from *Nakamura and Schmalzried* (1984) at the oxygen fugacity of Ni/NiO were also included for comparison. These calculated results for the diffusivity of metal vacancies agree very well with the measured diffusivities from the present study, as demonstrated in Figure 3.10. In addition, *Constable and Duba* (2002) calculated metal vacancy diffusivity from electrical conductivity of lherzolite measured as a function of time after changes in the oxygen fugacity, and the reported values also agree well with the metal vacancy diffusivities from this study. Based on these results, diffusivity of metal vacancies parallel to [001] is approximately one order of magnitude higher than those parallel to [100] and [010] at 1173 to 1573 K.

The results of electrical conductivity measurements following an abrupt change in oxygen partial pressure on olivine crystals along [100] (*Wanamaker*, 1994) exhibit two relaxation times, which were interpreted in terms of diffusion of metal vacancies and silicon vacancies. These results for chemical diffusion yielded a difference in diffusivity for metal vacancies and silicon vacancies of less than 0.6 log units, and the diffusivity of metal vacancies parallel to [100] agree well with the results from this study. Meanwhile, *Mackwell et al.* (1988) calculated point defect diffusivities from the time taken for San Carlos olivine specimens to reach a steady-state creep rate after a change in p_{O_2} assuming that strain rate, $\dot{\epsilon}$, and changes in $\dot{\epsilon}$ are rate-limited by the slowest diffusing species. These point defect diffusivities lie within reasonable range compared to the extrapolated curve of the metal vacancy diffusion along [001] (Figure 3.10). These results indicate that the minority defects of silicon and oxygen vacancies have a similar or higher diffusivity than the majority defects of metal vacancies. Thus, there is no significant difference between the diffusivities of silicon vacancies and metal vacancies.

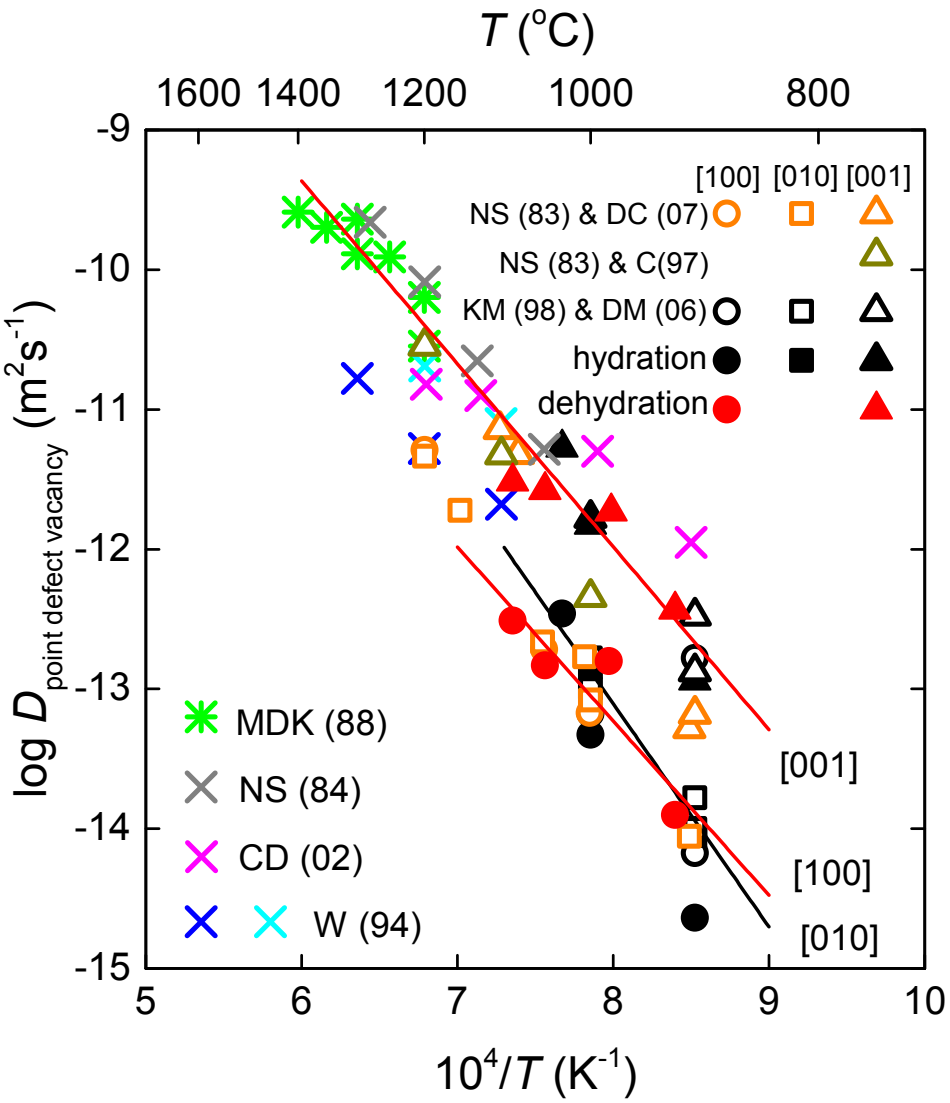

Figure 3.10: Arrhenius plot of metal vacancy diffusivity parallel to [100], [010], and [001] from both hydration (black solid symbols) and dehydration (red solid symbols) experiments. Black open symbols are the results of metal vacancy diffusivity from *Kohlstedt and Mackwell* (1998) and *Demouchy and Mackwell* (2006). "∗" symbols are data from point defect relaxation experiments (*Mackwell et al.*, 1988), orange open symbols are calculated diffusivity for metal vacancies using the concentration of metal vacancies from thermogravimetric experiments (*Nakamura and Schmalzried*, 1983) and measured values of self-diffusivity of metal ions (*Dohmen and Chakraborty*, 2007) parallel to three crystallographic axes, olivine color open symbols are calculated diffusivity for metal vacancies using the measured values of self-diffusivity of metal ions along [001] from *Chakraborty* (1997), gray cross symbols are chemical diffusivity of metal vacancies from *Nakamura and Schmalzried* (1984), cyan and blue "×" symbols represent the diffusivities of metal vacancies (blue) and silicon vacancies (cyan) from electrical conductivity relaxation experiments with olivine single crystals (*Wanamaker*, 1994), and magenta "×" symbols are the metal vacancy diffusivities obtained from electrical conductivity relaxation experiments with lherzolite (*Constable and Duba*, 2002) (see text for more details).

Another significant observation is that, for both the fast and the slow diffusion process, the diffusion coefficients associated with all of the individual absorption bands in the IR spectra, including 3598, 3572, 3566, 3543, 3525, 3490, 3372, 3355, and 3329 cm^{-1}, have similar values; all are within experimental uncertainty of the average value as presented in Appendix B.2 in Figures B.2.1 to B.2.5. Similarly, the dehydration diffusion experiments also yield for the two separated Group I and Group II bands (3650-3450 and 3450-3200 cm^{-1}) that are in good agreement in terms of magnitude, temperature dependence, and anisotropy as illustrated in Figure 3.9. These observations provide strong evidence that hydrogen ions associated with the individual bands in an IR spectrum diffuse by the same mechanism.

In contrast, *Padrón-Navarta et al.* (2014) reported that different hydrous defects in forsterite and Ti-doped forsterite have diffusivities that differ by several orders of magnitude. The fastest species associated with the band at 3220 cm^{-1} was assigned to hydrogen associated with Mg-vacancy, the slower species associated with the bands at 3572 and 3525 cm^{-1} were interpreted as hydrogen associated with titanium defects, and the slowest species associated with bands at 3613, 3566, 3542 cm^{-1} were assigned to hydrogen associated with silicon vacancies. In forsterite, Ti^{4+} is strongly bonded either tetrahedrally or octahedrally with oxygen ions. Thus, on the one hand, hydrous defects associated with Ti ions, such as $Ti^{\bullet\bullet}_{Me} - 2H^{//}_{Si}$, might be expected to have a lower mobility if Ti ions effectively trap H^+ ions. On the other hand, the forsterite samples doped with titanium used in their experiments were grown under wet hydrous conditions leading to the possibility that grain boundary migration incorporated a population of non-equilibrium hydrous defects, including point defect, planar defects, or nano-scale water inclusions. These hydrous defects would

work as a secondary water supply that extend the duration of the subsequent dehydration process, thus resulting in an apparently slow chemical diffusion.

3.5.2 Hydrogen diffusion models

Inward diffusion model

Charge neutrality in natural, iron-bearing, olivine under dry conditions is governed by electron holes and metal vacancies (e.g., *Dohmen and Chakraborty*, 2007). An increase in hydrogen fugacity under hydrous conditions facilitates the consumption of electron holes and creates protons by the redox reaction at the specimen surface as described by the reaction

$$H_2O(g) + 2Fe^{\bullet}_{Me} \quad \rightleftharpoons \quad 2H^{\bullet}_{i} + 2Fe^{\times}_{Me} + \frac{1}{2}O_2(g) \tag{3.17}$$

using the Kröger-Vink notation (*Kröger and Vink*, 1956). From previous studies (*Kohlstedt and Mackwell*, 1998) and the results of the present study, the fast diffusion process in the hydration experiments thus involves an inward flux of protons coupled and charge compensated with a counterflux of electron holes, as illustrated as the t_1 phase in Figure 3.11. Thus, diffusion of hydrogen will form (1) an interstitial hydrogen defect, $H^{\bullet}_{i}$, and supply hydrogen ions to form (2) a point defect associate formed between a proton and a metal vacancy (e.g., $\{(OH)^{\bullet}_{O} - V^{//}_{Me}\}^{/}$) or (3) a point defect associate formed between a proton and a silicon vacancy (e.g., $\{(OH)^{\bullet}_{O} - V^{////}_{Si}\}^{///}$, shown as the t_2 phase in Figure 3.11.

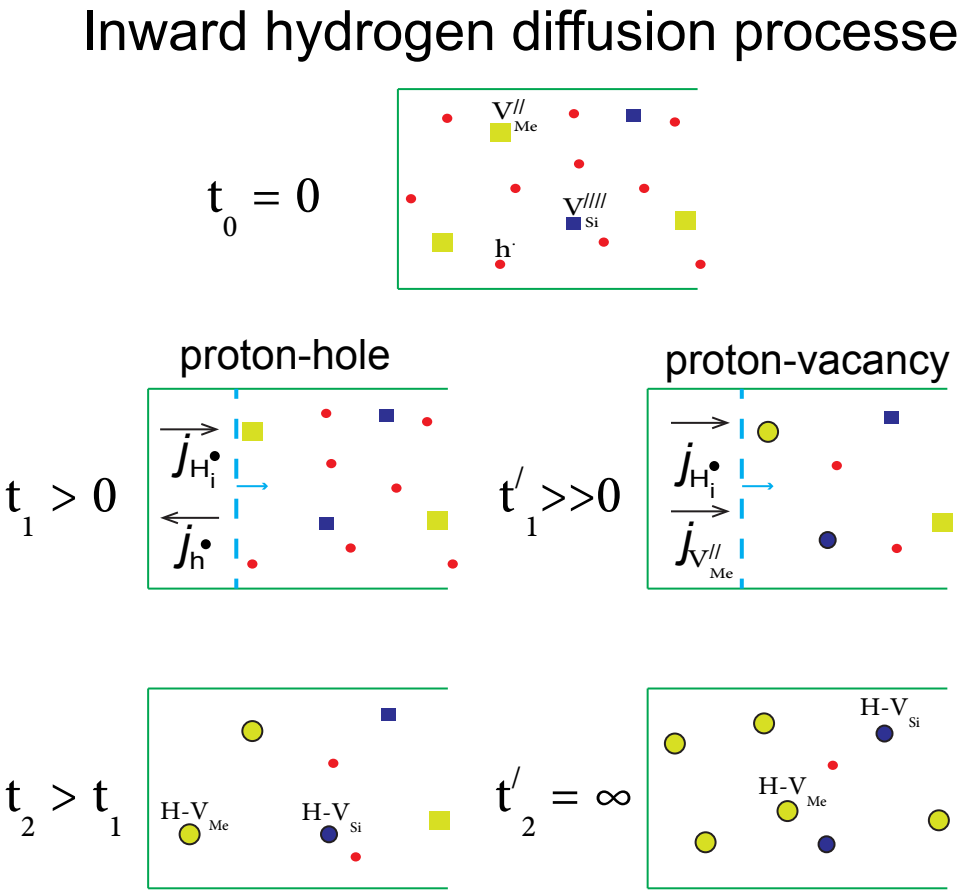

Figure 3.11: Schematic diagram of the mechanisms of diffusion of hydrous point defects in olivine from a time series perspective. Left column presents the fast mechanism that is rate-limited by the diffusion of protons, while the right column presents the slow mechanism that is rate-limited by the diffusion of metal vacancies. Red circle, green square and blue square represent the electron hole, metal vacancy, and silicon vacancy, respectively, which are intrinsic point defects in olivine. Green and blue circles are hydrogen associated point defect species as labeled in the figures. Blue dash lines delineate the hydrogen diffusion front for the fluxes labeled under the black arrows.

As for the slow diffusion process, results from the present study as well as previous studies (*Kohlstedt and Mackwell*, 1998; *Demouchy and Mackwell*, 2006) present in Figure 3.10 suggest that this slow diffusion process occurs by the inward flux of protons coupled with a parallel inward flux of metal vacancies, the t_1' phase in Figure 3.11. The concentration of metal vacancies in the sample consequently increases due to the inward flux of metal vacancy. The chemical reaction at the specimen surface is

$$\mathrm{H_2O(g)} + \mathrm{Me_{Me}^{\times}} \quad \rightleftharpoons \quad 2\mathrm{H_i^{\bullet}} + \mathrm{V_{Me}^{//}} + \mathrm{MeO}. \tag{3.18}$$

The diffusion of interstitial hydrogen ions is then rate-limited by the diffusion of metal vacancies.This slow mechanism thus becomes dominant in increasing the hydrogen content after the fast hydration process is complete, as shown the t_1' phase in Figure 3.11.

Outward diffusion model

The chemical diffusion coefficient for outward diffusion in our experiments is larger for transport along [001] than for transport along [010] and [001]. This observation indicates that the outward diffusion of protons is coupled with a parallel flux of metal vacancies as in the case of the slow mechanism in the inward diffusion process. Thus, the defect diffusion coefficient is calculated by applying Equation 3.5 to the chemical diffusion coefficients. The results for dehydration kinetics agree well with the slow diffusion rates measured in the hydration experiments for all three crystallographic orientations.

Because of the detection limit, it was not possible to resolve the fast mechanism in the outward diffusion results. In the case of hydration, the fast diffusion process adds a small amount of hydrogen to an initially near-zero baseline. In contrast, in the case of dehydration, the fast diffusion process removes a small amount of hydrogen from an initially large background. However, in the dehydration case, the gradient of polaron concentration does drive an inward flux of polarons coupled with a counter flux of protons, helping to deplete the concentration of hydrous defects.

3.6 Application to ascent rates of mantle xenoliths

Several studies have measured dehydration diffusion profiles in olivine grains in peridotite mantle xenoliths (e.g., *Demouchy et al.*, 2006; *Peslier and Luhr*, 2006; *Peslier et al.*, 2008; *Denis et al.*, 2013; *Hilchie et al.*, 2014; *Peslier et al.*, 2015). Generally these samples exhibit features common to IR spectra from mantle-derived olivine (*Miller et al.*, 1987; *Ingrin and Skogby*, 2000) including the peaks located at 3572, 3525, 3353, 3330 cm^{-1}. Results from the present study have demonstrated that all the major peaks exhibit similar growth or decay rates. In addition, the similarity between the diffusivities obtained from hydration and dehydration experiments justifies the validity of using the diffusivities obtained from hydration experiments to calculate the ascent rates of olivine xenolith host magma. The hydrogen diffusivities reported by *Padrón-Navarta et al.* (2014) predict ascent rates of xenoliths at least 3 orders of magnitude smaller. More importantly, no significant disparity for the diffusivities associated with the various hydrogen species were observed in the diffusion profiles from natural olivine grains (e.g., *Demouchy et al.*, 2006; *Denis et al.*, 2013; *Peslier et al.*,

2015). Thus, rates of magma ascent should remain rapid, several meters per second, regardless of the diffusivity of hydrogen obtained from various bands from IR spectra as reported in the earlier studies.

3.7 Conclusion and implication

Through this study of inward or outward diffusion of hydrogen in olivine, we systematically measured diffusion profiles of individual bands with specific wavenumbers in IR spectra.

★In hydration experiments, all of the major bands yield similar diffusion rates for both the fast mechanism, $p^{\bullet} - h^{\bullet}$, and the slow mechanism, $p^{\bullet} - V_{Me}^{//}$.

★The fast mechanism is rate-limited by the diffusion of hydrogen with the fastest rate of diffusion along [100]. The slow mechanism is rate-limited by the diffusion of metal vacancies, with the fastest rate of diffusion along [001].

★The diffusion coefficients determined for all of the individual bands are in reasonably good agreement with one another. The same diffusion properties for all the hydrous defects associated with the major bands of specific wavenumbers in an IR spectrum suggest that hydrogen diffusion in olivine through a single mechanism.

★Results of dehydration experiments also yield diffusivities, activation enthalpy, and anisotropy that agree within uncertainty with those from hydration experiments with the slower diffusion mechanism.

★Therefore, we propose that hydrogen diffuse both inward and outward through the crystal lattice

in the form of interstitial protons that are formed or annihilated at the surface of a sample (Equation 3.17 and 3.18).

★Thus, diffusivity measured from inward H diffusion can appropriately be used to calculate ascent times of xenoliths obtained from out H diffusion profiles in olivine grains.

Chapter 4

Diffusivity of silicon ions in iron-bearing olivine single crystal

4.1 Introduction

Diffusivity of silicon ions is an important physical parameter for understanding flow of the mantle, which is essential for tectonic activity on Earth and plays a key role in the solid earth geodynamics. In particular, diffusion of Si is important for understanding the rheological properties of olivine, the major constituent mineral in the upper portion of the Earth's mantle. Thus, the deformation behavior of olivine has been the subject of a great number of modelling and experimental studies (e.g. *Carter and Ave'Lallemant*, 1970; *Blacic*, 1972; *Poumellec and Jaoul*, 1984; *Poirier*, 1995; *Evans and Kohlstedt*, 1995; *Mei and Kohlstedt*, 2000a,b; *Hirth and Kohlstedt*, 2003; *Karato and Jung*, 2003; *Boioli et al.*, 2015). Experimental results of diffusional creep of olivine (e.g., *Cooper and*

Kohlstedt, 1984; *Hirth and Kohlstedt*, 1995; *Weertman*, 1999; *Mei and Kohlstedt*, 2000a) assert that deformation is limited by the diffusion processes along grain boundaries. Meanwhile, models for dislocation creep suggest that climb of dislocations is the rate-controlling step for high-temperature steady-state creep (e.g., *Weertman*, 1955, 1957; *Poirier*, 1985, pages 126-136; *Karato*, 2008, pages 143-164), and climb velocity of dislocation is also a function of ionic self-diffusivity (e.g., *Kohlstedt and Hansen*, 2015). Thus, plastic deformation is limited by ionic diffusion (*Weertman et al.*, 1978; *Cannon and Langdon*, 1988; *Evans and Kohlstedt*, 1995; *Weertman*, 1999; *Dohmen et al.*, 2002a; *Kohlstedt*, 2006). Meanwhile, silicon has the lowest ionic diffusivity among the major constituents (Mg, Fe, Si, O) in olivine (*Buening and Buseck*, 1973; *Hermeling and Schmalzried*, 1984; *Gérard and Jaoul*, 1989; *Ryerson and Durham*, 1989; *Houlier et al.*, 1990; *Chakraborty*, 1997; *Dohmen et al.*, 2002a; *Dohmen and Chakraborty*, 2007). Thus, knowledge of diffusivity and activation energy of silicon diffusion is critical to the understanding of olivine's rheological properties and dynamic features for the Earth's mantle.

Results of silicon diffusion obtained from experimental studies have shown a discrepancy of self-diffusivity and associated activation energy. Under anhydrous condition, *Houlier et al.* (1990) measured silicon self-diffusivity using isotope ^{30}Si in single crystals of San Carlos olivine at 1403 to 1803 K and obtained an activation energy $Q_{\mathrm{c}}^{\mathrm{dry}} = 291 \pm 15$ kJ/mol from the results of silicon diffusivity. *Dohmen et al.* (2002a) measured silicon self-diffusivity using ^{29}Si in single crystals of Nanga Parbat, Pakistan, olivine ($\sim$ Fo93) at 1373 to 1774 K, and this newer data set exhibited smaller values of silicon diffusivity by 0.5 to 1 log unit and a larger value for the activation energy, $Q_{\mathrm{Si}}^{\mathrm{dry}} = 530 \pm 40$ kJ/mol. *Dohmen et al.* (2002a) attributed the difference between values of

silicon diffusivity and activation energy to the artifacts associated with convolution effects caused by the very short diffusion distance and detecting limits on the spatial resolutions of the analytical instruments used to measure the diffusion profiles. The newer results agree well with the activation energy obtained from creep deformation experiments of olivine-rich rocks, $Q_{\mathrm{c}}^{\mathrm{dry}} \approx 530$ kJ/mol (*Hirth and Kohlstedt*, 2003). In addition, newer results from *Fei et al.* (2012) measured silicon diffusivity parallel to [010] from 1 atm to 13 GPa at 1600 to 1800 K using single crystals of synthetic forsterite and obtained larger values of silicon diffusivity than those from *Dohmen et al.* (2002a). This newer data set yielded an activation volume and activation energy of $1.7 \pm 0.4\,\mathrm{cm}^3$/mol and $Q_{\mathrm{Si}}^{\mathrm{dry}} = 410 \pm 30$ kJ/mol, respectively. These results for silicon diffusivity and $Q_{\mathrm{Si}}^{\mathrm{dry}}$ under dry conditions exhibit disagreements. Thus, it is important to revisit this problem in an attempt to explain the discrepancy between these studies. In this study, we measured silicon self-diffusion coefficient parallel to [010] using natural single crystals of San Carlos olivine ($\sim$ Fo90) and examined the convolution effects embedded in the measurements that may cause artifacts and lead to different values for silicon diffusivity and activation energy.

4.2 Silicon diffusion experiments

Crack-free single crystals of San Carlos olivine with no visible inclusions were selected for diffusion experiments. They were orientated using Laue X-ray diffraction and cut into slabs with normal vectors parallel to [010]. These slabs were polished using lapping films from 30 μm down to 0.5 μm, and then polished with colloidal silica for over one hour to obtain a surface roughness

of less than 10 nm. Olivine discs with a diameter of 1.5 mm were core drilled out of the single crystal slabs. Further thin film deposition was applied using pulsed laser deposition (PLD) at Ruhr Universität Bochum, Germany. Details of the facility and characterization of the thin films can be found in (*Dohmen et al.*, 2002b). Composition of the pellet for thin film deposition was $(MgO)_{1.8}(Fe_2O_3)_{0.1}(^{29}SiO_2)_{0.5}(Si^{18}O_2)_{0.5}$, similar to that of the substrate single crystal in terms of iron and silica content, $\sim Fo_{90}$. The composition of the thin film was confirmed with Rutherford backscattering spectroscopy (RBS) at Ruhr Universität Bochum, Germany. The amorphous thin film layer with a thickness of $\sim$500 nm was then crystallized into a polycrystalline layer through a pre-diffusion anneal at 1173 K for 20 hour. Oxygen fugacity was buffered by a flow mixture of CO-CO_2, volumetrically 20/80, at 10^{-14} bar. Surface roughness on the crystalized thin film layer is approximately 20 nm with a grain size of $\sim$100 nm, as shown in the SEM image (Figure 4.1) and the atomic force microscopy (AFM) image (Figure 4.2 and 4.3) of a diffusion sample's surface.

Diffusion experiments were carried out using 1 atmosphere furnace equipped to flow a mixture of CO-CO_2 and to monitor oxygen partial pressure. A diffusion couple of single crystals with thin film layers facing each other (Figure 4.4) were placed into a container fabricated from an olivine single crystal. A lid made of olivine single crystal was placed on top of the diffusion couple and onto the olivine container to help maintain a stable chemical field to minimize evaporation that may occur from the surfaces of the sample at high temperature. The furnace was heated to 100 K below the target temperature at a rate of 400 K/h and then increased to the target temperature within 30 min. Temperature at the sample was checked using a travel thermal couple and monitored for

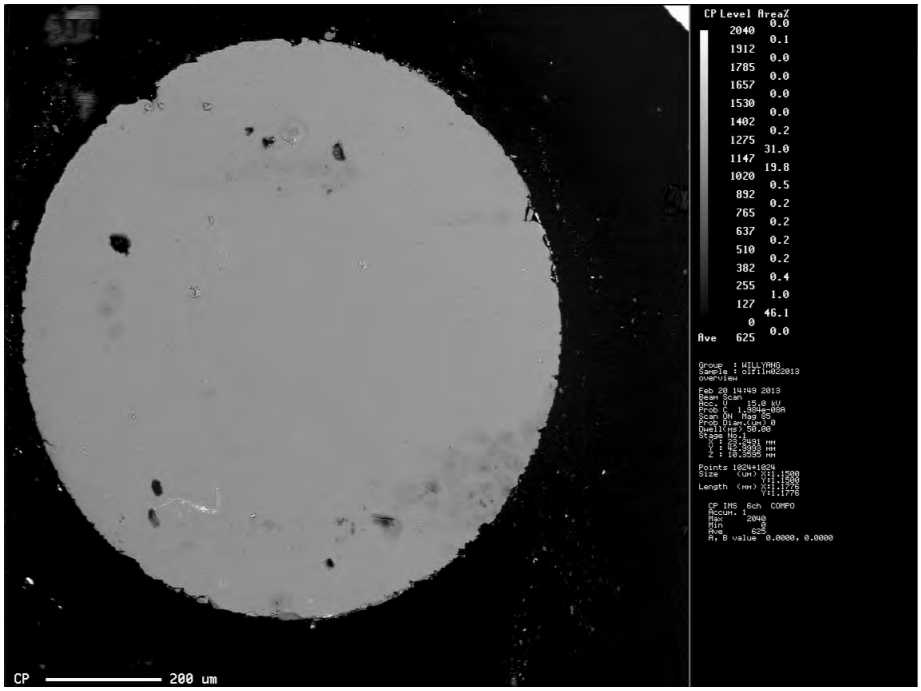

Figure 4.1: SEM image of the olivine diffusion sample's surface after the pre-diffusion anneal step.

temperature variation throughout diffusion experiments.

4.3 Diffusion profile measurements and analytical methods

4.3.1 SIMS measurements

Diffusion profiles of isotope ^{29}Si were measured in an ionprobe equipped with secondary ion mass spectrometry (SIMS) attachment (Cameca IMS 1270) in the depth sputtering mode using a primary Cs^+ beam at the University of Edinburgh, UK. The primary current of the ion beam was set stabilized in the range of 4.0-6.0 nA, indicating instrument stability and measurement consistency. The field aperture was set at 1500 μm, and the raster size was 50 μm. An electron multiplier was

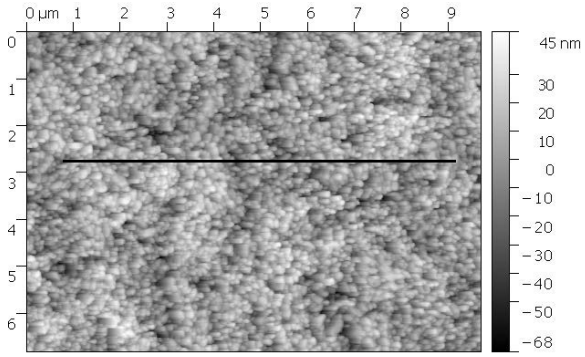

Figure 4.2: AFM map of surface height difference for a pre-diffusion sample.

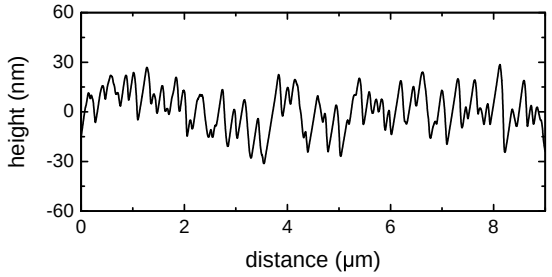

Figure 4.3: Height profile along the black line in Figure 4.2 representing sample surface roughness.

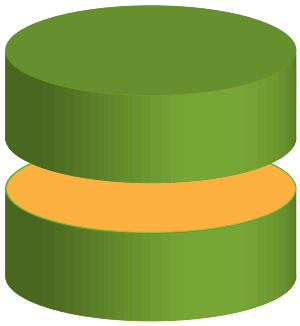

Figure 4.4: Silicon diffusion couple with polycrystalline thin film layer facing each other. Yellow areas are thin film deposited on olivine substrates.

chosen as the detector to improve the measurement spatial resolution. Final depth of ion beam raster process was measured using surface height image both with the AFM at the University of Minnesota and white light interference microscopy at Ruhr Universität Bochum, Germany.

The convolution factor can have a strong effect on diffusion profiles versus depth (e.g., *Ganguly et al.*, 1988 and *Dohmen et al.*, 2002a); this artifact results in an anomalously high diffusivity. It

can be caused by either atomic mixing or surface roughness (*Hofmann*, 1994). The effect of atomic mixing is mainly caused by the detection limit of SIMS associated with its working conditions. Improper setup for SIMS may cause artifacts to diffusion profiles such as tiled or non-flattened concentration profiles of isotope in thin film (source) and substrate (reservoir). Surface roughness of diffusion samples also plays a key factor causing a convolution effect due to sample preparation or material evaporation that occurs in long diffusion anneals at high temperatures. As an ion beam sputters at the sample surface and propagates down to the material beneath, roughness on the surface can be magnified and lead to an averaging effect to materials of different isotope concentrations. As illustrated in Figure 4.5, if the isotope enriched layer (lighter yellow) has a rough topography, it will cause higher averaging effect to the materials at different depths and lead to a slower sputtering rate on the thin film. A similar convolution effect can also be caused if the sample is mounted tilted on sample holder for SIMS measurements. Thus, it is of great importance to evaluate convolution factor involved in measured diffusion profiles.

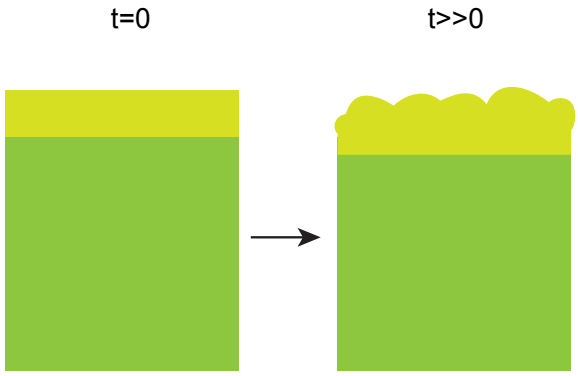

Figure 4.5: Sketch for surface roughness due to evaporation at high temperature causing convolution effect.

To obtain optimum conditions for less convolution effect, it is important to balance between sputtering rate and spatial resolution of SIMS measurement. Factors that increase sputtering rate (e.g. higher voltage, smaller raster for a given beam energy, larger integration times for counting signals) with better detection limits can reduce spatial resolution thus increase convolution effect. Thus, one needs to estimate reasonable overall drilling time so that ions beam can stay stable with enough signal strength to obtain good counting statistics.

We determined the convolution factor caused by roughness of the surface and irregularity of the film-substrate interface by measuring ^{29}Si profiles on pre-diffusion (zero-time) samples. The zero-time profile was fit to a smeared profile of an ideal step function convolved with a Gaussian function to determine the convolution factor, ϵ, (*Ganguly et al.*, 1988):

$$C_{\text{conv}}(x,t) = \int_{-\infty}^{+\infty} C(x') \cdot G(x-x')dx', \tag{4.1}$$

where $G(x) = \frac{1}{\sqrt{2\pi\epsilon}} \exp(\frac{-x^2}{2\epsilon^2})$. This result provides a minimum estimation for the convolution effect since higher surface roughness may be caused through the following long diffusion anneals at high temperature.

4.3.2 Diffusion profile model

An analytical solution for a one-dimensional system with a layer of finite thickness (constant diffusion coefficient, D_{film}) with zero flux at the surface on a semi-infinite substrate (constant diffusion

coefficient, independent on the isotope distribution, D_{sub}) is given by *Lovering* (1936):

$$\frac{C_{\text{film}}(x,t) - C^0_{\text{sub}}}{C^0_{\text{film}} - C^0_{\text{sub}}} = -\frac{1+p}{2}\text{erf}(\frac{x}{2\sqrt{D_{\text{film}}t}}) + \frac{1+p}{2}\sum_{n=1}^{\infty}(-p)^{n-1}[\text{erf}(\frac{d\cdot n + x}{2\sqrt{D_{\text{film}}t}}) - p\cdot\text{erf}(\frac{d\cdot n - x}{2\sqrt{D_{\text{film}}t}})],$$

$$\frac{C_{\text{sub}}(x,t) - C^0_{\text{sub}}}{C^0_{\text{film}} - C^0_{\text{sub}}} = -\frac{1-p}{2}\text{erf}(\frac{x}{2\sqrt{D_{\text{sub}}t}}) + \frac{1-p^2}{2}\sum_{n=1}^{\infty}(-p)^{n-1}\text{erf}(\frac{d\cdot\sqrt{D_{\text{sub}}/D_{\text{film}}}\cdot n + x}{2\sqrt{D_{\text{sub}}t}}), \tag{4.2}$$

$$p := \frac{\sqrt{D_{\text{film}}}D_{\text{sub}} - \sqrt{D_{\text{sub}}}D_{\text{film}}}{\sqrt{D_{\text{film}}}D_{\text{sub}} + \sqrt{D_{\text{sub}}}D_{\text{film}}},$$

where x is the distance from the film-substrate interface with $x > 0$ for the substrate, h is thin film thickness, and $d = 2h$; C^0_{film} and C^0_{sub} represent the initial concentration in the thin film and the substrate at $t = 0$, respectively.

Because of the symmetrical shape of our diffusion profiles, similar values of D_{film} and D_{sub} were obtained from fitting our results to Equation 4.2. With $D_{\text{film}} = D_{\text{sub}}$, the solution to the Fick's second law with the convolution factor can be simplified into the following expression (*Ganguly et al.*, 1988):

$$C = \frac{C_{\text{film}} + C_{\text{sub}}}{2} + \frac{C_{\text{film}} - C_{\text{sub}}}{2}\{\text{erf}(\frac{x}{2\sqrt{D_{\text{Si}}t}}) + \frac{2x\cdot\exp\{-(\frac{x}{2\sqrt{D_{\text{Si}}t}})^2\}}{(2\sqrt{D_{\text{Si}}t})^3\cdot\sqrt{\pi}}\epsilon^2\}, \tag{4.3}$$

where ϵ is convolution factor. Location of the interface between the thin film and the substrate is identified as $C(x = 0) = (C_{\text{film}} + C_{\text{sub}})/2$, constrained by the mass balance condition between the two sides of the interface. Thus, we obtained the silicon diffusivity and the convolution factor

from fitting diffusion profile to the Equation 4.3. Values of the convolution factor should be bigger than that from the zero-time profile (Equation 4.1) because long-time anneals at high temperatures resulted in evaporation on material from the sample surface, causing a more significant convolution effect.

Thus, deconvoluted profiles were obtained by deleting the convolution term in Equation 4.3:

$$C = \frac{C_{\text{film}} + C_{\text{sub}}}{2} + \frac{C_{\text{film}} - C_{\text{sub}}}{2}\text{erf}(\frac{x}{2\sqrt{D_{\text{Si}}t}}). \tag{4.4}$$

4.4 Silicon diffusion results

Results of silicon diffusivity are summarized in Table 4.1, and diffusion profiles with various fitting parameters are shown in Figures 4.6 to 4.9. Diffusion profiles were firstly fit with variable values for C_{film}, C_{sub}, and ϵ. Diffusion profiles were also fit with fixed values for C_{film} and C_{sub} as calculated from the average elevated concentration in regions of the plateau in the concentration profile in the film and the flatten-out concentration in regions of the profile tail in the substrate. Deconvolved profiles were also plotted in the figures from applying Equation 4.4 to the red curves.

Silicon diffusivity results exhibit a temperature dependence, as illustrated in Figure 4.10. A least-squares fit yields the following expression:

$$D_{\text{Si}} = 10^{-3.6\pm3.8}\ \text{m}^2/\text{s} \times \exp(\frac{-5.6 \pm 1.2 \times 10^2\ \text{kJ}}{RT}.) \tag{4.5}$$

Table 4.1: Experimental settings and results of silicon diffusion parallel to [010]. Oxygen fugacity was 10^{-9} Pa controlled with a mixture flow of CO-CO_2. Sample SC2b1418p was buffered with periclase while other samples were not buffered.

Sample #	T (K)	t (hour)	$logD_{Si}$ (m^2/s)	ϵ (nm)
SC2b1380	1653	96	-20.6	24
SC3b1397	1670	72	-21.0	21
SC2b1418p	1691	60	-20.7	28
SC2b1431	1704	50	-20.9	14
SC2b1450	1723	60	-20.8	9
SC2b1479	1752	50	-20.0	53
SC2b1489	1762	50	-20.2	47

4.5 Discussion

The convolution factor needs to be used in order to obtain true profiles for silicon diffusion. To measure silicon diffusion profiles, one needs to run experiments for relatively long times at fairly high temperature to produce a measurable diffusion length, which should be at least twice value of the convolution factor (*Dohmen et al.*, 2002a). However, values of silicon diffusivity are on the order 10^{-22} m^2/s at 1573 K, such that the diffusion length after 50 hour at this temperature is roughly on the order of several tens of nanometer, which is similar to the length scale of the convolution factor. In addition, a long time anneal at high temperature can also result in evaporation of material

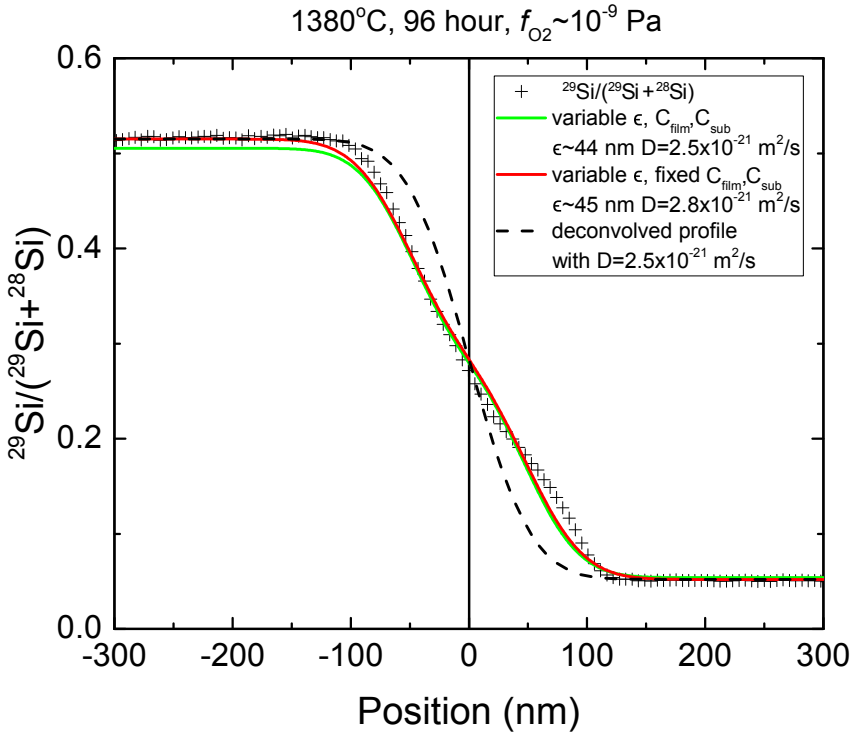

Figure 4.6: Diffusion profiles of Si isotope from sample SC2b1380. Cross symbols are SIMS measurements, green curve is the best fit to the data with C_{film} and C_{sub} as variable, red curve is the best fit to the data with C_{film} and C_{sub} fixed to the averaged values of ^{29}Si concentration in the thin film and substrate, respectively, and the black dashed line is the deconvoluted profile obtained from Equation 4.4.

from the sample surface and result in an increased surface roughness, which in turn causes a larger convolution factor. Thus, it is important to carefully deconvolve the data to obtain best-fit diffusion profiles.

Results for silicon diffusivity from the present study for natural single crystals of San Carlos olivine are similar to those from *Dohmen et al.* (2002a). In addition, our activation energy of ∼560 kJ/mol is the value of 529 kJ/mol reported by *Dohmen et al.* (2002a). The similarity between the

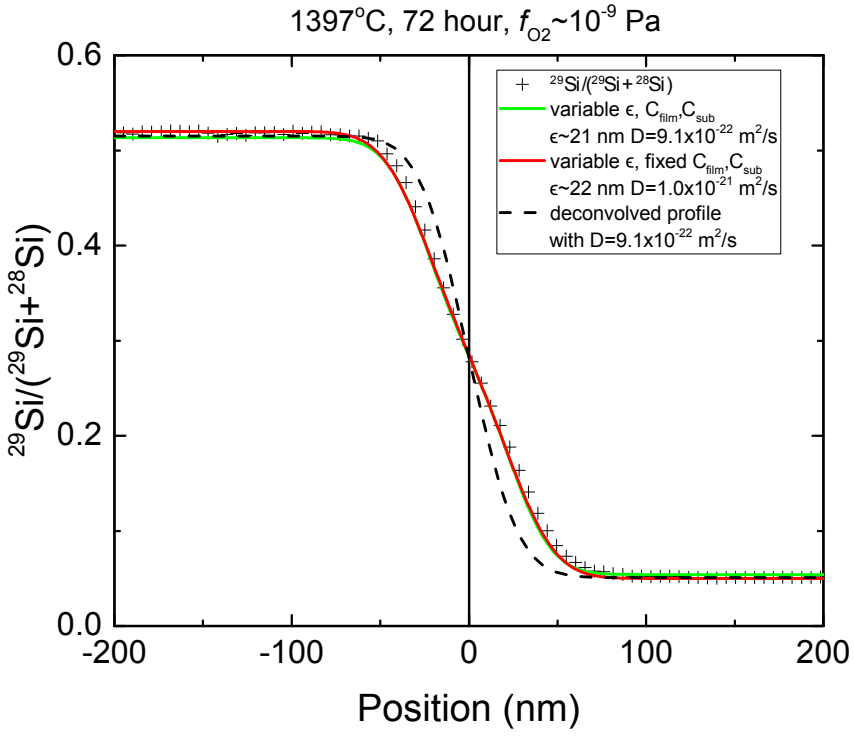

Figure 4.7: Diffusion profiles of Si isotope from sample SC3b1397. Cross symbols are SIMS measurements, green curve is the best fit to the data with C_{film} and C_{sub} as variable, red curve is the best fit to the data with C_{film} and C_{sub} fixed to the averaged values of ^{29}Si concentration in the thin film and substrate, respectively, and the black dashed line is the deconvoluted profile obtained from Equation 4.4.

results for silicon diffusion parallel to [010] from the present study and those parallel to [001] from *Dohmen et al.* (2002a) indicates that there is no significant anisotropy for silicon diffusion in olivine. The good agreement of diffusivity and activation energy between these results also justifies the deconvolution method applied in the present study to obtain deconvolved profiles (Equations 4.3 and 4.4).

As for the discrepancy between these results with those from *Fei et al.* (2012, 2013), different

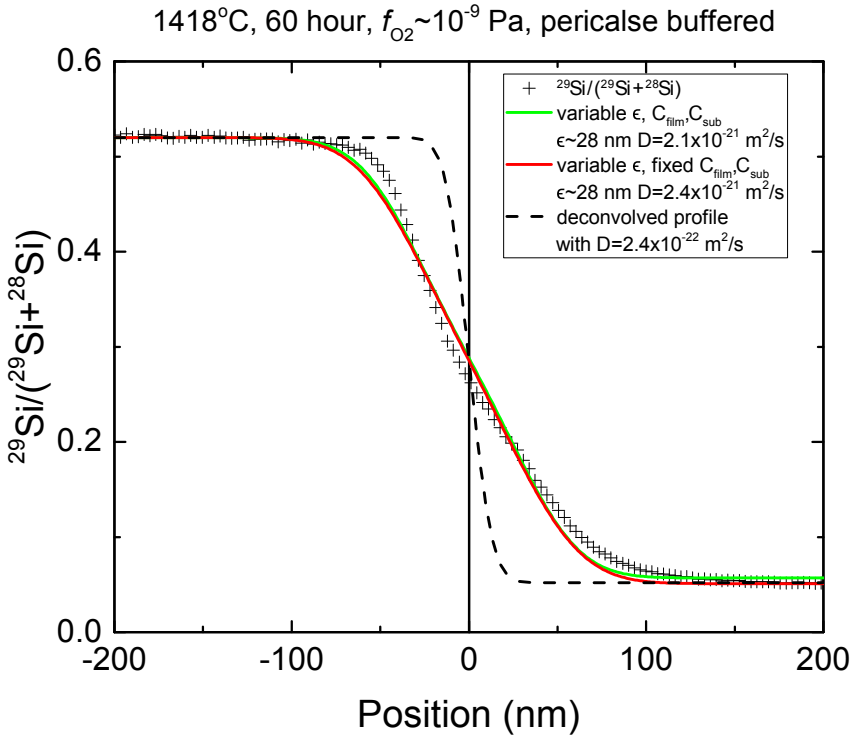

Figure 4.8: Diffusion profiles of Si isotope from sample SC2b1418p. Cross symbols are SIMS measurements, green curve is the best fit to the data with C_{film} and C_{sub} as variable, red curve is the best fit to the data with C_{film} and C_{sub} fixed to the averaged values of ^{29}Si concentration in the thin film and substrate, respectively, and the black dashed line is the deconvoluted profile obtained from Equation 4.4.

sample materials and fitting models for silicon diffusion could account for the different observations. On one hand, they used synthetic iron-free forsterite single crystals. Iron has a significant influence on the physical and chemical properties of olivine as expressed through its point defect chemistry (e.g., *Nakamura and Schmalzried*, 1983) and creep behavior under dry conditions (e.g., *Durham et al.*, 1979; *Kohlstedt and Ricoult*, 1984; *Zhao et al.*, 2009). These effects indicate that

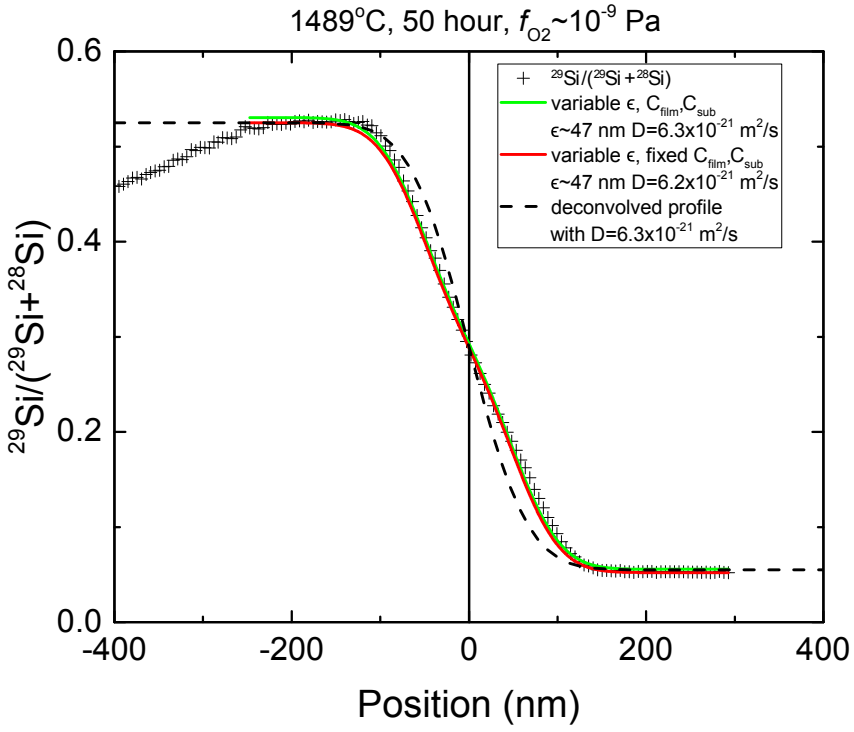

Figure 4.9: Diffusion profiles of Si isotope from sample SC2b1489. Cross symbols are SIMS measurements, green curve is the best fit to the data with C_{film} and C_{sub} as variable, red curve is the best fit to the data with C_{film} and C_{sub} fixed to the averaged values of ^{29}Si concentration in the thin film and substrate, respectively, and the black dashed line is the deconvoluted profile obtained from Equation 4.4.

iron content is important to the concentration of silicon vacancies and consequently to silicon self-diffusivity. On the other hand, *Fei et al.* (2012, 2013) used a different term of nominal diffusion length $L(\sigma)$ in their diffusion model to fit the diffusion profiles. This model may underestimate the convolution effect caused by surface roughness and irregularity at the interface between thin film and substrate. These factors could potentially lead to larger values of silicon diffusivity and a different value for activation energy.

In our study, one sample annealed at 1691 K was buffered with periclase while other samples

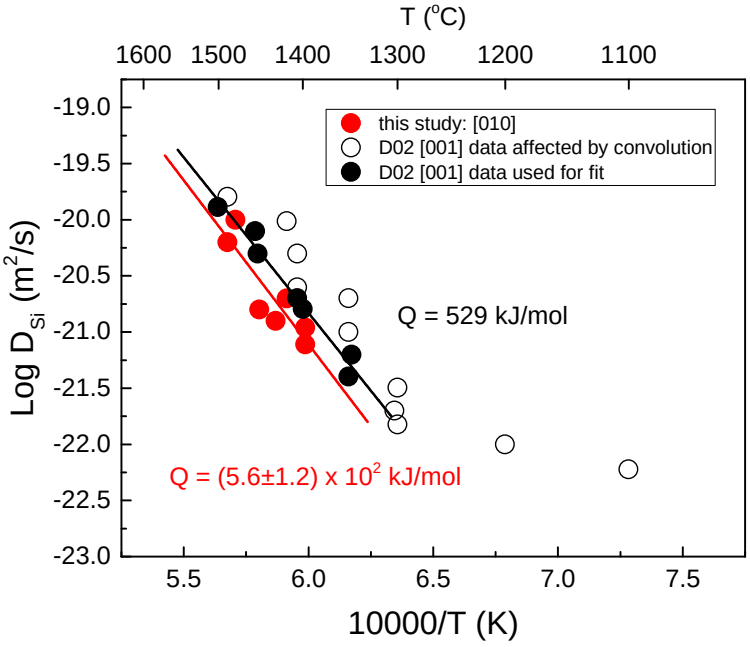

Figure 4.10: Arrhenius plot of silicon diffusivity. Red solid circles are results of silicon diffusivity parallel to [010] with $f_{O_2} = 10^{-9}$ bar from natural single crystals of San Carlos olivine; black solid circles are data from *Dohmen et al.* (2002a) that were not affected by convolution effects and used to obtain the activation anergy of 529 kJ/mol; open circles are data from *Dohmen et al.* (2002a) that were affected by convolution effects with diffusion profile length $< 2\epsilon$.

were not buffered with pyroxene activity. There is no significant difference in the silicon diffusivities from samples annealed at similar temperatures. Thus, no obvious dependence of silicon diffusivity on pyroxene activity is observed.

The concentration of silicon vacancies in olivine should be lower than that of metal vacancies by orders of magnitude. We can calculate the concentration of silicon vacancies, $[\mathrm{V_{Si}}]$, from results for the diffusivity of silicon, D_{Si}, and the diffusivity of silicon vacancies $D_{\mathrm{V_{Si}}}$, from the relationship $D_{\mathrm{Si}} = [\mathrm{V_{Si}}] \times D_{\mathrm{V_{Si}}}$. Under dry condition, with the results of silicon diffusivity from Equation 4.5, we obtain a silicon diffusivity of $\times 10^{-22}$ m^2/s at 1573 K. The diffusivity of silicon

vacancies has a lower limit of $\sim 10^{-12}$ m^2/s at the same temperature, as discussed in Chapter 3. For water saturated conditions with a water fugacity of 1 GPa, silicon diffusivity is $\sim 10^{-19}$ m^2/s (*Costa and Chakraborty*, 2008; *Fei et al.*, 2013); applying the equation for diffusivity of silicon and silicon vacancies, the concentration of silicon vacancies has a upper limit 10^{-7}. Thus, the incorporation mechanism of hydrogen associated with silicon vacancies is not sufficient to present as much hydrogen ions as observed in the results of water solubility of olivine in Chapter 2.

Results of hydroxyl content from hydrogen decoration experiments (*Bai and Kohlstedt*, 1993) agree well with the results of concentration of metal vacancies from thermogravimetric analyses for olivine (*Nakamura and Schmalzried*, 1983; *Tsai and Dieckmann*, 2002) as shown in Figure 4.11. The hydroxyl content obtained from IR peaks of Group I (3650-3450 cm^{-1}), green symbols, and Group II (3450-3200 cm^{-1}), blue symbols, exhibit an oxygen fugacity exponent of $\sim$1/6 (green curve) and $\sim$1/3 (blue curve), respectively. The former value is the same as the dependence of the concentration of metal vacancies on oxygen fugacity for olivine (e.g., *Nakamura and Schmalzried*, 1983). We can calculate the concentration of metal vacancies by assuming that the charge neutrality condition is governed by $2[V''_{Me}] = [(OH)^{\bullet}_{O}]$. Thus, magenta and green dashed curves are the calculated concentration of metal vacancies from the hydroxyl concentration determined from the summation of Group I and Group II peaks and the Group I peaks only, respectively. Black and red dotted curves are concentration of metal vacancies calculated from *Nakamura and Schmalzried* (1983) and *Tsai and Dieckmann* (2002), respectively. Similarity between calculated concentration of metal vacancies from the hydroxyl content (decorated with hydrogen) and the experimental

results of concentration of metal vacancies hence indicates that the dominant incorporation mechanism for hydrogen in olivine is hydrogen associated with metal vacancies.

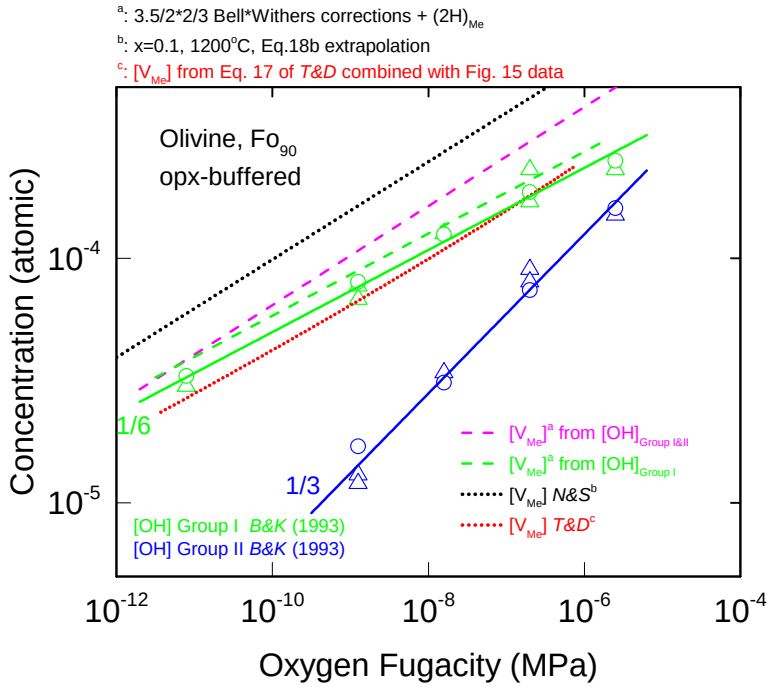

Figure 4.11: Hydroxyl content and concentration of metal vacancies versus oxygen fugacity. Green and blue open symbols are results of hydroxyl content obtained from IR peaks of Group I (3650-3450 cm^{-1}) and Group II (3450-3200 cm^{-1}) from vacancy decoration experiments from *Bai and Kohlstedt* (1993), and solid green and blue curves are linear best-fit to the data points. Green dashed line is calculated concentration of metal vacancies from the hydroxyl content from Group I with corrected calibration factors from *Bell et al.* (2003); *Withers et al.* (2011); magenta dashed curve is calculated concentration of metal vacancies from the hydroxyl content from both Group I and Group II peaks in IR spectra. Black dotted curve represent the concentration of metal vacancies obtained with Equation 18b from *Nakamura and Schmalzried* (1983). Red dotted curve is the concentration of metal vacancies obtained with Equation 17 and data in Figure 15 from*Tsai and Dieckmann* (2002).

4.6 Conclusion

★The convolution effect strongly influences on measured silicon diffusion profiles. Models for fitting silicon diffusivity from measured self-diffusion profiles require the convolution factor to obtain true diffusion profiles and diffusivity.

★Results of silicon diffusion experiments on single crystals of San Carlos olivine ($\sim$ Fo90) parallel to [010] exhibit similar values and activation energy as those from single crystals of Nanga Parbat olivine ($\sim$ Fo93) parallel to [001]. No significant anisotropy is observed for silicon diffusion in olivine.

★No obvious dependence of silicon diffusivity on pyroxene activity is observed.

★The concentration of silicon vacancies is much smaller than that of metal vacancies in olivine, and is insufficient to incorporate as many hydrogen ions as observed in the water solubility studies. Meanwhile, the concentration of metal vacancies obtained with the assumption that hydrogen is associated with metal vacancies agrees with the results of concentration of metal vacancies from thermogravimetric experiments. Thus, hydrogen incorporation mechanism in olivine is dominant by hydrogen associated with metal vacancies.

Chapter 5

Conclusion

5.1 Summary of results

Results of water solubility of olivine single crystal exhibit a positive dependence on pyroxene activity at a pressure of 0.3 GPa. Results from present study and those from earlier studies for the cases of samples buffered with pyroxene yield an exponent of water fugacity close to 1 and an activation volume of $\Delta V_{\mathrm{px}} = (12 \pm 1) \times 10^{-6}\,\mathrm{m}^3/\mathrm{mol}$. These observations all suggest an incorporation mechanism of hydrogen associated with metal vacancies in the case of samples buffered with pyroxene. However, a negative dependence on pyroxene activity was observed at pressures higher than 3 GPa. Results of water solubility at 3, 5 and 8 GPa for samples buffered with periclase from the present and earlier studies yield a water fugacity exponent of $\sim$1.8 and an activation volume of $\Delta V_{\mathrm{pc}} = (25 \pm 8) \times 10^{-6}\,\mathrm{m}^3/\mathrm{mol}$. Thus, a different mechanism for the hydrogen incorporation apply to olivine buffered with periclase.

In Chapter 3, hydrogen species associated with different wavenumbers in IR spectra exhibit the same diffusivity within experimental uncertainty suggesting that hydrogen diffuses through olivine crystal lattice as interstitial protons. Results also illustrate that hydrogen diffusion occurs by two different mechanisms: the faster mechanism is a flux of hydrogen ions with a counter-flux of electron holes; the slower mechanism is a flux of hydrogen ions with a flux of metal vacancies. Results of dehydration experiments exhibit similar anisotropy and diffusivity to that from results of hydration experiments. This important observation indicates that dehydration is the counter process of hydration for olivine. Thus, it is valid to apply hydrogen diffusion results obtained from hydration experiments to the water loss profiles in olivine grains from xenoliths.

Through Chapter 4, we measured silicon diffusivity and estimated the concentration of silicon vacancies in natural single crystals of olivine. No significant anisotropy was observed. Concentration of silicon vacancies is much lower than that of metal vacancies, thus not sufficient to incorporate as many hydrogen ions as observed in the water solubility experiments. In addition, concentration of metal vacancies agree well with the hydroxyl content again indicating that hydrogen dominantly is associated with metal vacancies.

5.2 Future directions

In Chapter 2, it has been noticed that a different mechanism for water solubility in olivine from that for hydrogen associated with metal vacancies becomes dominant for the samples buffered with periclase at high pressures. More results of water solubility in olivine buffered with periclase

are needed to better constrain the water incorporation mechanism at high pressures. A systematic study of the dependence of individual peaks in IR spectra on water fugacity and pyroxene activity may help place constraints on the incorporation mechanisms of the hydroxyl associated with those individual peaks.

Following the work of silicon diffusivity in Chapter 4, future work will be continued on the effect of hydrogen incorporation on silicon diffusivity with elevated water fugacity. *Costa and Chakraborty* (2008) reported results of silicon diffusivity under wet to water-saturated conditions, but unfortunately they did not estimate the influence of convolution effects on the diffusion profiles. In addition, pyroxene activity plays an important role in water solubility of olivine and may also play a key role in silicon diffusivity under wet conditions. However, no experimental results of silicon diffusivity with various pyroxene activity buffers under wet conditions are available yet. Future work may explore the dependence of silicon diffusivity on water fugacity and pyroxene activity together with analyses of water peak in IR spectra.

Retrieving olivine diffusion couple from high-pressure experiment is challenging. However, proper experimental design can help preserve diffusion couple and protect interface in between so that diffusion profile that has a diffusion length shorter than 100 nm can be analyzed. More importantly, convolution effects should be carefully evaluated from silicon diffusion profiles to exclude the artifacts caused by atomic mixing from SIMS measurements and surface roughness of diffusion samples.

References

Aizawa, Y., A. Barnhoorn, U. H. Faul, J. D. F. Gerald, I. Jackson, and I. Kovács (2008), Seismic properties of anita bay dunite: an exploratory study of the influence of water, *Journal of Petrology*, *49*(4), 841–855.

Aubaud, C., A. C. Withers, M. M. Hirschmann, Y. Guan, L. A. Leshin, S. J. Mackwell, and D. R. Bell (2007), Intercalibration of ftir and sims for hydrogen measurements in glasses and nominally anhydrous minerals, *American Mineralogist*, *92*(5-6), 811–828.

Bai, Q. (1992), Substantial hydrogen solubility in olivine and implications for water storage in the mantle, *Nature*, *357*(6380), 672–674.

Bai, Q., and D. Kohlstedt (1993), Effects of chemical environment on the solubility and incorporation mechanism for hydrogen in olivine, *Physics and Chemistry of Minerals*, *19*(7), 460–471.

Bell, D. R., and G. R. Rossman (1992), Water in earth's mantle: the role of nominally anhydrous minerals, *Science*, *255*(5050), 1391.

Bell, D. R., G. R. Rossman, J. Maldener, D. Endisch, and F. Rauch (2003), Hydroxide in olivine: a

quantitative determination of the absolute amount and calibration of the ir spectrum, *Journal of Geophysical Research: Solid Earth (1978–2012)*, *108*(B2).

Bercovici, D., and S.-i. Karato (2003), Whole-mantle convection and the transition-zone water filter, *Nature*, *425*(6953), 39–44.

Berry, A. J., J. Hermann, H. S. O'Neill, and G. J. Foran (2005), Fingerprinting the water site in mantle olivine, *Geology*, *33*(11), 869–872.

Berry, A. J., H. S. C. O'Neill, J. Hermann, and D. R. Scott (2007), The infrared signature of water associated with trivalent cations in olivine, *Earth and Planetary Science Letters*, *261*(1), 134–142.

Blacic, J. D. (1972), Effect of water on the experimental deformation of olivine, *Flow and Fracture of Rocks*, pp. 109–115.

Boioli, F., P. Carrez, P. Cordier, B. Devincre, and M. Marquille (2015), Modeling the creep properties of olivine by 2.5-dimensional dislocation dynamics simulations, *Physical Review B*, *92*(1), 014,115.

Buening, D., and P. R. Buseck (1973), Fe-mg lattice diffusion in olivine, *Journal of Geophysical Research*, *78*(29), 6852–6862.

Cannon, W. R., and T. G. Langdon (1988), Creep of ceramics, *Journal of materials science*, *23*(1), 1–20.

Carslaw, H. S., and J. C. Jaeger (1959), Conduction of heat in solids, *Oxford: Clarendon Press, 1959, 2nd ed.*, *1*, 510.

Carter, N. L., and H. G. Ave'Lallemant (1970), High temperature flow of dunite and peridotite, *Geological Society of America Bulletin*, *81*(8), 2181–2202.

Chakraborty, S. (1997), Rates and mechanisms of fe-mg interdiffusion in olivine at 980–1300 c, *Journal of Geophysical Research: Solid Earth (1978–2012)*, *102*(B6), 12,317–12,331.

Chakraborty, S. (2010), Diffusion coefficients in olivine, wadsleyite and ringwoodite, *Reviews in mineralogy and geochemistry*, *72*(1), 603–639.

Chen, Y., A. Provost, P. Schiano, and N. Cluzel (2011), The rate of water loss from olivine-hosted melt inclusions, *Contributions to Mineralogy and Petrology*, *162*(3), 625–636.

Chen, Y., A. Provost, P. Schiano, and N. Cluzel (2013), Magma ascent rate and initial water concentration inferred from diffusive water loss from olivine-hosted melt inclusions, *Contributions to Mineralogy and Petrology*, *165*(3), 525–541.

Chopra, P., and M. Paterson (1984), The role of water in the deformation of dunite, *Journal of Geophysical Research: Solid Earth (1978–2012)*, *89*(B9), 7861–7876.

Constable, S., and A. Duba (2002), Diffusion and mobility of electrically conducting defects in olivine, *Physics and chemistry of minerals*, *29*(7), 446–454.

Cooper, R., and D. Kohlstedt (1984), Solution-precipitation enhanced diffusional creep of partially molten olivine-basalt aggregates during hot-pressing, *Tectonophysics*, *107*(3), 207–233.

Costa, F., and S. Chakraborty (2008), The effect of water on si and o diffusion rates in olivine and implications for transport properties and processes in the upper mantle, *Physics of the Earth and Planetary Interiors*, *166*(1), 11–29.

Demouchy, S., and S. Mackwell (2003), Water diffusion in synthetic iron-free forsterite, *Physics and Chemistry of Minerals*, *30*(8), 486–494.

Demouchy, S., and S. Mackwell (2006), Mechanisms of hydrogen incorporation and diffusion in iron-bearing olivine, *Physics and Chemistry of Minerals*, *33*(5), 347–355.

Demouchy, S., S. D. Jacobsen, F. Gaillard, and C. R. Stern (2006), Rapid magma ascent recorded by water diffusion profiles in mantle olivine, *Geology*, *34*(6), 429–432.

Denis, C. M., S. Demouchy, and C. S. Shaw (2013), Evidence of dehydration in peridotites from eifel volcanic field and estimates of the rate of magma ascent, *Journal of Volcanology and Geothermal Research*, *258*, 85–99.

Dixon, J. E., T. H. Dixon, D. Bell, and R. Malservisi (2004), Lateral variation in upper mantle viscosity: role of water, *Earth and Planetary Science Letters*, *222*(2), 451–467.

Dohmen, R., and S. Chakraborty (2007), Fe–mg diffusion in olivine ii: point defect chemistry, change of diffusion mechanisms and a model for calculation of diffusion coefficients in natural olivine, *Physics and Chemistry of Minerals*, *34*(6), 409–430.

Dohmen, R., S. Chakraborty, and H.-W. Becker (2002a), Si and o diffusion in olivine and implications for characterizing plastic flow in the mantle, *Geophysical research letters*, *29*(21), 26–1.

Dohmen, R., H.-W. Becker, E. Meißner, T. Etzel, and S. Chakraborty (2002b), Production of silicate thin films using pulsed laser deposition (pld) and applications to studies in mineral kinetics, *European journal of mineralogy*, *14*(6), 1155–1168.

Dohmen, R., H.-W. Becker, and S. Chakraborty (2007), Fe–mg diffusion in olivine i: experimental determination between 700 and 1,200 c as a function of composition, crystal orientation and oxygen fugacity, *Physics and Chemistry of Minerals*, *34*(6), 389–407.

Du Frane, W. L., and J. A. Tyburczy (2012), Deuterium-hydrogen exchange in olivine: Implications for point defects and electrical conductivity, *Geochemistry, Geophysics, Geosystems*, *13*(3).

Du Frane, W. L., J. J. Roberts, D. A. Toffelmier, and J. A. Tyburczy (2005), Anisotropy of electrical conductivity in dry olivine, *Geophysical research letters*, *32*(24).

Durham, W., C. Froidevaux, and O. Jaoul (1979), Transient and steady-state creep of pure forsterite at low stress, *Physics of the Earth and Planetary Interiors*, *19*(3), 263–274.

Evans, B., and D. L. Kohlstedt (1995), Rheology of rocks, *Rock Physics & Phase Relations: A Handbook of Physical Constants*, pp. 148–165.

Fei, H., C. Hegoda, D. Yamazaki, M. Wiedenbeck, H. Yurimoto, S. Shcheka, and T. Katsura (2012), High silicon self-diffusion coefficient in dry forsterite, *Earth and Planetary Science Letters*, *345*, 95–103.

Fei, H., M. Wiedenbeck, D. Yamazaki, and T. Katsura (2013), Small effect of water on upper-mantle rheology based on silicon self-diffusion coefficients, *Nature*, *498*(7453), 213–215.

Gaetani, G. A., J. A. OLeary, K. T. Koga, E. H. Hauri, E. F. Rose-Koga, and B. D. Monteleone (2014), Hydration of mantle olivine under variable water and oxygen fugacity conditions, *Contributions to Mineralogy and Petrology*, *167*(2), 1–14.

Ganguly, J., R. Bhattacharya, and S. Chakraborty (1988), Convolution effect in the determination of compositional profiles and diffusion coefficients by microprobe step scans, *American Mineralogist*, *73*, 901–909.

Gérard, O., and O. Jaoul (1989), Oxygen diffusion in san carlos olivine, *Journal of Geophysical Research: Solid Earth (1978–2012)*, *94*(B4), 4119–4128.

Green, D. H., W. O. Hibberson, I. Kovács, and A. Rosenthal (2010), Water and its influence on the lithosphere-asthenosphere boundary, *Nature*, *467*(7314), 448–451.

Hermeling, J., and H. Schmalzried (1984), Tracerdiffusion of the fe-cations in olivine (fe x mg1-x) 2sio4 (iii), *Physics and Chemistry of Minerals*, *11*(4), 161–166.

Hier-Majumder, S., I. M. Anderson, and D. L. Kohlstedt (2005), Influence of protons on fe-mg interdiffusion in olivine, *Journal of Geophysical Research: Solid Earth (1978–2012)*, *110*(B2).

Hilchie, L., Y. Fedortchouk, S. Matveev, and M. G. Kopylova (2014), The origin of high hydrogen content in kimberlitic olivine: Evidence from hydroxyl zonation in olivine from kimberlites and mantle xenoliths, *Lithos*, *202*, 429–441.

Hirsch, L., T. Shankland, and A. Duba (1993), Electrical conduction and polaron mobility in fe-bearing olivine, *Geophysical Journal International*, *114*(1), 36–44.

Hirschmann, M. M. (2006), Water, melting, and the deep earth h2o cycle, *Annu. Rev. Earth Planet. Sci.*, *34*, 629–653.

Hirth, G., and D. Kohlstedt (2003), Rheology of the upper mantle and the mantle wedge: A view from the experimentalists, *Inside the subduction Factory*, pp. 83–105.

Hirth, G., and D. L. Kohlstedt (1995), Experimental constraints on the dynamics of the partially molten upper mantle: Deformation in the diffusion creep regime, *Journal of Geophysical Research: Solid Earth (1978–2012)*, *100*(B2), 1981–2001.

Hirth, G., and D. L. Kohlstedt (1996), Water in the oceanic upper mantle: implications for rheology, melt extraction and the evolution of the lithosphere, *Earth and Planetary Science Letters*, *144*(1), 93–108.

Hobbs, B. (1983), Constraints on the mechanism of deformation of olivine imposed by defect chemistry, *Tectonophysics*, *92*(1), 35–69.

Hofmann, S. (1994), Atomic mixing, surface roughness and information depth in high-resolution aes depth profiling of a gaas/alas superlattice structure, *Surface and interface analysis*, *21*(9), 673–678.

Houlier, B., M. Cheraghmakani, and O. Jaoul (1990), Silicon diffusion in san carlos olivine, *Physics of the Earth and Planetary Interiors*, *62*(3), 329–340.

Ingrin, J., and H. Skogby (2000), Hydrogen in nominally anhydrous upper-mantle minerals concentration levels and implications, *European Journal of Mineralogy*, *12*(3), 543–570.

Jackson, I. (2000), *The Earth's mantle: composition, structure, and evolution*, Cambridge University Press.

Jacobsen, S. D., F. Jiang, Z. Mao, T. S. Duffy, J. R. Smyth, C. M. Holl, and D. J. Frost (2008), Effects of hydration on the elastic properties of olivine, *Geophysical Research Letters*, *35*(14).

Karato, S., and H. Spetzler (1990), Defect microdynamics in minerals and solid-state mechanisms of seismic wave attenuation, *Reviews of Geophysics*, *28*, 399–421.

Karato, S.-I. (1990), The role of hydrogen in the electrical conductivity of the upper mantle, *Nature*.

Karato, S.-i. (1995), Effects of water on seismic wave velocities in the upper mantle., *Proceedings of the Japan Academy, Series B*, *71*(2), 61–66.

Karato, S.-i. (2003), Mapping water content in upper mantle, *GEOPHYSICAL MONOGRAPH-AMERICAN GEOPHYSICAL UNION*, *138*, 135–152.

Karato, S.-i. (2006), Influence of hydrogen-related defects on the electrical conductivity and plastic deformation of mantle minerals: a critical review, *GEOPHYSICAL MONOGRAPH-AMERICAN GEOPHYSICAL UNION*, *168*, 113.

Karato, S.-i. (2008), *Deformation of earth materials: an introduction to the rheology of solid earth*, Cambridge University Press.

Karato, S.-i. (2010), Rheology of the deep upper mantle and its implications for the preservation of the continental roots: A review, *Tectonophysics*, *481*(1), 82–98.

Karato, S.-i. (2011), Water distribution across the mantle transition zone and its implications for global material circulation, *Earth and Planetary Science Letters*, *301*(3), 413–423.

Karato, S.-i., and H. Jung (1998), Water, partial melting and the origin of the seismic low velocity and high attenuation zone in the upper mantle, *Earth and Planetary Science Letters*, *157*(3), 193–207.

Karato, S.-I., and H. Jung (2003), Effects of pressure on high-temperature dislocation creep in olivine, *Philosophical Magazine*, *83*(3), 401–414.

Karato, S.-I., M. S. Paterson, and J. D. FitzGerald (1986), Rheology of synthetic olivine aggregates: influence of grain size and water, *Journal of Geophysical Research: Solid Earth (1978–2012)*, *91*(B8), 8151–8176.

Kohlstedt, D., and L. Hansen (2015), 2.18 - constitutive equations, rheological behavior, and viscosity of rocks, in *Treatise on Geophysics (Second Edition)*, edited by G. Schubert, second edition ed., pp. 441 – 472, Elsevier, Oxford, doi:http://dx.doi.org/10.1016/B978-0-444-53802-4.00042-7.

Kohlstedt, D., and D. Ricoult (1984), High-temperature creep of silicate olivines, in *Deformation of Ceramic Materials II*, pp. 251–280, Springer.

Kohlstedt, D., H. Keppler, and D. Rubie (1996), Solubility of water in the α, β and γ phases of (mg, fe) 2sio4, *Contributions to Mineralogy and Petrology*, *123*(4), 345–357.

Kohlstedt, D. L. (2006), The role of water in high-temperature rock deformation, *Reviews in mineralogy and geochemistry*, *62*(1), 377–396.

Kohlstedt, D. L., and S. J. Mackwell (1998), Diffusion of hydrogen and intrinsic point defects in olivine, *Zeitschrift für physikalische Chemie*, *207*(Part_1_2), 147–162.

Kovács, I., H. S. C. ONeill, J. Hermann, and H. Hauri (2010), Site-specific infrared oh absorption coefficients for water substitution into olivine, *American Mineralogist*, *95*(2-3), 292–299.

Kröger, F., and H. Vink (1956), Relations between the concentrations of imperfections in crystalline solids, *Solid state physics*, *3*, 307–435.

Lemaire, C., S. Kohn, and R. Brooker (2004), The effect of silica activity on the incorporation mechanisms of water in synthetic forsterite: a polarised infrared spectroscopic study, *Contributions to Mineralogy and Petrology*, *147*(1), 48–57.

Lovering, T. (1936), Heat conduction in dissimilar rocks and the use of thermal models, *Geological Society of America Bulletin*, *47*(1), 87–100.

Mackwell, S., D. Kohlstedt, and M. Paterson (1985), The role of water in the deformation of olivine single crystals, *Journal of Geophysical Research: Solid Earth (1978–2012)*, *90*(B13), 11,319–11,333.

Mackwell, S., D. Dimos, and D. Kohlstedt (1988), Transient creep of olivine: point-defect relaxation times, *Philosophical Magazine A*, *57*(5), 779–789.

Mackwell, S. J., and D. L. Kohlstedt (1990), Diffusion of hydrogen in olivine: implications for water in the mantle, *Journal of Geophysical Research: Solid Earth (1978–2012)*, *95*(B4), 5079–5088.

Matveev, S., H. S. C. Oneill, C. Ballhaus, W. Taylor, and D. Green (2001), Effect of silica activity on oh- ir spectra of olivine: implications for low-asio2 mantle metasomatism, *Journal of Petrology*, *42*(4), 721–729.

Mei, S., and D. Kohlstedt (2000a), Influence of water on plastic deformation of olivine aggregates: 1. diffusion creep regime, *Journal of Geophysical Research: Solid Earth (1978–2012)*, *105*(B9), 21,457–21,469.

Mei, S., and D. Kohlstedt (2000b), Influence of water on plastic deformation of olivine aggregates: 2. dislocation creep regime, *Journal of Geophysical Research: Solid Earth (1978–2012)*, *105*(B9), 21,471–21,481.

Miller, G. H., G. R. Rossman, and G. E. Harlow (1987), The natural occurrence of hydroxide in olivine, *Physics and Chemistry of Minerals*, *14*(5), 461–472.

Misener, D. J. (1973), Cation diffusion in olivine to 1400 c and 35 kb.

Mosenfelder, J. L., N. I. Deligne, P. D. Asimow, and G. R. Rossman (2006), Hydrogen incorporation in olivine from 2–12 gpa, *American Mineralogist*, *91*(2-3), 285–294.

Nakamura, A., and H. Schmalzried (1983), On the nonstoichiometry and point defects of olivine, *Physics and Chemistry of Minerals*, *10*(1), 27–37.

Nakamura, A., and H. Schmalzried (1984), On the fe2+–mg2+-interdiffusion in olivine (ii), *Berichte der Bunsengesellschaft für physikalische Chemie*, *88*(2), 140–145.

Ohtani, E., K. Litasov, T. Hosoya, T. Kubo, and T. Kondo (2004), Water transport into the deep mantle and formation of a hydrous transition zone, *Physics of the Earth and Planetary Interiors*, *143*, 255–269.

Padrón-Navarta, J. A., J. Hermann, and H. S. C. O'Neill (2014), Site-specific hydrogen diffusion rates in forsterite, *Earth and Planetary Science Letters*, *392*, 100–112.

Paterson, M. (1982), The determination of hydroxyl by infrared absorption in quartz, silicate glasses, and similar materials, *Bulletin de la Societe Francaise de Mineralogie*, *105*, 20–29.

Paterson, M. (1990), Rock deformation experimentation, *The Brittle-Ductile Transition in Rocks, Geophys. Monogr. Ser*, *56*, 187–194.

Peslier, A. H. (2010), A review of water contents of nominally anhydrous natural minerals in the mantles of earth, mars and the moon, *Journal of Volcanology and Geothermal Research*, *197*(1), 239–258.

Peslier, A. H., and J. F. Luhr (2006), Hydrogen loss from olivines in mantle xenoliths from simcoe (usa) and mexico: mafic alkalic magma ascent rates and water budget of the sub-continental lithosphere, *Earth and Planetary Science Letters*, *242*(3), 302–319.

Peslier, A. H., A. B. Woodland, and J. A. Wolff (2008), Fast kimberlite ascent rates estimated from hydrogen diffusion profiles in xenolithic mantle olivines from southern africa, *Geochimica et Cosmochimica Acta*, *72*(11), 2711–2722.

Peslier, A. H., M. Bizimis, and M. Matney (2015), Water disequilibrium in olivines from hawaiian peridotites: Recent metasomatism, h diffusion and magma ascent rates, *Geochimica et Cosmochimica Acta*, *154*, 98–117.

Pitzer, K. S., and S. M. Sterner (1994), Equations of state valid continuously from zero to extreme pressures for h2o and co2, *The Journal of chemical physics*, *101*(4), 3111–3116.

Poe, B. T., C. Romano, F. Nestola, and J. R. Smyth (2010), Electrical conductivity anisotropy of dry and hydrous olivine at 8gpa, *Physics of the Earth and Planetary Interiors*, *181*(3), 103–111.

Poirier, J. (1995), Plastic rheology of crystals, *Mineral physics and crystallography. A handbook of physical constants*.

Poirier, J.-P. (1985), *Creep of crystals: high-temperature deformation processes in metals, ceramics and minerals*, Cambridge University Press.

Poumellec, B., and O. Jaoul (1984), Influence of po2 and ph2o on the high temperature plasticity of olivine, in *Deformation of Ceramic Materials II*, pp. 281–305, Springer.

Robie, R. A., B. Hemmingway, and J. R. Fisher (1978), Thermodynamic properties of minerals and related substances at 298.15 k and 1 bar pressure and at higher temperature, *Geol. Surv. Bull., vol., p. 1452-1452 (1978).*, *1*, 1452–1452.

Ryerson, F. J., and W. B. Durham (1989), Oxygen diffusion in olivine: The effect of oxygen fugacity and implications for creep, *Earth Sciences*, p. 103.

Sato, H. (1986), High temperature ac electrical properties of olivine single crystal with varying oxygen partial pressure: implications for the point defect chemistry, *Physics of the earth and planetary interiors*, *41*(4), 269–282.

Shaw, H. R., and D. R. Wones (1964), Fugacity coefficients for hydrogen gas between o degrees and 1000 degrees c, for pressures to 3000 atm, *American Journal of Science*, *262*(7), 918–929.

Simpson, F., and A. Tommasi (2005), Hydrogen diffusivity and electrical anisotropy of a peridotite mantle, *Geophysical Journal International*, *160*(3), 1092–1102.

Smyth, J., D. Frost, F. Nestola, C. Holl, and G. Bromiley (2006), Olivine hydration in the deep upper mantle: effects of temperature and silica activity, *Geophysical Research Letters*, *33*(15).

Smyth, J. R., and D. J. Frost (2002), The effect of water on the 410-km discontinuity: An experimental study, *Geophysical Research Letters*, *29*(10), 123–1.

Tödheide, K. (1972), Water at high temperatures and pressures, in *The Physics and Physical Chemistry of Water*, pp. 463–514, Springer.

Tsai, T.-L., and R. Dieckmann (1997), Point defects and transport of matter and charge in olivines,(fexmg1-x) 2sio4, in *Materials Science Forum*, vol. 239, pp. 399–402, Trans Tech Publ.

Tsai, T.-L., and R. Dieckmann (2002), Variation of the oxygen content and point defects in olivines,(fe x mg 1- x) 2sio4, 0.2 x 1.0, *Physics and chemistry of minerals*, *29*(10), 680–694.

Walker, A., J. Hermann, A. Berry, and H. S. C. O'Neill (2007), Three water sites in upper mantle olivine and the role of titanium in the water weakening mechanism, *Journal of Geophysical Research: Solid Earth (1978–2012)*, *112*(B5).

Wanamaker, B. (1994), Point defect diffusivites in san carlos olivine derived from reequilibration of electrical conductivity following changes in oxygen fugacity, *Geophysical research letters*, *21*(1), 21–24.

Wang, D., M. Mookherjee, Y. Xu, and S.-i. Karato (2006), The effect of water on the electrical conductivity of olivine, *Nature*, *443*(7114), 977–980.

Wang, D., S.-i. Karato, and Z. Liu (2012), Influence of hydrogen on the electronic states of olivine: Implications for electrical conductivity, *Geophysical Research Letters*, *39*(6).

Wang, Z., T. Hiraga, and D. Kohlstedt (2004), Effect of h+ on fe–mg interdiffusion in olivine,(fe, mg) 2sio4, *Applied physics letters*, *85*(2), 209–211.

Weertman, J. (1955), Theory of steady-state creep based on dislocation climb, *Journal of Applied Physics*, *26*(10), 1213–1217.

Weertman, J. (1957), Steady-state creep through dislocation climb, *Journal of Applied Physics*, *28*, 362–364.

Weertman, J. (1999), Microstructural mechanisms of creep, *Mechanics and materials: Fundamentals and linkages*, pp. 451–488.

Weertman, J., S. White, and A. H. Cook (1978), Creep laws for the mantle of the earth [and discussion], *Philosophical Transactions of the Royal Society of London A: Mathematical, Physical and Engineering Sciences*, *288*(1350), 9–26.

Withers, A., M. Hirschmann, and T. Tenner (2011), The effect of fe on olivine h2o storage capacity: Consequences for h2o in the martian mantle, *American Mineralogist*, *96*(7), 1039–1053.

Withers, A. C., and M. M. Hirschmann (2008), Influence of temperature, composition, silica activity and oxygen fugacity on the h2o storage capacity of olivine at 8 gpa, *Contributions to Mineralogy and Petrology*, *156*(5), 595–605.

Yoshino, T., T. Matsuzaki, S. Yamashita, and T. Katsura (2006), Hydrous olivine unable to account for conductivity anomaly at the top of the asthenosphere, *Nature*, *443*(7114), 973–976.

Yoshino, T., T. Matsuzaki, A. Shatskiy, and T. Katsura (2009), The effect of water on the electrical conductivity of olivine aggregates and its implications for the electrical structure of the upper mantle, *Earth and Planetary Science Letters*, *288*(1), 291–300.

Zhao, Y.-H., S. Ginsberg, and D. Kohlstedt (2004), Solubility of hydrogen in olivine: dependence on temperature and iron content, *Contributions to Mineralogy and Petrology*, *147*(2), 155–161.

Zhao, Y.-H., M. E. Zimmerman, and D. L. Kohlstedt (2009), Effect of iron content on the creep

behavior of olivine: 1. anhydrous conditions, *Earth and Planetary Science Letters*, *287*(1), 229–240.

Appendix A

IR spectra for water solubility

A.1 IR spectra from samples hydrothermally annealed at 0.3, 3, and 5 GPa

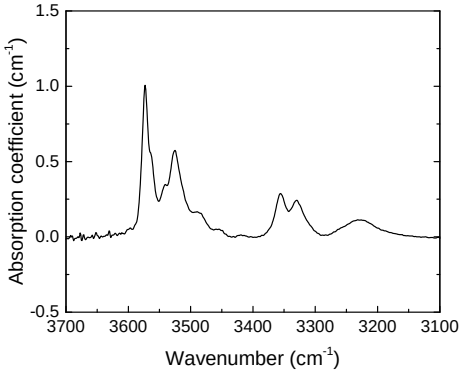

Figure A.1: Unpolarized FTIR spectra from sample PI-1676a hydrothermally annealed at 0.3 GPa, 1473 K and buffered by pyroxene. Oxygen fugacity was buffered with Ni/NiO.

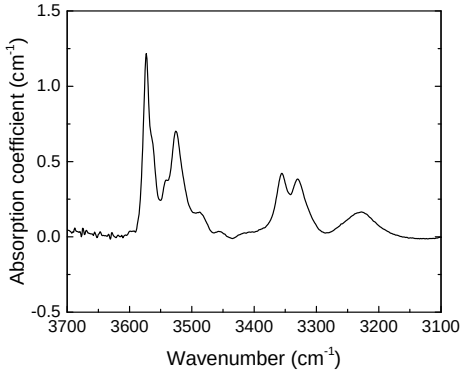

Figure A.2: Unpolarized FTIR spectra from sample PI-1676 hydrothermally annealed at 0.3 GPa, 1473 K and buffered by pyroxene. Oxygen fugacity was buffered with Ni/NiO.

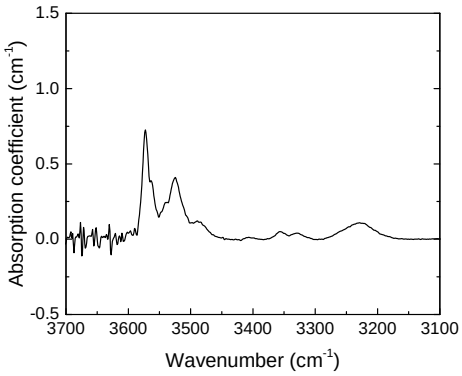

Figure A.3: Unpolarized FTIR spectra from sample PI-1674a hydrothermally annealed at 0.3 GPa, 1473 K and buffered by periclase. Oxygen fugacity was buffered with Ni/NiO.

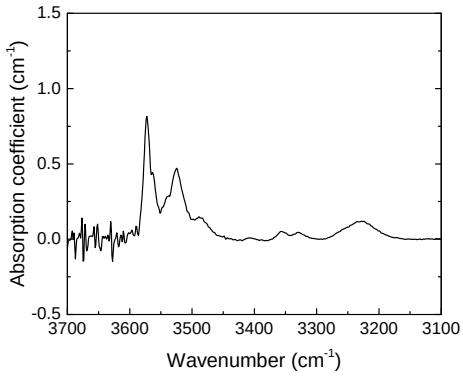

Figure A.4: Unpolarized FTIR spectra from sample PI-1674 hydrothermally annealed at 0.3 GPa, 1473 K and buffered by periclase. Oxygen fugacity was buffered with Ni/NiO.

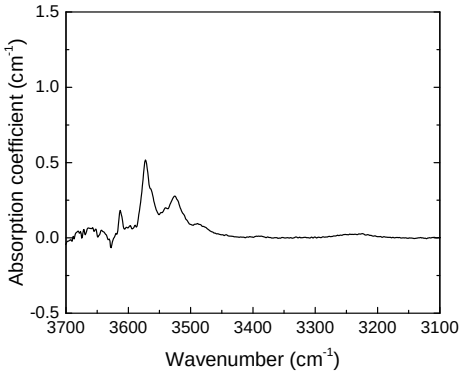

Figure A.5: Unpolarized FTIR spectra from sample PI-1680a hydrothermally annealed at 0.3 GPa, 1473 K and buffered by pyroxene. Oxygen fugacity was buffered with Fe/FeO.

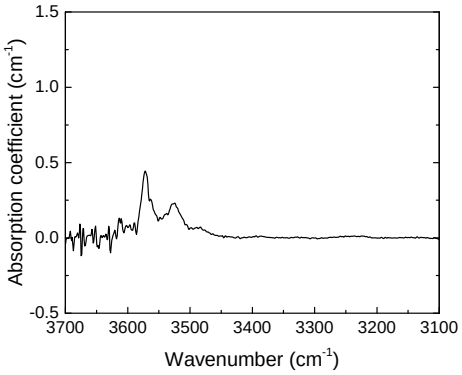

Figure A.6: Unpolarized FTIR spectra from sample PI-1680 hydrothermally annealed at 0.3 GPa, 1473 K and buffered by pyroxene. Oxygen fugacity was buffered with Fe/FeO.

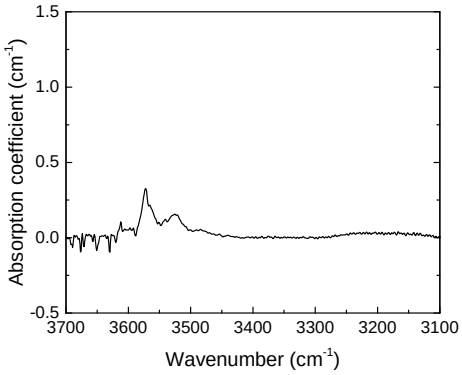

Figure A.7: Unpolarized FTIR spectra from sample PI-1691a hydrothermally annealed at 0.3 GPa, 1473 K and buffered by periclase. Oxygen fugacity was buffered with Fe/FeO.

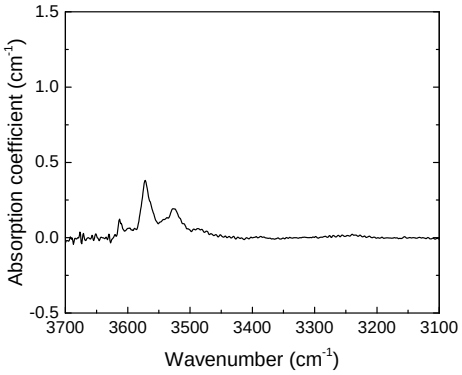

Figure A.8: Unpolarized FTIR spectra from sample PI-1691 hydrothermally annealed at 0.3 GPa, 1473 K and buffered by periclase. Oxygen fugacity was buffered with Fe/FeO.

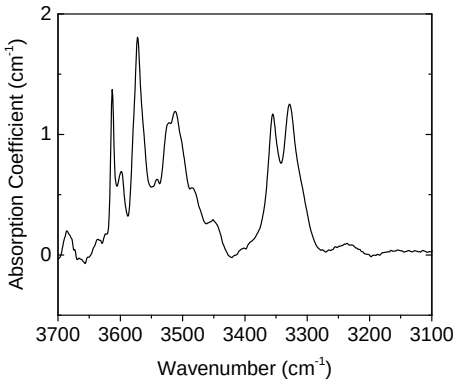

Figure A.9: Unpolarized FTIR spectra from sample M666 hydrothermally annealed at 3 G-Pa, 1473 K and buffered by pyroxene. Oxygen fugacity was buffered with Ni/NiO.

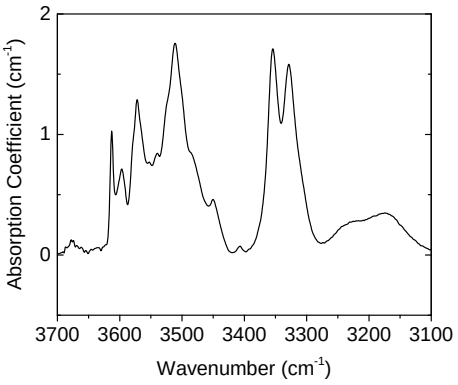

Figure A.10: Unpolarized FTIR spectra from sample M708 hydrothermally annealed at 3 G-Pa, 1473 K and buffered by pyroxene. Oxygen fugacity was buffered with Ni/NiO.

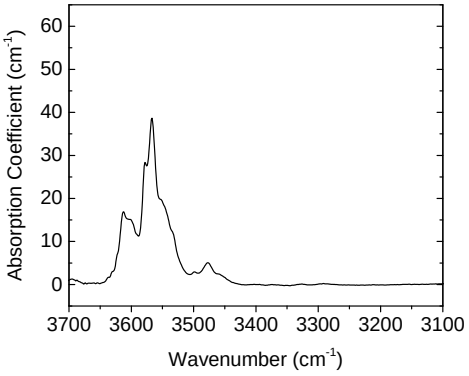

Figure A.11: Unpolarized FTIR spectra from sample M709 hydrothermally annealed at 3 G-Pa, 1473 K and buffered by periclase. Oxygen fugacity was buffered with Ni/NiO.

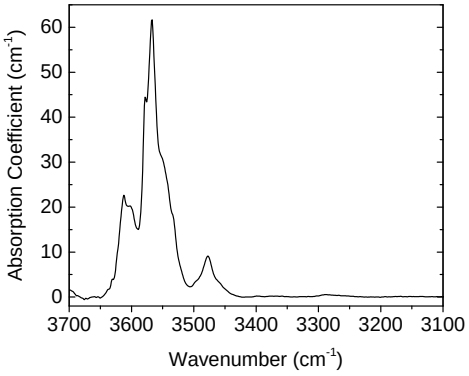

Figure A.12: Unpolarized FTIR spectra from sample M712 hydrothermally annealed at 3 G-Pa, 1473 K and buffered by periclase. Oxygen fugacity was buffered with Ni/NiO.

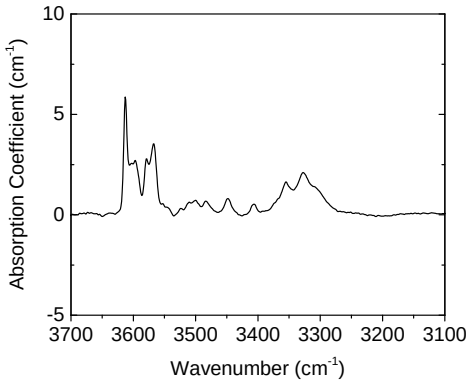

Figure A.13: Unpolarized FTIR spectra from sample M670 hydrothermally annealed at 5 G-Pa, 1473 K and buffered by pyroxene. Oxygen fugacity was buffered with Ni/NiO.

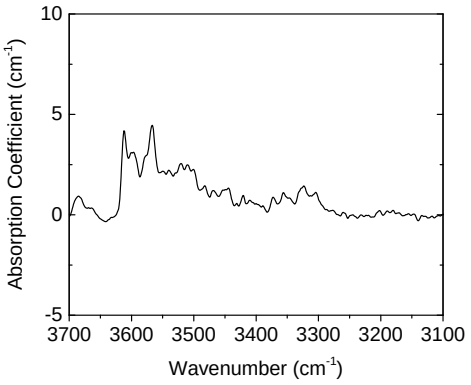

Figure A.14: Unpolarized FTIR spectra from sample M682 hydrothermally annealed at 5 G-Pa, 1473 K and buffered by pyroxene. Oxygen fugacity was buffered with Ni/NiO.

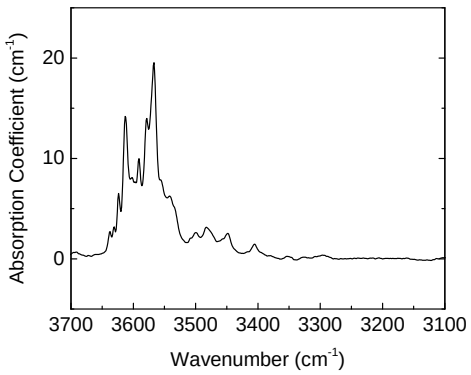

Figure A.15: Unpolarized FTIR spectra from sample M709 hydrothermally annealed at 5 G-Pa, 1473 K and buffered by periclase. Oxygen fugacity was buffered with Ni/NiO.

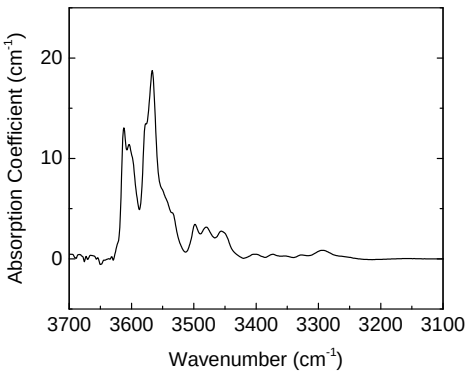

Figure A.16: Unpolarized FTIR spectra from sample M650 hydrothermally annealed at 5 G-Pa, 1473 K and buffered by periclase. Oxygen fugacity was buffered with Ni/NiO.

Appendix B

Diffusion profiles of hydrous defect

B.1 Series of IR spectra of diffusion samples

Figure B.1.1: Series of polarized (E//a) IR spectra from sample SC14_6 hydrothermally annealed at 1173 K and 300 MPa for 1 hour with oxygen fugacity buffered by Fe/FeO. The numbers on the left are the distance from the edge along each principal direction on the sample:(a) parallel to [100], (b) parallel to [010], (c) parallel to [001].

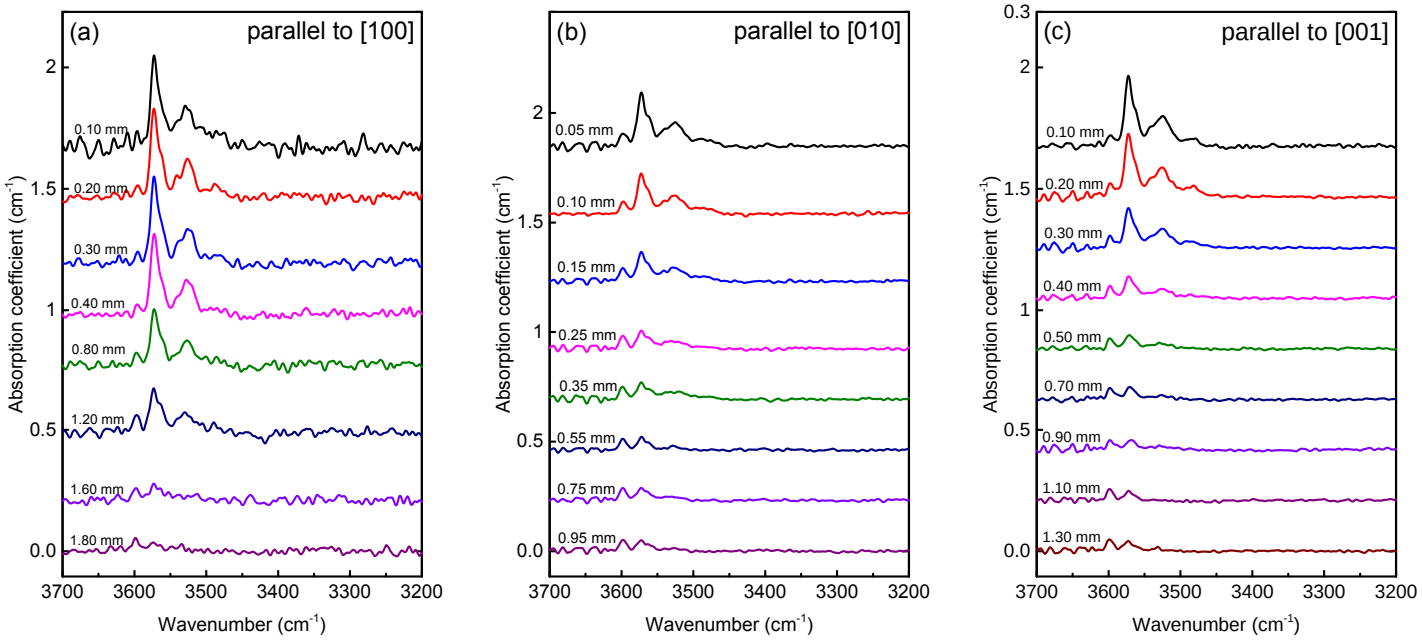

Figure B.1.2: Series of polarized (E//a) IR spectra from sample SC16_6 hydrothermally annealed at 1273 K and 300 MPa for 35 min with oxygen fugacity buffered by Ni/NiO. The numbers on the left are the distance from the edge along each principal direction on the sample:(a) parallel to [100], (b) parallel to [010], (c) parallel to [001].

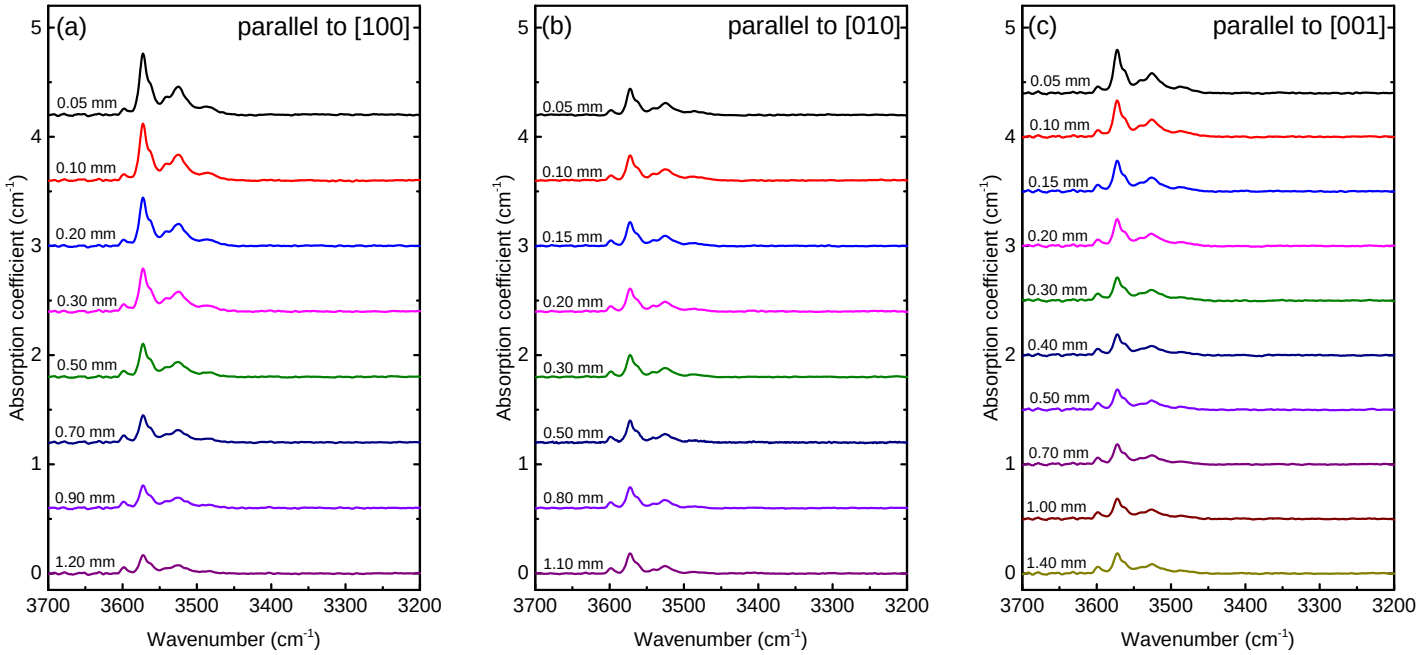

Figure B.1.3: Series of polarized (E//a) IR spectra from sample SC31_2 hydrothermally annealed at 1173 K and 200 MPa for 21 h 6 min with oxygen fugacity buffered by Ni/NiO. The numbers on the left are the distance from the edge along each principal direction on the sample:(a) parallel to [100], (b) parallel to [010], (c) parallel to [001].

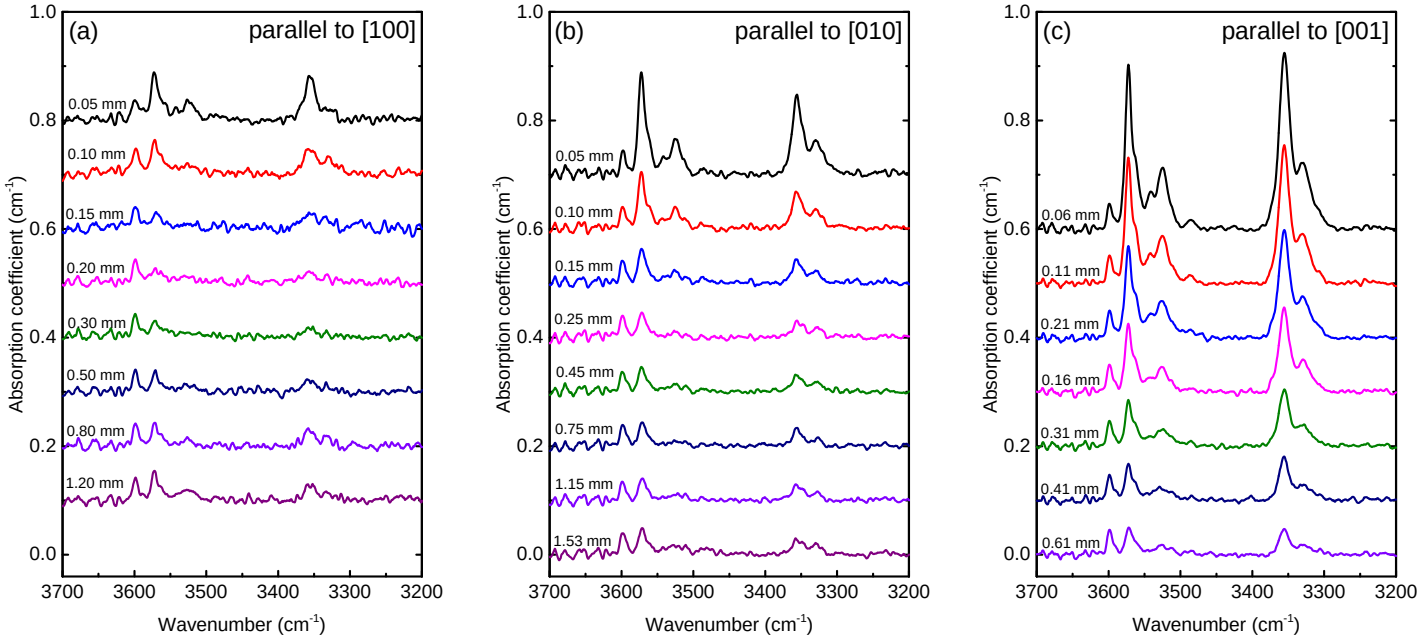

Figure B.1.4: Series of polarized (E//a) IR spectra from sample SC31_3 hydrothermally annealed at 1273 K and 200 MPa for 8 h with oxygen fugacity buffered by Ni/NiO. The numbers on the left are the distance from the edge along each principal direction on the sample:(a) parallel to [100], (b) parallel to [010], (c) parallel to [001].

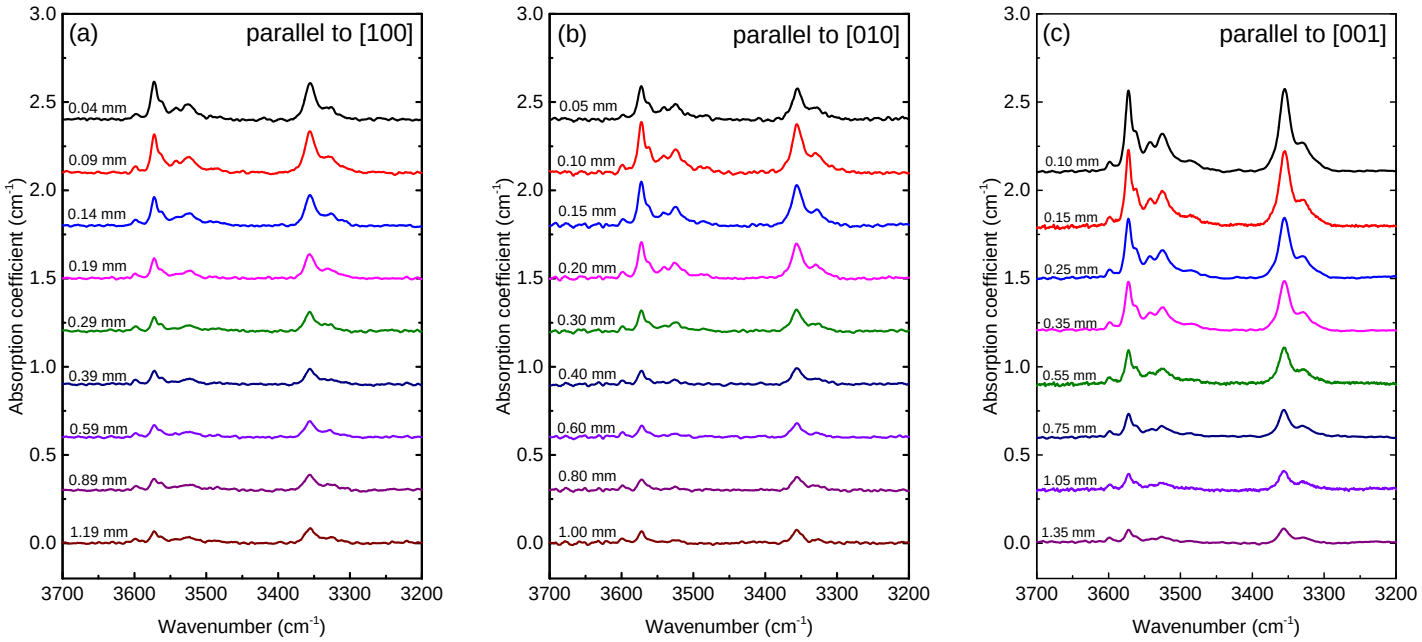

Figure B.1.5: Series of polarized (E//a) IR spectra from sample SC31_5 hydrothermally annealed at 1303 K and 200 MPa for 5h with oxygen fugacity buffered by Ni/NiO. The numbers on the left are the distance from the edge along each principal direction on the sample:(a) parallel to [100], (b) parallel to [001].

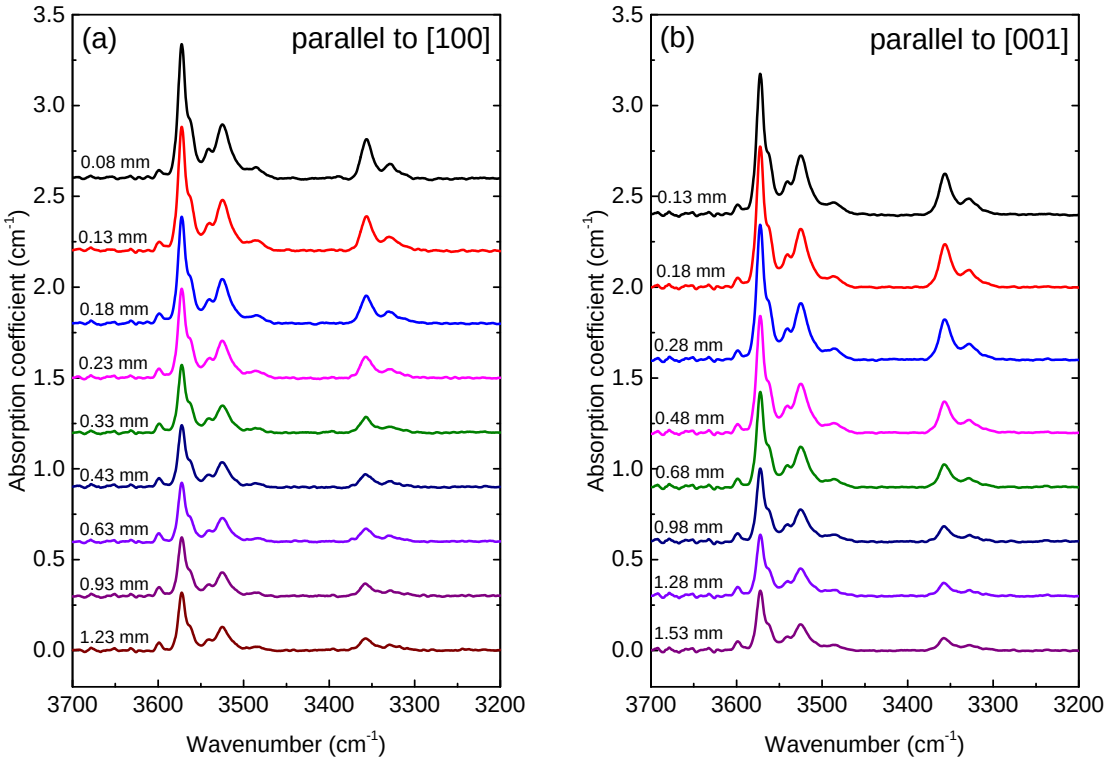

Figure B.1.6: Series of unpolarized IR spectra from sample PI-1914 dehydrated at 1253 K and 1 atmosphere for 5 hour with oxygen fugacity of 10^{-11} Pa. The numbers on the left are the distance from the edge along each principal direction on the sample:(a) parallel to [100], (b) parallel to [001].

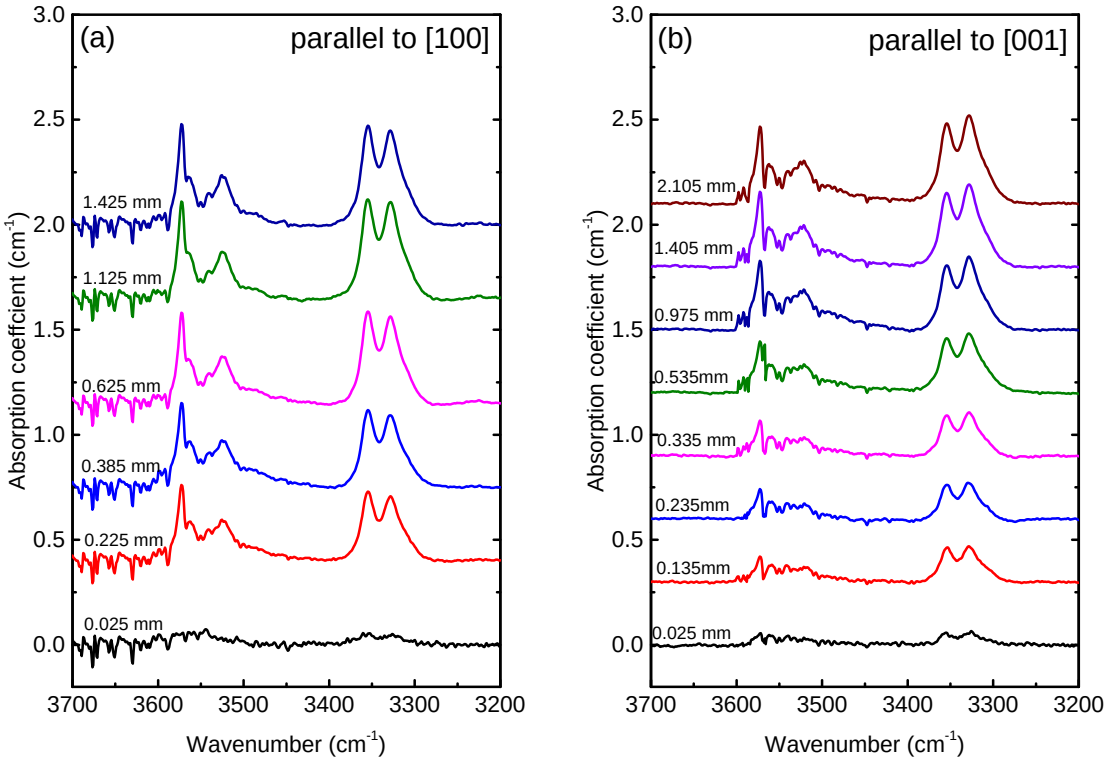

Figure B.1.7: Series of unpolarized IR spectra from sample PI-1918-1 dehydrated at 1322 K and 1 atmosphere for 3 hour with an oxygen fugacity of 10^{-11} Pa. The numbers on the left are the distance from the edge along each principal direction on the sample:(a) parallel to [100], (b) parallel to [001].

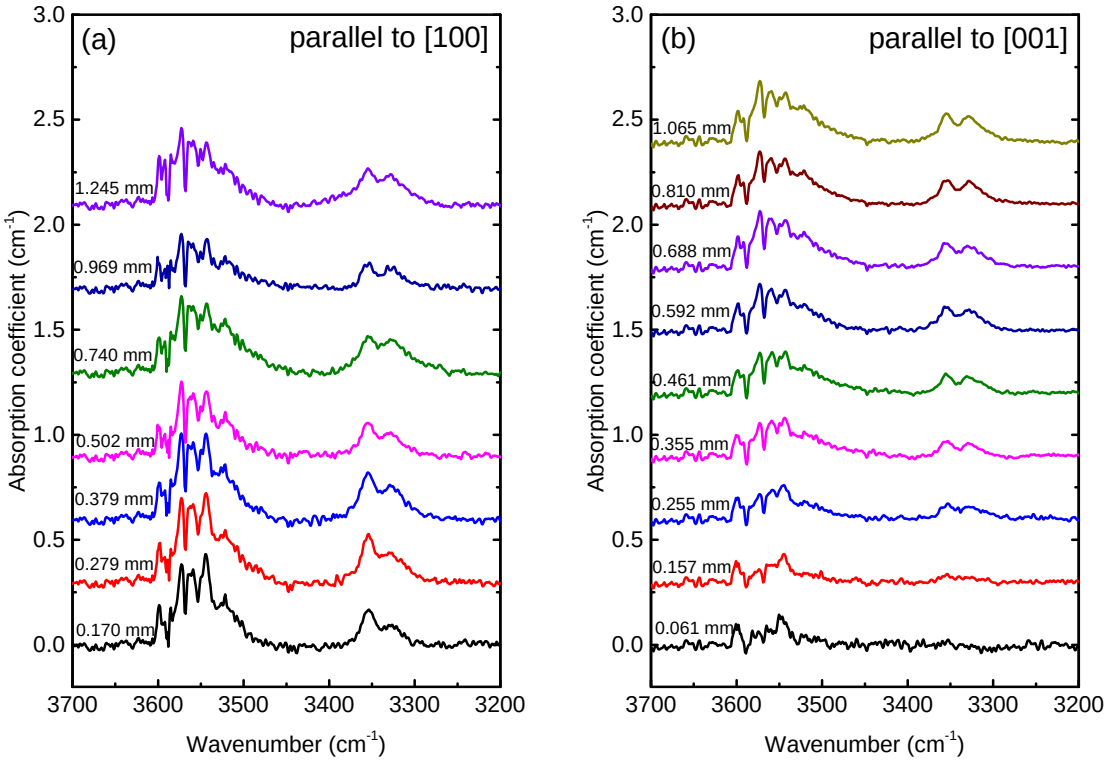

Figure B.1.8: Series of unpolarized IR spectra from sample PI-1918-2 dehydrated at 1358 K and 1 atmosphere for 2 hour with an oxygen fugacity of 10^{-11} Pa. The numbers on the left are the distance from the edge along each principal direction on the sample:(a) parallel to [100], (b) parallel to [001].

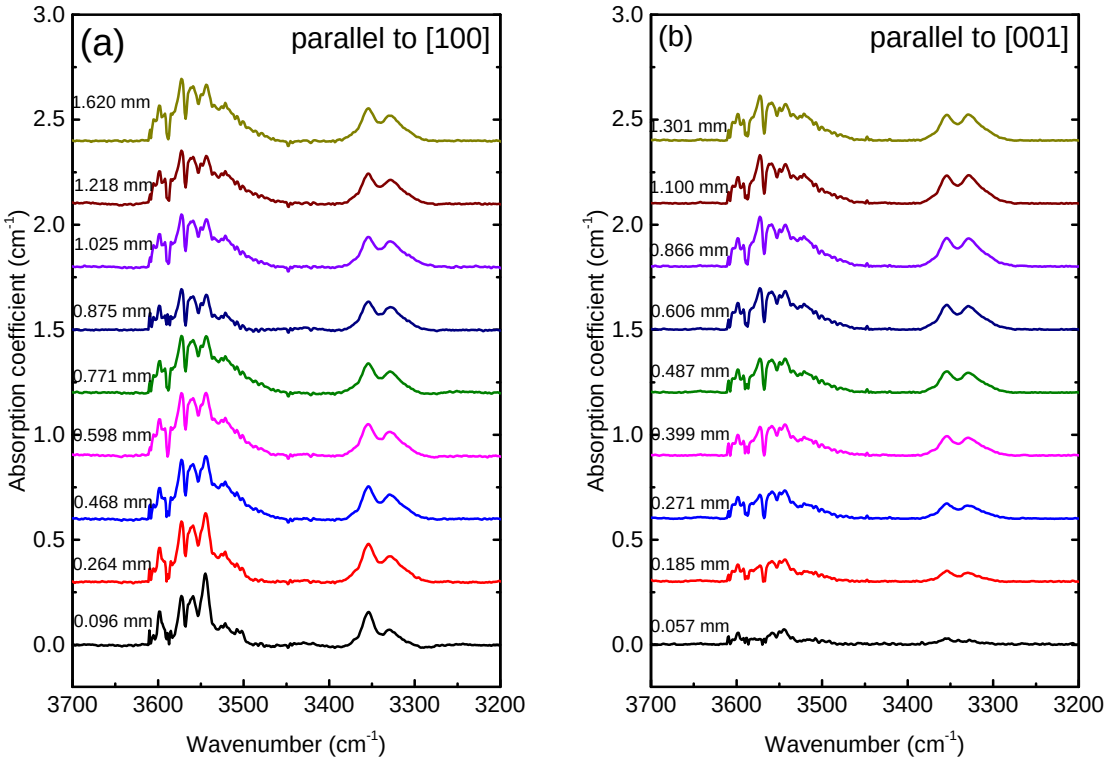

Figure B.1.9: Series of unpolarized IR spectra from sample PI-1918-3 dehydrated at 1191 K and 1 atmosphere for 20 hour with an oxygen fugacity of 10^{-11} Pa. The numbers on the left are the distance from the edge along each principal direction on the sample:(a) parallel to [100], (b) parallel to [001].

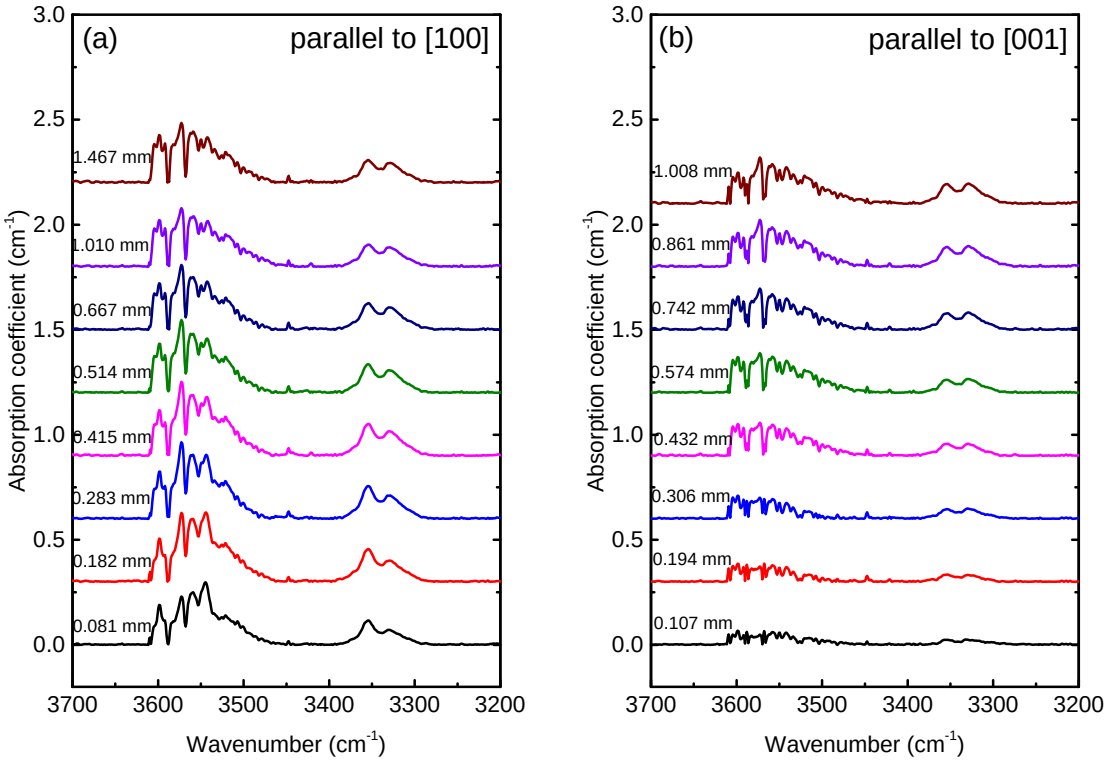

B.2 Chemical diffusivities from diffusion profiles

Figure B.2.1: Chemical diffusion coefficient for each IR band parallel to each of the three orthogonal directions of sample SC14-6:(a) parallel to [100], (b) parallel to [010], and (c) parallel to [001]. Magenta line labeled as K&M is from *Kohlstedt and Mackwell* (1998). Green line is the chemical diffusivity obtained from the diffusion profile of the overall region, 3650-3200 cm^{-1}, in an IR spectrum. Blue dash line is the average chemical diffusivity of that of each IR band.

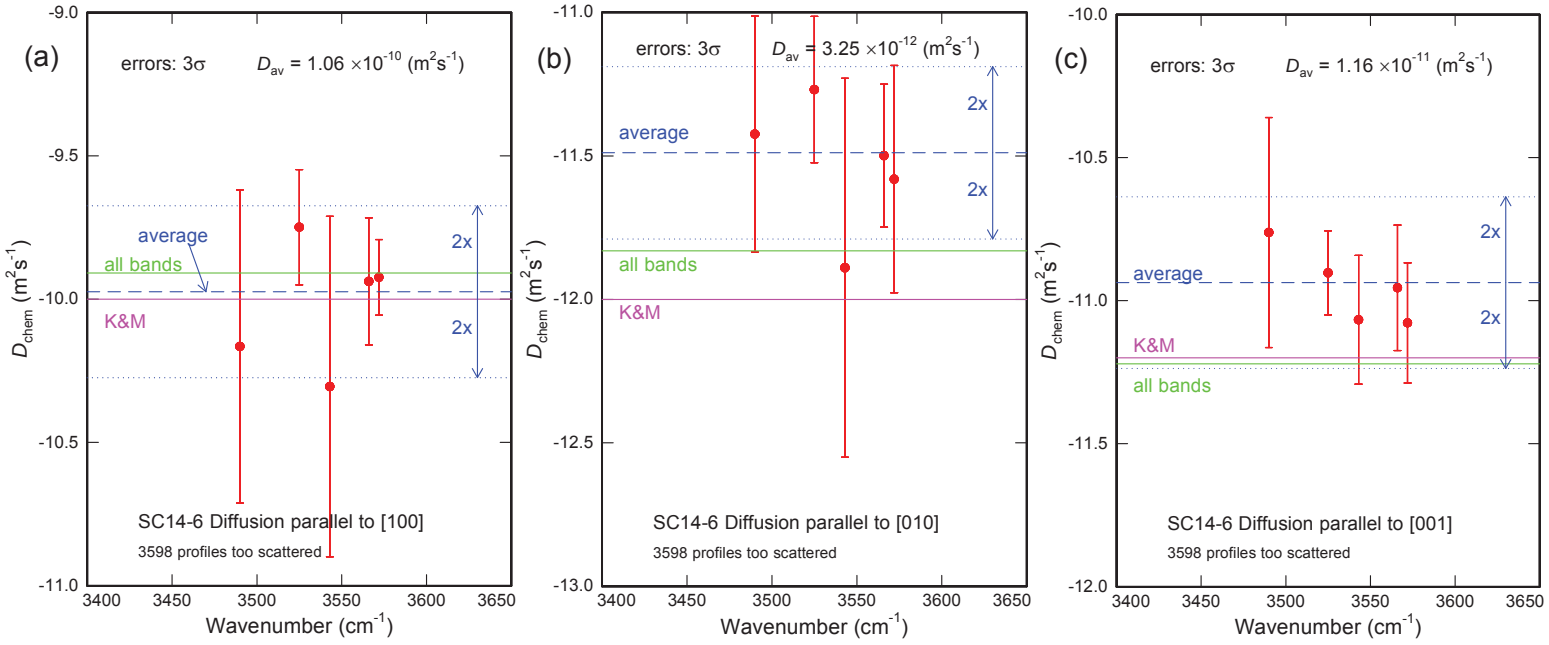

Figure B.2.2: Chemical diffusion coefficient for each IR band parallel to each of the three orthogonal directions of sample SC16-4:(a) parallel to [100], (b) parallel to [010], and (c) parallel to [001]. Magenta line labeled as K&M is from *Kohlstedt and Mackwell* (1998). Green line is the chemical diffusivity obtained from the diffusion profile of the overall region, 3650-3200 cm^{-1}, in an IR spectrum. Blue dash line is the average chemical diffusivity of that of each IR band.

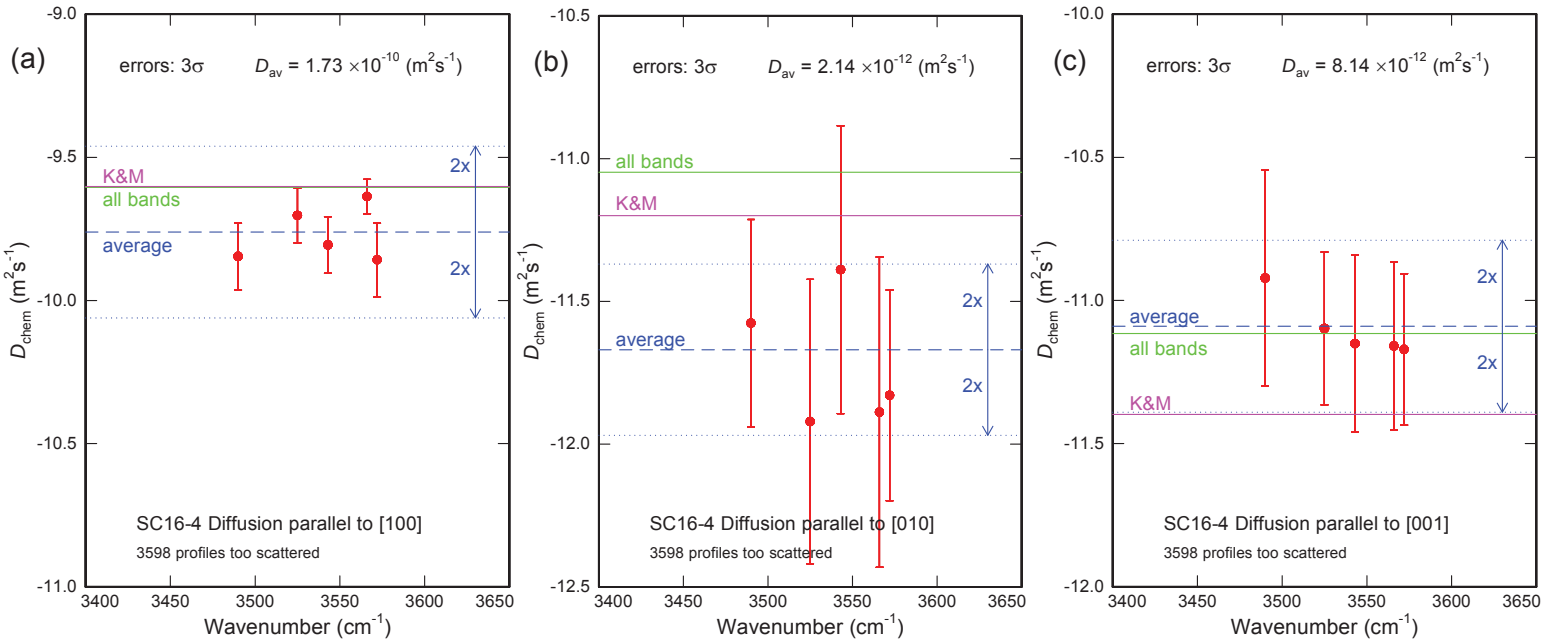

Figure B.2.3: Chemical diffusion coefficient for each IR band parallel to each of the three orthogonal directions of sample SC31-2:(a) parallel to [100], (b) parallel to [010], and (c) parallel to [001]. Magenta line labeled as K&M is from *Kohlstedt and Mackwell* (1998). Green line is the chemical diffusivity obtained from the diffusion profile of the overall region, 3650-3200 cm^{-1}, in an IR spectrum. Blue dash line is the average chemical diffusivity of that of each IR band.

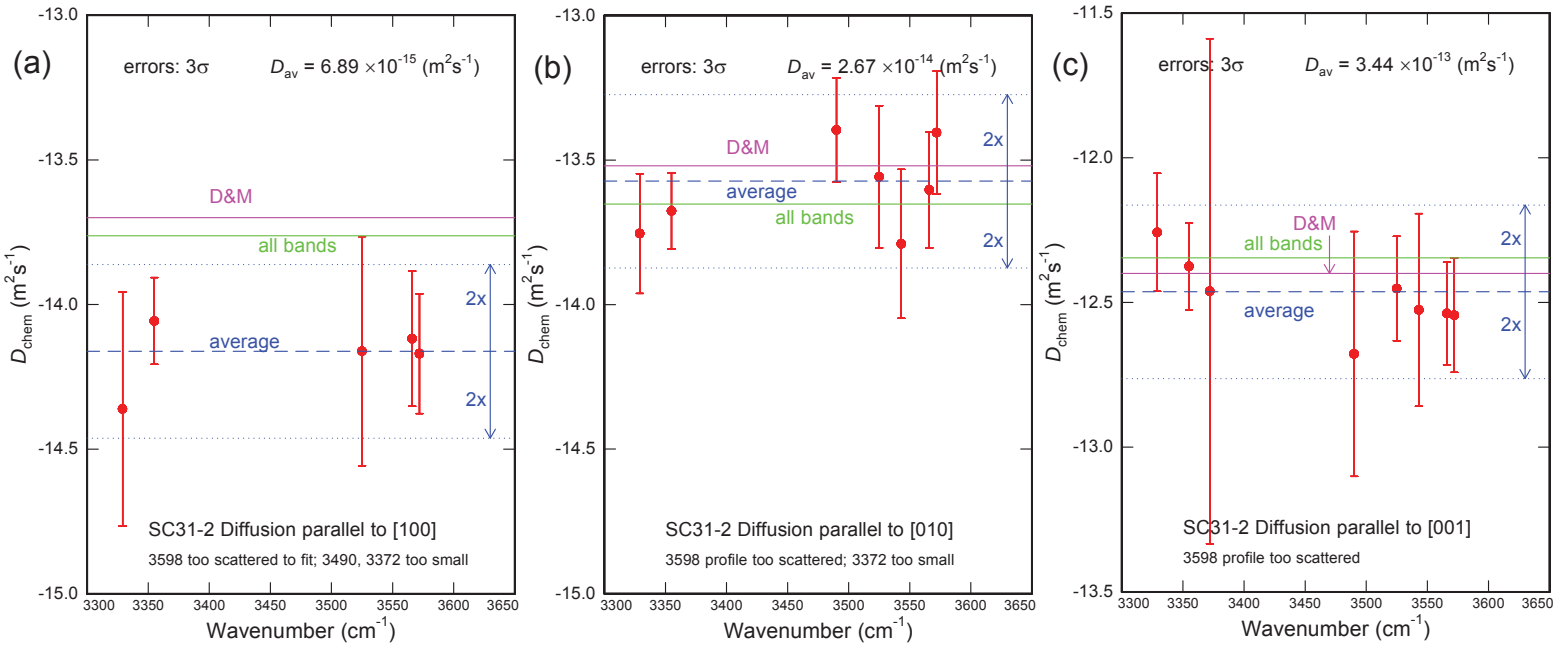

Figure B.2.4: Chemical diffusion coefficient for each IR band parallel to each of the three orthogonal directions of sample SC31-3:(a) parallel to [100], (b) parallel to [010], and (c) parallel to [001]. Magenta line labeled as K&M is from *Kohlstedt and Mackwell* (1998). Green line is the chemical diffusivity obtained from the diffusion profile of the overall region, 3650-3200 cm^{-1}, in an IR spectrum. Blue dash line is the average chemical diffusivity of that of each IR band.

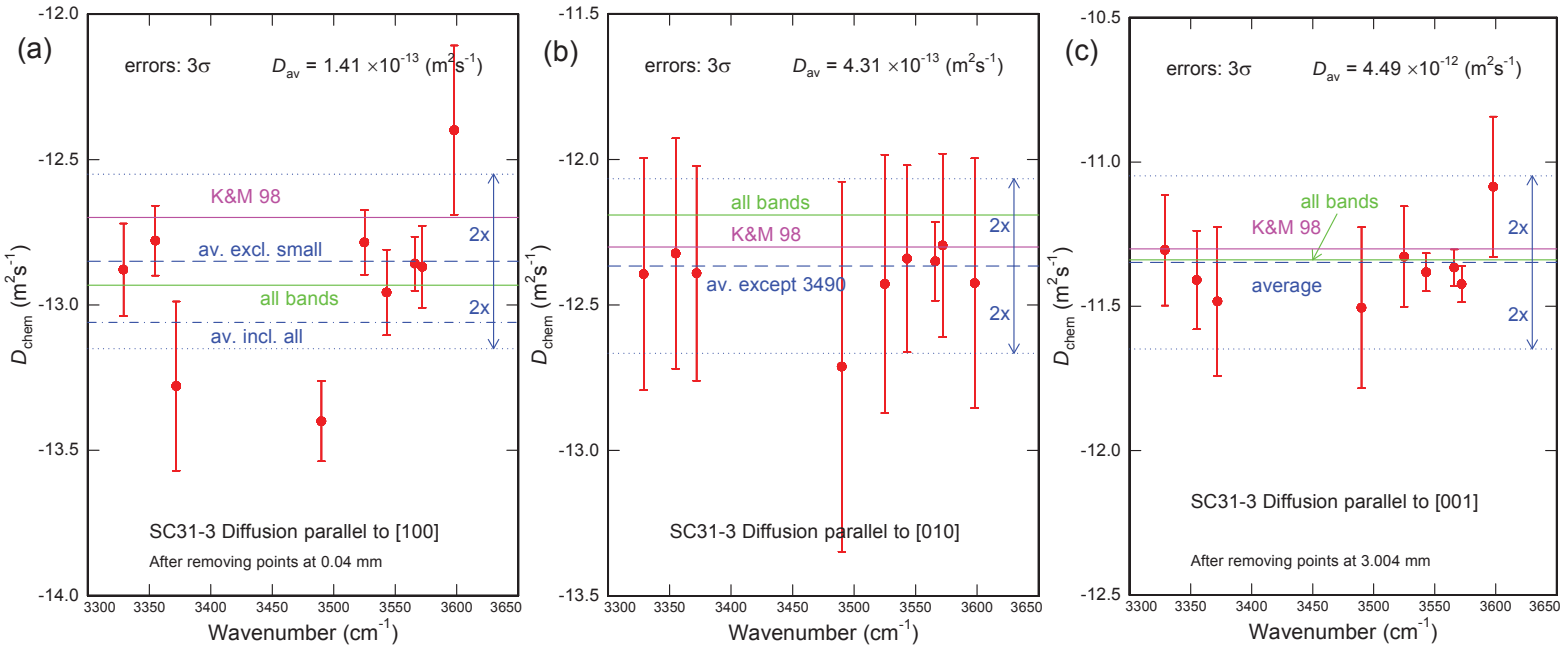

Figure B.2.5: Chemical diffusion coefficient for each IR band parallel to each of the three orthogonal directions of sample SC31-5:(a) parallel to [100], and (b) parallel to [001]. Magenta line labeled as K&M is from *Kohlstedt and Mackwell* (1998). Green line is the chemical diffusivity obtained from the diffusion profile of the overall region, 3650-3200 cm^{-1}, in an IR spectrum. Blue dash line is the average chemical diffusivity of that of each IR band.

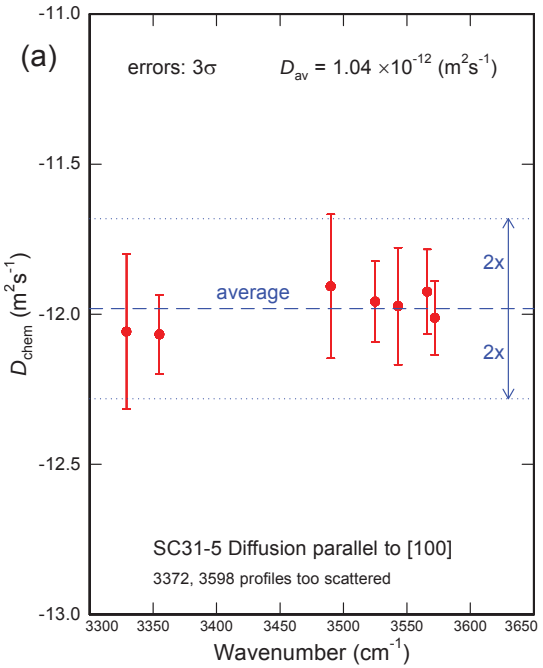

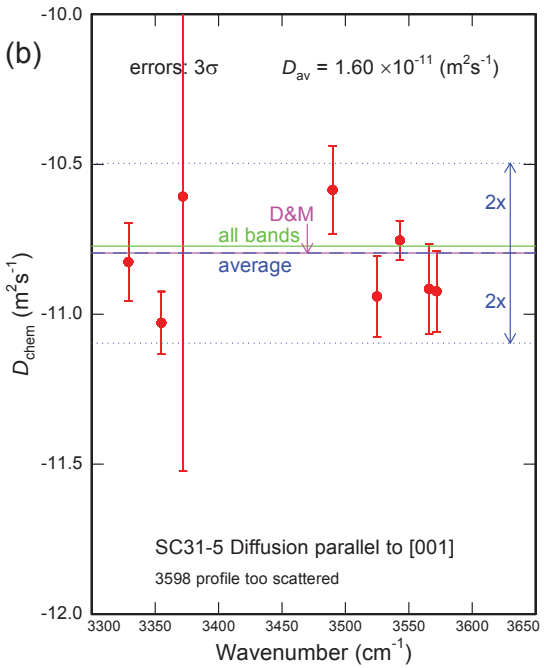

B.3 Inward (hydration) chemical diffusion profiles

Figure B.3.1: OH concentration versus positions (x, y, z) along [100], [010], and [001] of sample SC14-6. Title of each plot has the format of "SC14-6" + "diffusion profile direction (a, b, or c)" + "wavenumber". First three plots in the top row are diffusion profiles of the overall region, 3650-3200 cm^{-1}, in IR spectra along [100], [010], and [001].

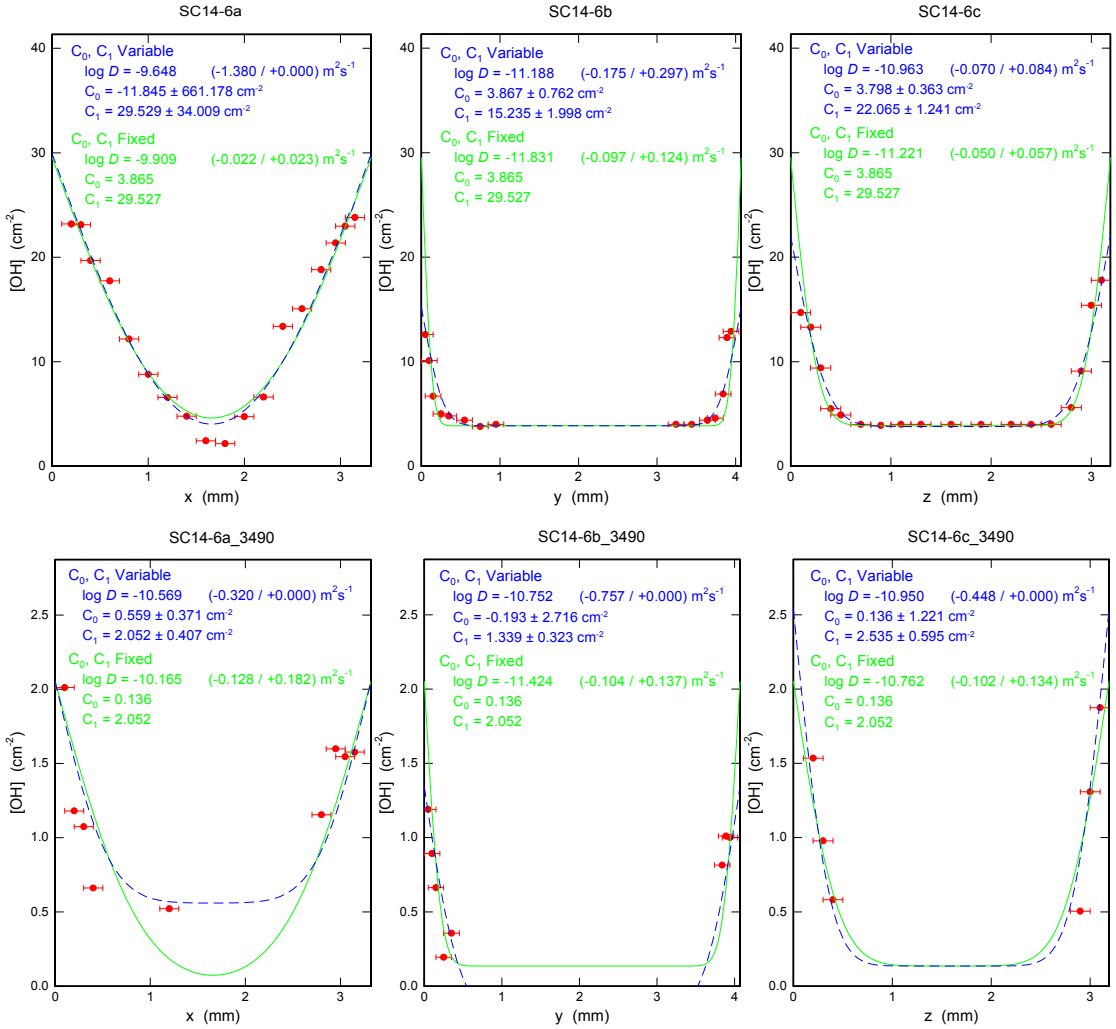

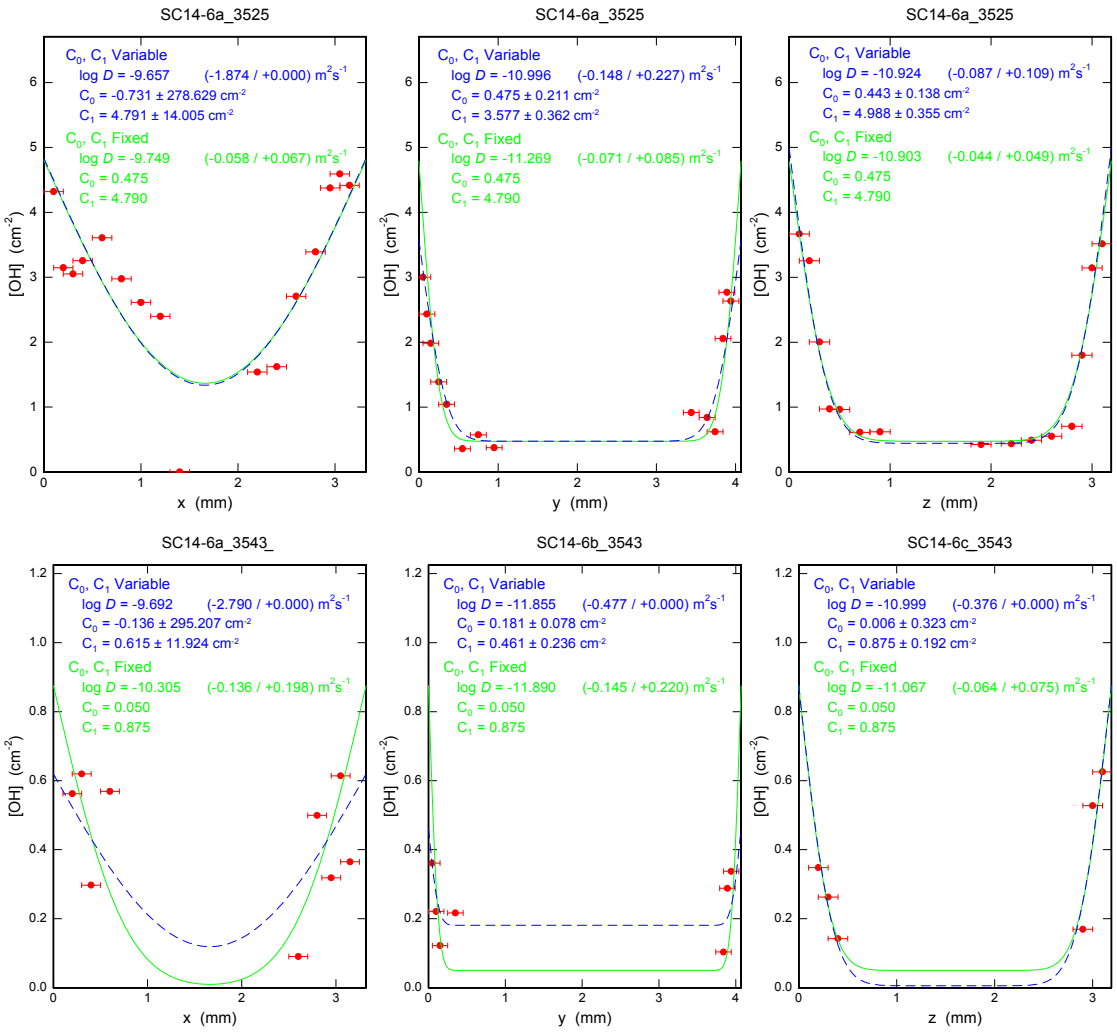
SC14-6a_3525
C0, C1 Variable
log D = -9.657 (-1.874 / +0.000) m2s-1
C0 = -0.731 ± 278.629 cm-2
C1 = 4.791 ± 14.005 cm-2
C0, C1 Fixed
log D = -9.749 (-0.058 / +0.067) m2s-1
C0 = 0.475
C1 = 4.790
[OH] (cm-2)
x (mm)
SC14-6a_3525
C0, C1 Variable
log D = -10.996 (-0.148 / +0.227) m2s-1
C0 = 0.475 ± 0.211 cm-2
C1 = 3.577 ± 0.362 cm-2
C0, C1 Fixed
log D = -11.269 (-0.071 / +0.085) m2s-1
C0 = 0.475
C1 = 4.790
[OH] (cm-2)
y (mm)
SC14-6a_3525
C0, C1 Variable
log D = -10.924 (-0.087 / +0.109) m2s-1
C0 = 0.443 ± 0.138 cm-2
C1 = 4.988 ± 0.355 cm-2
C0, C1 Fixed
log D = -10.903 (-0.044 / +0.049) m2s-1
C0 = 0.475
C1 = 4.790
[OH] (cm-2)
z (mm)
SC14-6a_3543_
C0, C1 Variable
log D = -9.692 (-2.790 / +0.000) m2s-1
C0 = -0.136 ± 295.207 cm-2
C1 = 0.615 ± 11.924 cm-2
C0, C1 Fixed
log D = -10.305 (-0.136 / +0.198) m2s-1
C0 = 0.050
C1 = 0.875
[OH] (cm-2)
x (mm)
SC14-6b_3543
C0, C1 Variable
log D = -11.855 (-0.477 / +0.000) m2s-1
C0 = 0.181 ± 0.078 cm-2
C1 = 0.461 ± 0.236 cm-2
C0, C1 Fixed
log D = -11.890 (-0.145 / +0.220) m2s-1
C0 = 0.050
C1 = 0.875
[OH] (cm-2)
y (mm)
SC14-6c_3543
C0, C1 Variable
log D = -10.999 (-0.376 / +0.000) m2s-1
C0 = 0.006 ± 0.323 cm-2
C1 = 0.875 ± 0.192 cm-2
C0, C1 Fixed
log D = -11.067 (-0.064 / +0.075) m2s-1
C0 = 0.050
C1 = 0.875
[OH] (cm-2)
z (mm)

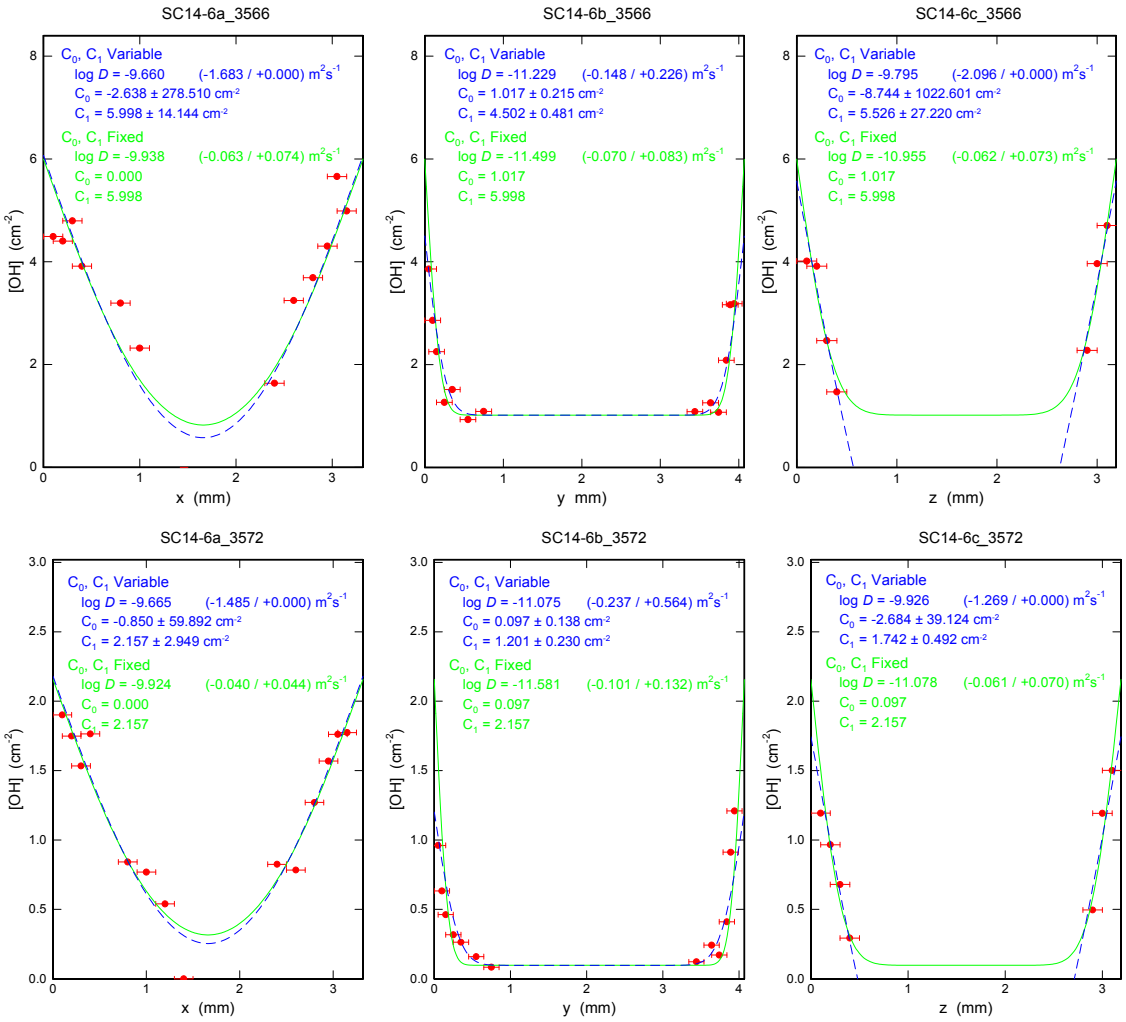
SC14-6a_3566
C0, C1 Variable
log D = -9.660 (-1.683 / +0.000) m2s-1
C0 = -2.638 ± 278.510 cm-2
C1 = 5.998 ± 14.144 cm-2
C0, C1 Fixed
log D = -9.938 (-0.063 / +0.074) m2s-1
C0 = 0.000
C1 = 5.998
[OH] (cm-2)
x (mm)
SC14-6b_3566
C0, C1 Variable
log D = -11.229 (-0.148 / +0.226) m2s-1
C0 = 1.017 ± 0.215 cm-2
C1 = 4.502 ± 0.481 cm-2
C0, C1 Fixed
log D = -11.499 (-0.070 / +0.083) m2s-1
C0 = 1.017
C1 = 5.998
[OH] (cm-2)
y mm)
SC14-6c_3566
C0, C1 Variable
log D = -9.795 (-2.096 / +0.000) m2s-1
C0 = -8.744 ± 1022.601 cm-2
C1 = 5.526 ± 27.220 cm-2
C0, C1 Fixed
log D = -10.955 (-0.062 / +0.073) m2s-1
C0 = 1.017
C1 = 5.998
[OH] (cm-2)
z (mm)
SC14-6a_3572
C0, C1 Variable
log D = -9.665 (-1.485 / +0.000) m2s-1
C0 = -0.850 ± 59.892 cm-2
C1 = 2.157 ± 2.949 cm-2
C0, C1 Fixed
log D = -9.924 (-0.040 / +0.044) m2s-1
C0 = 0.000
C1 = 2.157
[OH] (cm-2)
x (mm)
SC14-6b_3572
C0, C1 Variable
log D = -11.075 (-0.237 / +0.564) m2s-1
C0 = 0.097 ± 0.138 cm-2
C1 = 1.201 ± 0.230 cm-2
C0, C1 Fixed
log D = -11.581 (-0.101 / +0.132) m2s-1
C0 = 0.097
C1 = 2.157
[OH] (cm-2)
y (mm)
SC14-6c_3572
C0, C1 Variable
log D = -9.926 (-1.269 / +0.000) m2s-1
C0 = -2.684 ± 39.124 cm-2
C1 = 1.742 ± 0.492 cm-2
C0, C1 Fixed
log D = -11.078 (-0.061 / +0.070) m2s-1
C0 = 0.097
C1 = 2.157
[OH] (cm-2)
z (mm)

Figure B.3.2: OH concentration versus positions (x, y, z) along [100], [010], and [001] of sample SC16-4. Title of each plot has the format of "SC16-4" + "diffusion profile direction (a, b, or c)" + "wavenumber". First three plots in the top row are diffusion profiles of the overall region, 3650-3200 cm^{-1}, in IR spectra along [100], [010], and [001].

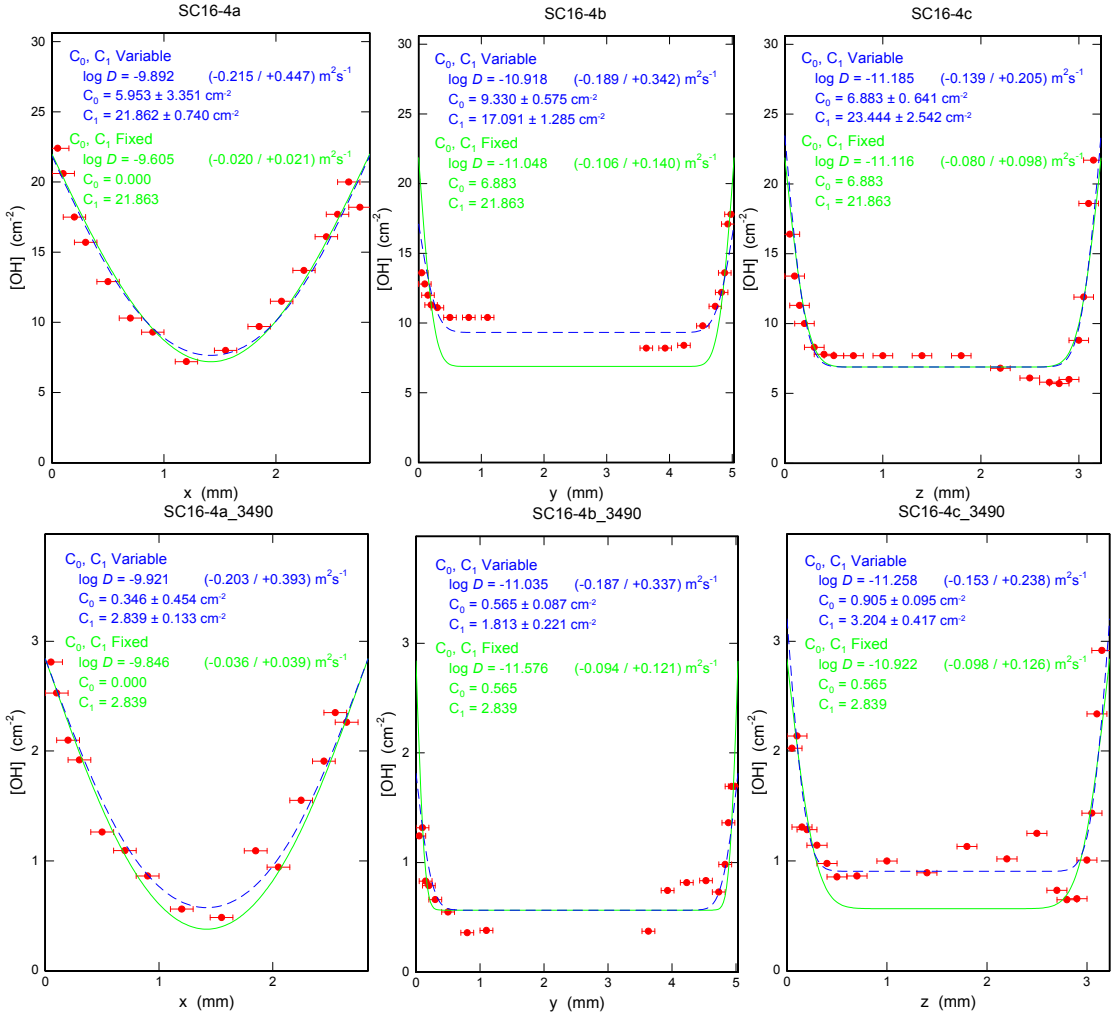

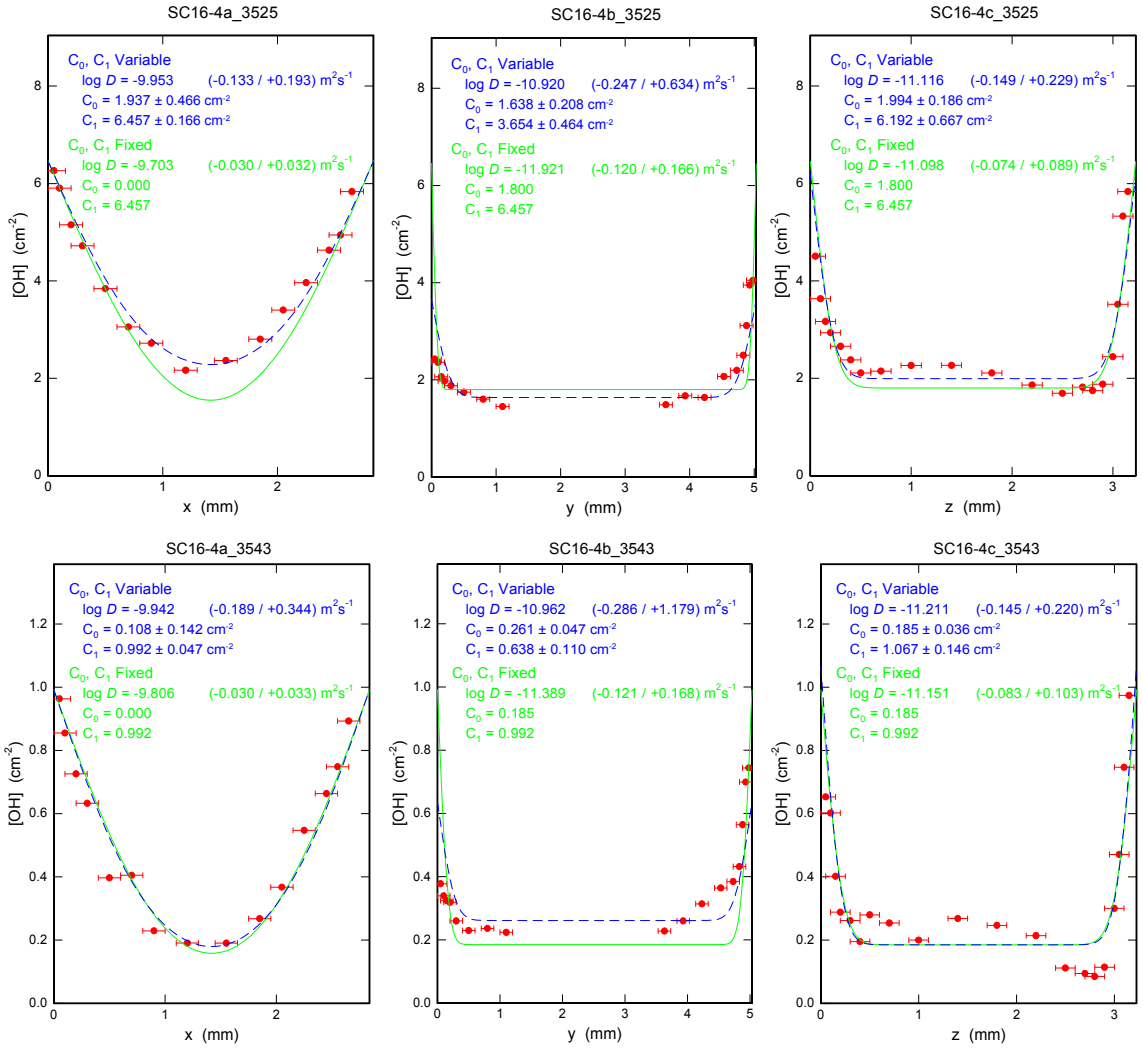
SC16-4a_3525
C0, C1 Variable
log D = -9.953 (-0.133 / +0.193) m2s-1
C0 = 1.937 ± 0.466 cm-2
C1 = 6.457 ± 0.166 cm-2
C0, C1 Fixed
log D = -9.703 (-0.030 / +0.032) m2s-1
C0 = 0.000
C1 = 6.457
[OH] (cm-2)
x (mm)
SC16-4b_3525
C0, C1 Variable
log D = -10.920 (-0.247 / +0.634) m2s-1
C0 = 1.638 ± 0.208 cm-2
C1 = 3.654 ± 0.464 cm-2
C0, C1 Fixed
log D = -11.921 (-0.120 / +0.166) m2s-1
C0 = 1.800
C1 = 6.457
[OH] (cm-2)
y (mm)
SC16-4c_3525
C0, C1 Variable
log D = -11.116 (-0.149 / +0.229) m2s-1
C0 = 1.994 ± 0.186 cm-2
C1 = 6.192 ± 0.667 cm-2
C0, C1 Fixed
log D = -11.098 (-0.074 / +0.089) m2s-1
C0 = 1.800
C1 = 6.457
[OH] (cm-2)
z (mm)
SC16-4a_3543
C0, C1 Variable
log D = -9.942 (-0.189 / +0.344) m2s-1
C0 = 0.108 ± 0.142 cm-2
C1 = 0.992 ± 0.047 cm-2
C0, C1 Fixed
log D = -9.806 (-0.030 / +0.033) m2s-1
C0 = 0.000
C1 = 0.992
[OH] (cm-2)
x (mm)
SC16-4b_3543
C0, C1 Variable
log D = -10.962 (-0.286 / +1.179) m2s-1
C0 = 0.261 ± 0.047 cm-2
C1 = 0.638 ± 0.110 cm-2
C0, C1 Fixed
log D = -11.389 (-0.121 / +0.168) m2s-1
C0 = 0.185
C1 = 0.992
[OH] (cm-2)
y (mm)
SC16-4c_3543
C0, C1 Variable
log D = -11.211 (-0.145 / +0.220) m2s-1
C0 = 0.185 ± 0.036 cm-2
C1 = 1.067 ± 0.146 cm-2
C0, C1 Fixed
log D = -11.151 (-0.083 / +0.103) m2s-1
C0 = 0.185
C1 = 0.992
[OH] (cm-2)
z (mm)

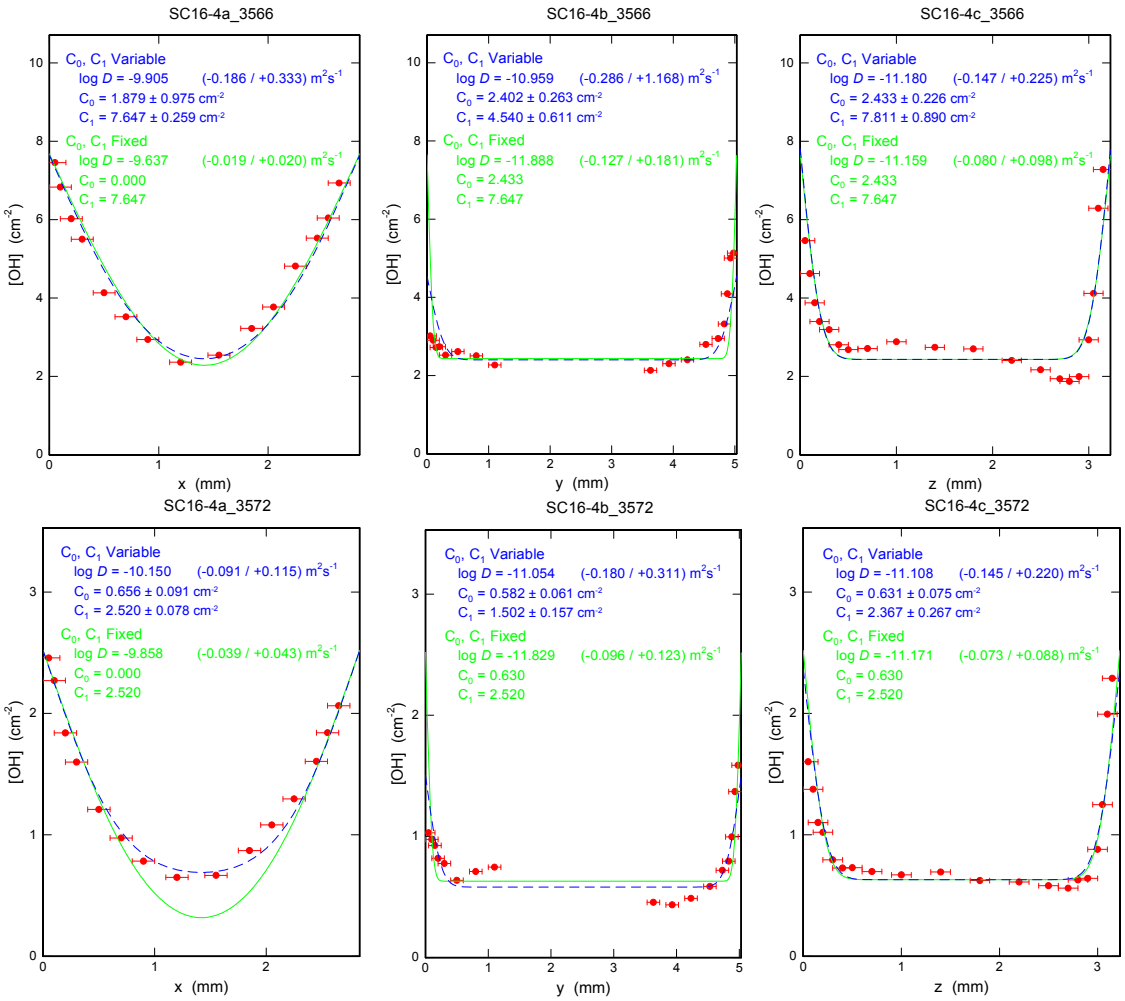
SC16-4a_3566
C0, C1 Variable
log D = -9.905 (-0.186 / +0.333) m2s-1
C0 = 1.879 ± 0.975 cm-2
C1 = 7.647 ± 0.259 cm-2
C0, C1 Fixed
log D = -9.637 (-0.019 / +0.020) m2s-1
C0 = 0.000
C1 = 7.647
[OH] (cm-2)
x (mm)
SC16-4b_3566
C0, C1 Variable
log D = -10.959 (-0.286 / +1.168) m2s-1
C0 = 2.402 ± 0.263 cm-2
C1 = 4.540 ± 0.611 cm-2
C0, C1 Fixed
log D = -11.888 (-0.127 / +0.181) m2s-1
C0 = 2.433
C1 = 7.647
[OH] (cm-2)
y (mm)
SC16-4c_3566
C0, C1 Variable
log D = -11.180 (-0.147 / +0.225) m2s-1
C0 = 2.433 ± 0.226 cm-2
C1 = 7.811 ± 0.890 cm-2
C0, C1 Fixed
log D = -11.159 (-0.080 / +0.098) m2s-1
C0 = 2.433
C1 = 7.647
[OH] (cm-2)
z (mm)
SC16-4a_3572
C0, C1 Variable
log D = -10.150 (-0.091 / +0.115) m2s-1
C0 = 0.656 ± 0.091 cm-2
C1 = 2.520 ± 0.078 cm-2
C0, C1 Fixed
log D = -9.858 (-0.039 / +0.043) m2s-1
C0 = 0.000
C1 = 2.520
[OH] (cm-2)
x (mm)
SC16-4b_3572
C0, C1 Variable
log D = -11.054 (-0.180 / +0.311) m2s-1
C0 = 0.582 ± 0.061 cm-2
C1 = 1.502 ± 0.157 cm-2
C0, C1 Fixed
log D = -11.829 (-0.096 / +0.123) m2s-1
C0 = 0.630
C1 = 2.520
[OH] (cm-2)
y (mm)
SC16-4c_3572
C0, C1 Variable
log D = -11.108 (-0.145 / +0.220) m2s-1
C0 = 0.631 ± 0.075 cm-2
C1 = 2.367 ± 0.267 cm-2
C0, C1 Fixed
log D = -11.171 (-0.073 / +0.088) m2s-1
C0 = 0.630
C1 = 2.520
[OH] (cm-2)
z (mm)

Figure B.3.3: OH concentration versus positions (x, y, z) along [100], [010], and [001] of sample SC31-2. Title of each plot has the format of ”SC31-2” + ”diffusion profile direction (a, b, or c)” + ”wavenumber”. First three plots in the top row are diffusion profiles of the overall region, 3650-3200 cm^{-1}, in IR spectra along [100], [010], and [001].

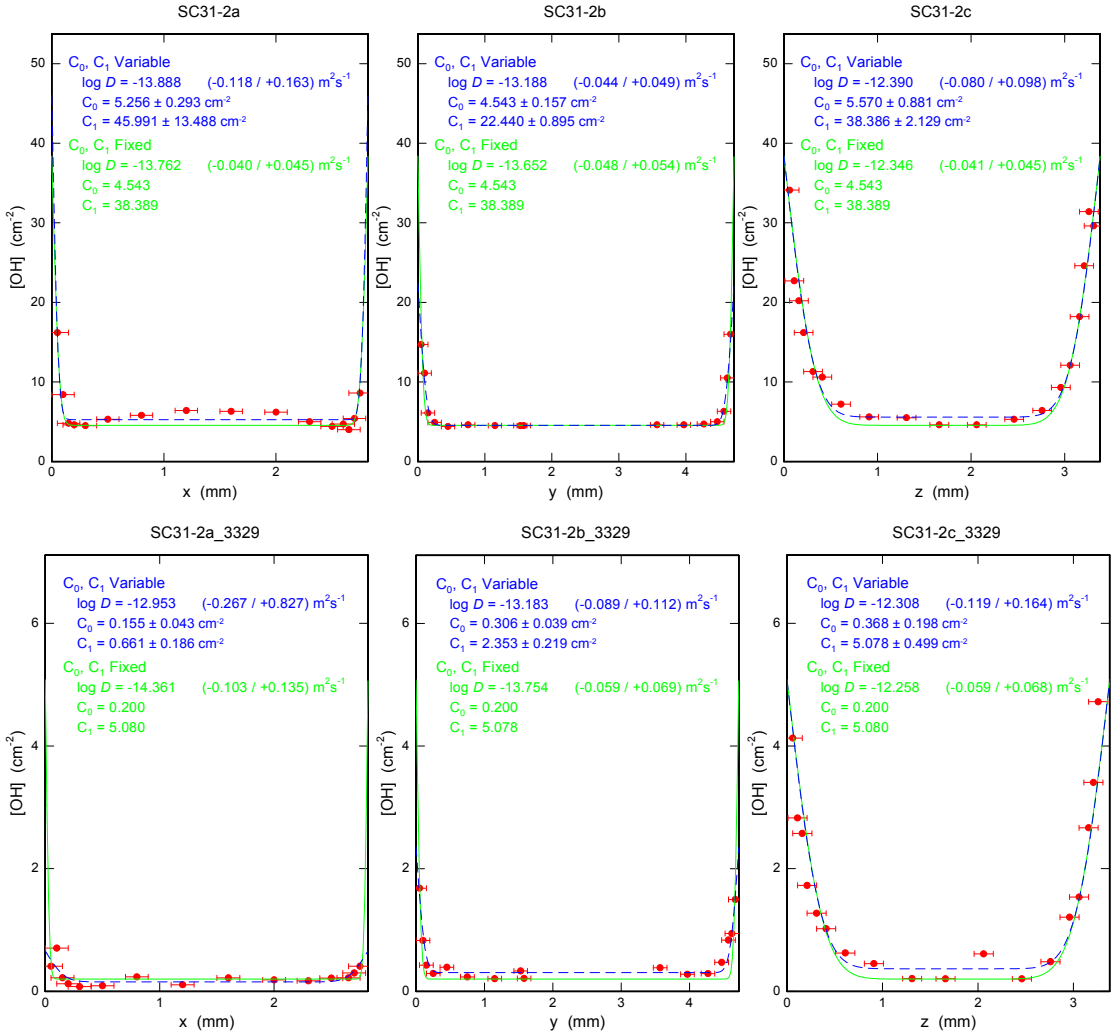

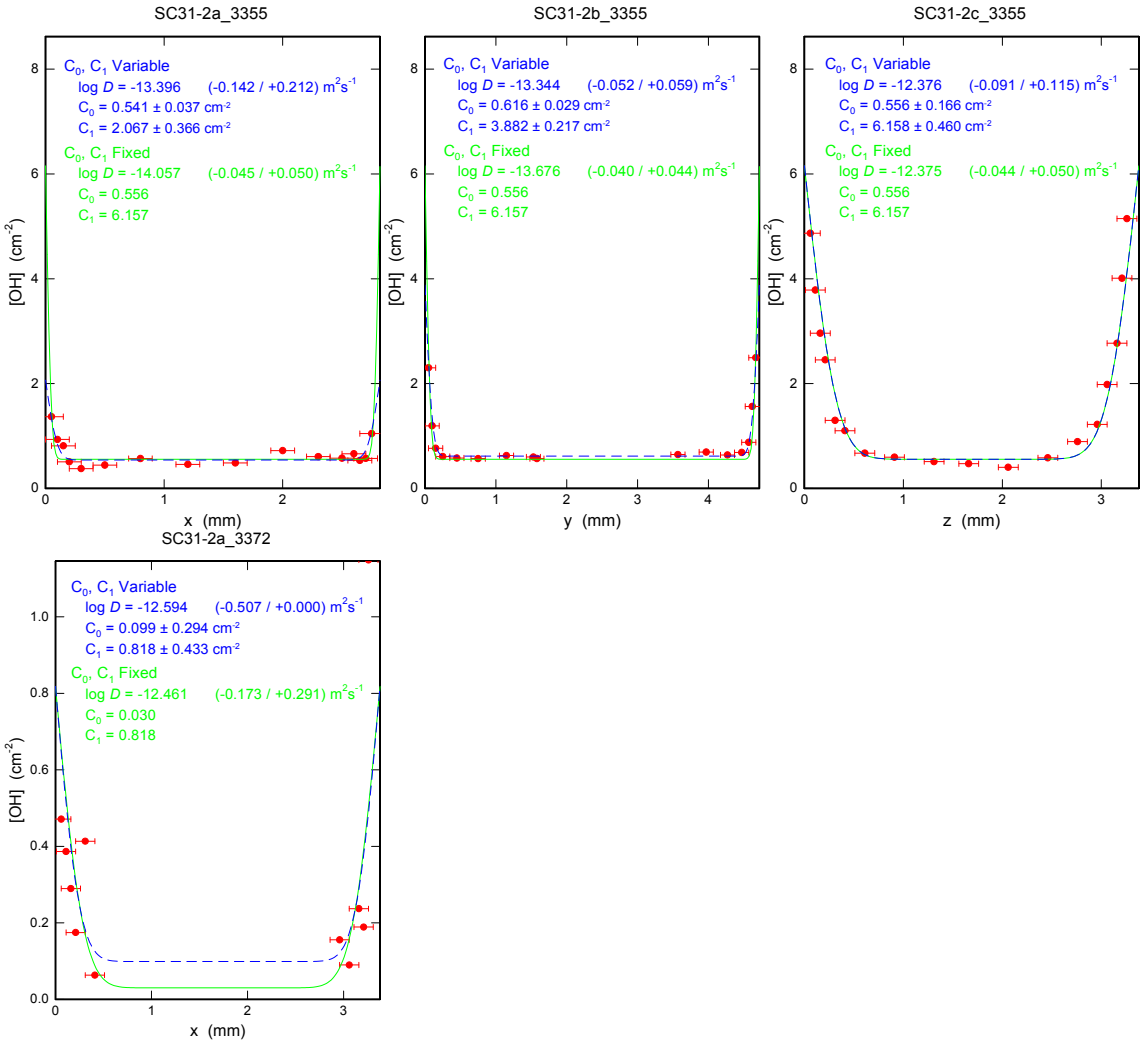
SC31-2a_3355
C0, C1 Variable
log D = -13.396 (-0.142 / +0.212) m2s-1
C0 = 0.541 ± 0.037 cm-2
C1 = 2.067 ± 0.366 cm-2
C0, C1 Fixed
log D = -14.057 (-0.045 / +0.050) m2s-1
C0 = 0.556
C1 = 6.157
[OH] (cm-2)
x (mm)
SC31-2b_3355
C0, C1 Variable
log D = -13.344 (-0.052 / +0.059) m2s-1
C0 = 0.616 ± 0.029 cm-2
C1 = 3.882 ± 0.217 cm-2
C0, C1 Fixed
log D = -13.676 (-0.040 / +0.044) m2s-1
C0 = 0.556
C1 = 6.157
[OH] (cm-2)
y (mm)
SC31-2c_3355
C0, C1 Variable
log D = -12.376 (-0.091 / +0.115) m2s-1
C0 = 0.556 ± 0.166 cm-2
C1 = 6.158 ± 0.460 cm-2
C0, C1 Fixed
log D = -12.375 (-0.044 / +0.050) m2s-1
C0 = 0.556
C1 = 6.157
[OH] (cm-2)
z (mm)
SC31-2a_3372
C0, C1 Variable
log D = -12.594 (-0.507 / +0.000) m2s-1
C0 = 0.099 ± 0.294 cm-2
C1 = 0.818 ± 0.433 cm-2
C0, C1 Fixed
log D = -12.461 (-0.173 / +0.291) m2s-1
C0 = 0.030
C1 = 0.818
[OH] (cm-2)
x (mm)

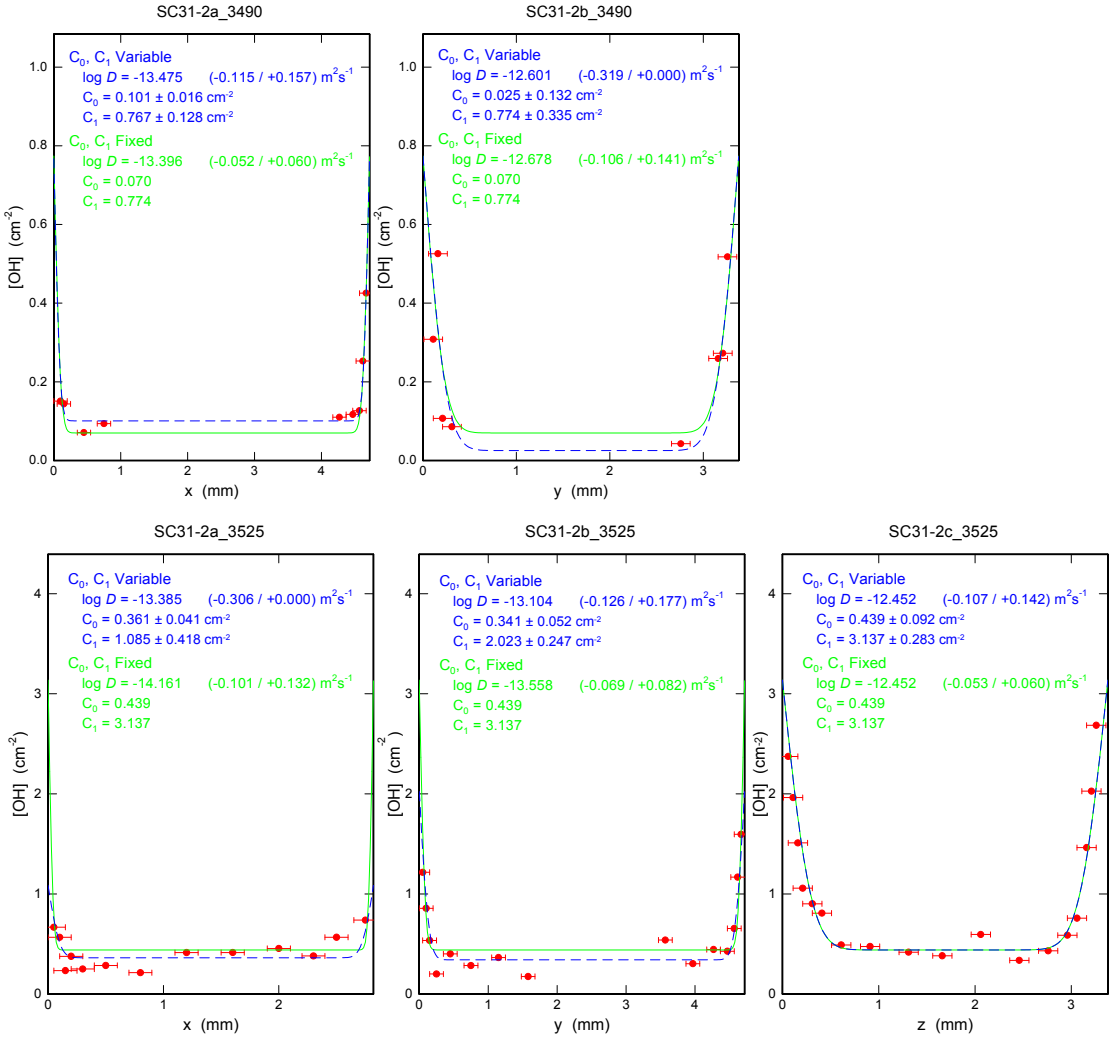
SC31-2a_3490
C0, C1 Variable
log D = -13.475 (-0.115 / +0.157) m2s-1
C0 = 0.101 ± 0.016 cm-2
C1 = 0.767 ± 0.128 cm-2
C0, C1 Fixed
log D = -13.396 (-0.052 / +0.060) m2s-1
C0 = 0.070
C1 = 0.774
[OH] (cm-2)
x (mm)
SC31-2b_3490
C0, C1 Variable
log D = -12.601 (-0.319 / +0.000) m2s-1
C0 = 0.025 ± 0.132 cm-2
C1 = 0.774 ± 0.335 cm-2
C0, C1 Fixed
log D = -12.678 (-0.106 / +0.141) m2s-1
C0 = 0.070
C1 = 0.774
[OH] (cm-2)
y (mm)
SC31-2a_3525
C0, C1 Variable
log D = -13.385 (-0.306 / +0.000) m2s-1
C0 = 0.361 ± 0.041 cm-2
C1 = 1.085 ± 0.418 cm-2
C0, C1 Fixed
log D = -14.161 (-0.101 / +0.132) m2s-1
C0 = 0.439
C1 = 3.137
[OH] (cm-2)
x (mm)
SC31-2b_3525
C0, C1 Variable
log D = -13.104 (-0.126 / +0.177) m2s-1
C0 = 0.341 ± 0.052 cm-2
C1 = 2.023 ± 0.247 cm-2
C0, C1 Fixed
log D = -13.558 (-0.069 / +0.082) m2s-1
C0 = 0.439
C1 = 3.137
[OH] (cm-2)
y (mm)
SC31-2c_3525
C0, C1 Variable
log D = -12.452 (-0.107 / +0.142) m2s-1
C0 = 0.439 ± 0.092 cm-2
C1 = 3.137 ± 0.283 cm-2
C0, C1 Fixed
log D = -12.452 (-0.053 / +0.060) m2s-1
C0 = 0.439
C1 = 3.137
[OH] (cm-2)
z (mm)

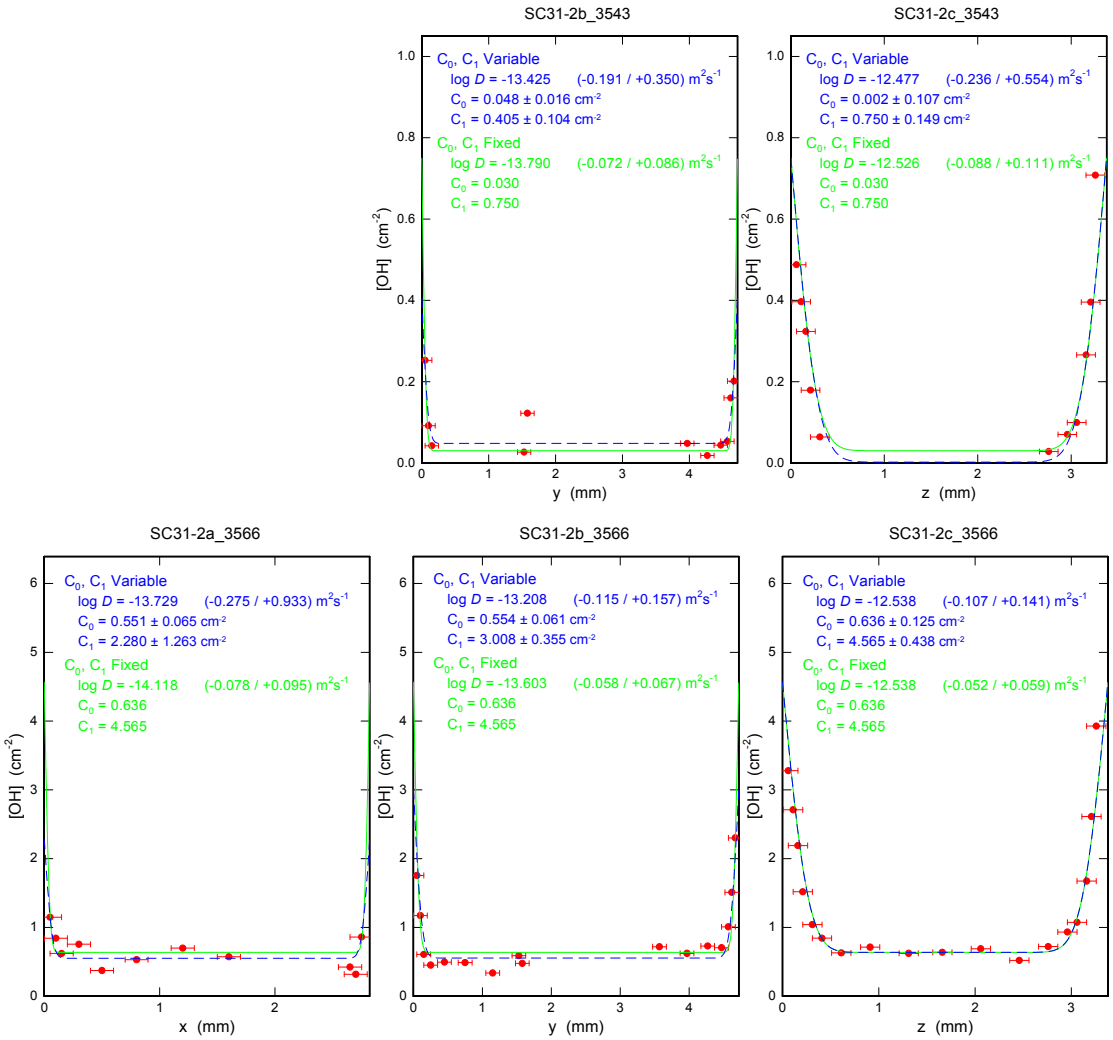
SC31-2b_3543
C0, C1 Variable
log D = -13.425 (-0.191 / +0.350) m2s-1
C0 = 0.048 ± 0.016 cm-2
C1 = 0.405 ± 0.104 cm-2
C0, C1 Fixed
log D = -13.790 (-0.072 / +0.086) m2s-1
C0 = 0.030
C1 = 0.750
[OH] (cm-2)
y (mm)
SC31-2c_3543
C0, C1 Variable
log D = -12.477 (-0.236 / +0.554) m2s-1
C0 = 0.002 ± 0.107 cm-2
C1 = 0.750 ± 0.149 cm-2
C0, C1 Fixed
log D = -12.526 (-0.088 / +0.111) m2s-1
C0 = 0.030
C1 = 0.750
[OH] (cm-2)
z (mm)
SC31-2a_3566
C0, C1 Variable
log D = -13.729 (-0.275 / +0.933) m2s-1
C0 = 0.551 ± 0.065 cm-2
C1 = 2.280 ± 1.263 cm-2
C0, C1 Fixed
log D = -14.118 (-0.078 / +0.095) m2s-1
C0 = 0.636
C1 = 4.565
[OH] (cm-2)
x (mm)
SC31-2b_3566
C0, C1 Variable
log D = -13.208 (-0.115 / +0.157) m2s-1
C0 = 0.554 ± 0.061 cm-2
C1 = 3.008 ± 0.355 cm-2
C0, C1 Fixed
log D = -13.603 (-0.058 / +0.067) m2s-1
C0 = 0.636
C1 = 4.565
[OH] (cm-2)
y (mm)
SC31-2c_3566
C0, C1 Variable
log D = -12.538 (-0.107 / +0.141) m2s-1
C0 = 0.636 ± 0.125 cm-2
C1 = 4.565 ± 0.438 cm-2
C0, C1 Fixed
log D = -12.538 (-0.052 / +0.059) m2s-1
C0 = 0.636
C1 = 4.565
[OH] (cm-2)
z (mm)

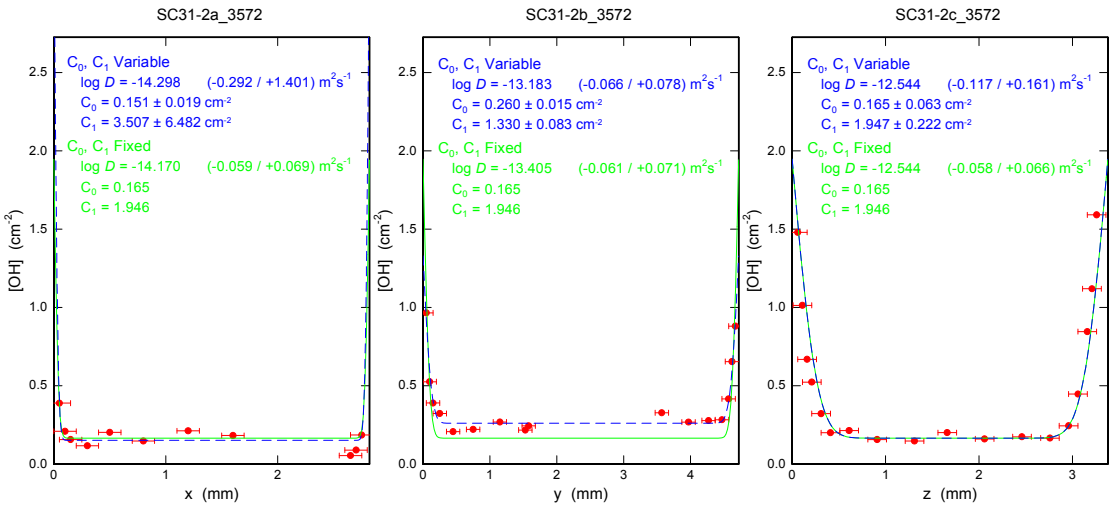
SC31-2a_3572
C0, C1 Variable
log D = -14.298 (-0.292 / +1.401) m2s-1
C0 = 0.151 ± 0.019 cm-2
C1 = 3.507 ± 6.482 cm-2
C0, C1 Fixed
log D = -14.170 (-0.059 / +0.069) m2s-1
C0 = 0.165
C1 = 1.946
[OH] (cm-2)
x (mm)
SC31-2b_3572
C0, C1 Variable
log D = -13.183 (-0.066 / +0.078) m2s-1
C0 = 0.260 ± 0.015 cm-2
C1 = 1.330 ± 0.083 cm-2
C0, C1 Fixed
log D = -13.405 (-0.061 / +0.071) m2s-1
C0 = 0.165
C1 = 1.946
[OH] (cm-2)
y (mm)
SC31-2c_3572
C0, C1 Variable
log D = -12.544 (-0.117 / +0.161) m2s-1
C0 = 0.165 ± 0.063 cm-2
C1 = 1.947 ± 0.222 cm-2
C0, C1 Fixed
log D = -12.544 (-0.058 / +0.066) m2s-1
C0 = 0.165
C1 = 1.946
[OH] (cm-2)
z (mm)

Figure B.3.4: OH concentration versus positions (x, y, z) along [100], [010], and [001] of sample SC31-3. Title of each plot has the format of "SC31-3" + "diffusion profile direction (a, b, or c)" + "wavenumber". First three plots in the top row are diffusion profiles of the overall region, 3650-3200 cm^{-1}, in IR spectra along [100], [010], and [001].

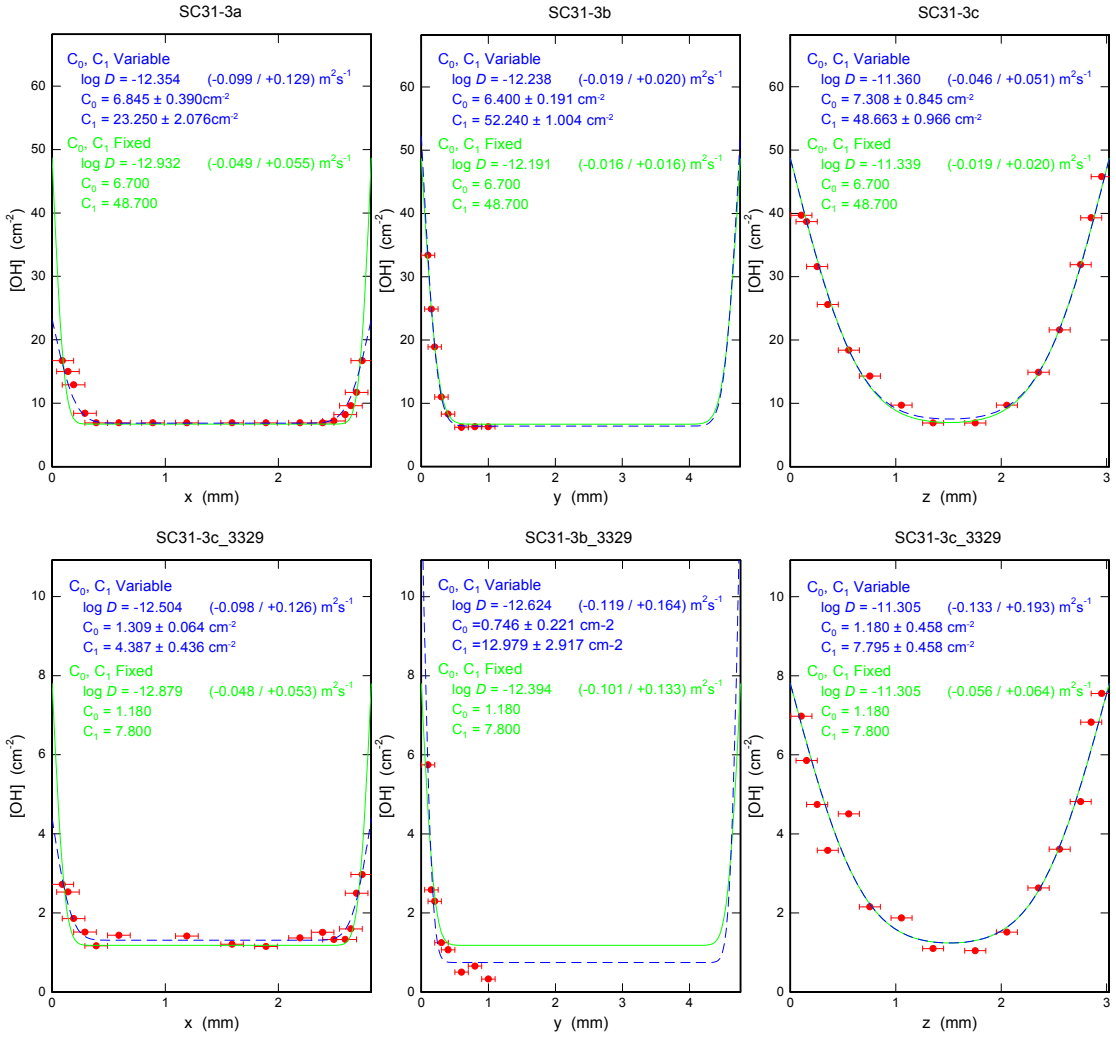

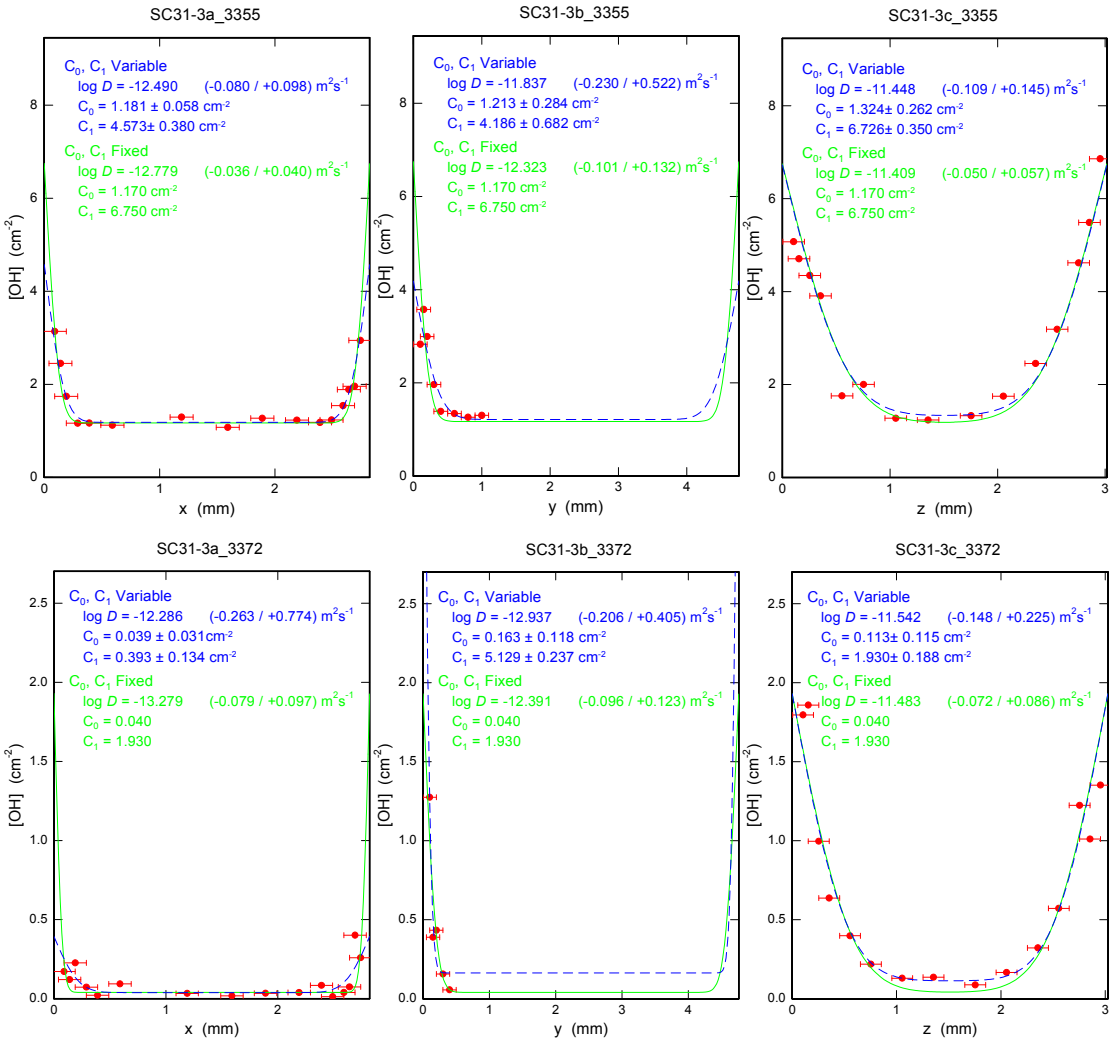
SC31-3a_3355
C0, C1 Variable
log D = -12.490 (-0.080 / +0.098) m2s-1
C0 = 1.181 ± 0.058 cm-2
C1 = 4.573± 0.380 cm-2
C0, C1 Fixed
log D = -12.779 (-0.036 / +0.040) m2s-1
C0 = 1.170 cm-2
C1 = 6.750 cm-2
[OH] (cm-2)
x (mm)
SC31-3b_3355
C0, C1 Variable
log D = -11.837 (-0.230 / +0.522) m2s-1
C0 = 1.213 ± 0.284 cm-2
C1 = 4.186 ± 0.682 cm-2
C0, C1 Fixed
log D = -12.323 (-0.101 / +0.132) m2s-1
C0 = 1.170 cm-2
C1 = 6.750 cm-2
[OH] (cm-2)
y (mm)
SC31-3c_3355
C0, C1 Variable
log D = -11.448 (-0.109 / +0.145) m2s-1
C0 = 1.324± 0.262 cm-2
C1 = 6.726± 0.350 cm-2
C0, C1 Fixed
log D = -11.409 (-0.050 / +0.057) m2s-1
C0 = 1.170 cm-2
C1 = 6.750 cm-2
[OH] (cm-2)
z (mm)
SC31-3a_3372
C0, C1 Variable
log D = -12.286 (-0.263 / +0.774) m2s-1
C0 = 0.039 ± 0.031cm-2
C1 = 0.393 ± 0.134 cm-2
C0, C1 Fixed
log D = -13.279 (-0.079 / +0.097) m2s-1
C0 = 0.040
C1 = 1.930
[OH] (cm-2)
x (mm)
SC31-3b_3372
C0, C1 Variable
log D = -12.937 (-0.206 / +0.405) m2s-1
C0 = 0.163 ± 0.118 cm-2
C1 = 5.129 ± 0.237 cm-2
C0, C1 Fixed
log D = -12.391 (-0.096 / +0.123) m2s-1
C0 = 0.040
C1 = 1.930
[OH] (cm-2)
y (mm)
SC31-3c_3372
C0, C1 Variable
log D = -11.542 (-0.148 / +0.225) m2s-1
C0 = 0.113± 0.115 cm-2
C1 = 1.930± 0.188 cm-2
C0, C1 Fixed
log D = -11.483 (-0.072 / +0.086) m2s-1
C0 = 0.040
C1 = 1.930
[OH] (cm-2)
z (mm)

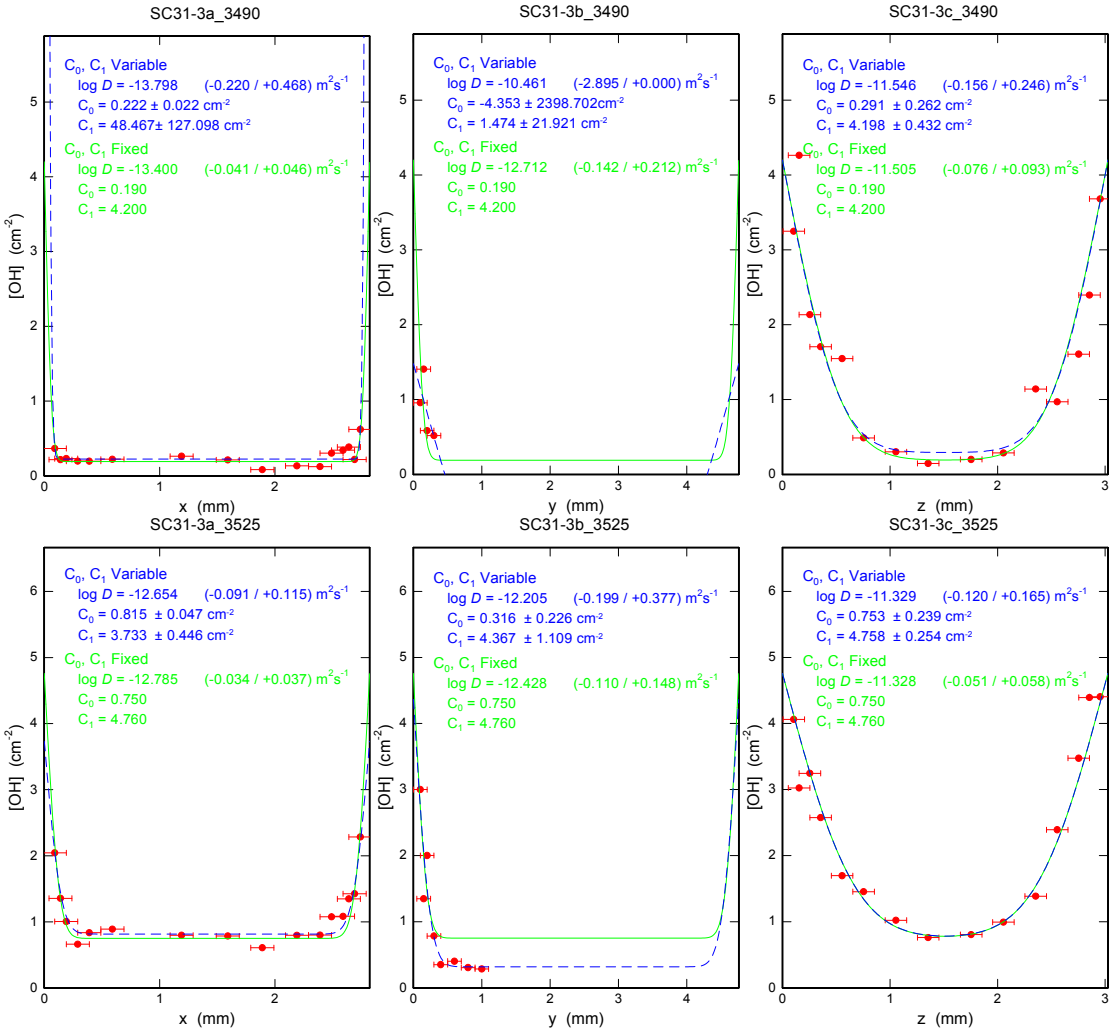
SC31-3a_3490
C0, C1 Variable
log D = -13.798 (-0.220 / +0.468) m2s-1
C0 = 0.222 ± 0.022 cm-2
C1 = 48.467± 127.098 cm-2
C0, C1 Fixed
log D = -13.400 (-0.041 / +0.046) m2s-1
C0 = 0.190
C1 = 4.200
[OH] (cm-2)
x (mm)
SC31-3b_3490
C0, C1 Variable
log D = -10.461 (-2.895 / +0.000) m2s-1
C0 = -4.353 ± 2398.702cm-2
C1 = 1.474 ± 21.921 cm-2
C0, C1 Fixed
log D = -12.712 (-0.142 / +0.212) m2s-1
C0 = 0.190
C1 = 4.200
[OH] (cm-2)
y (mm)
SC31-3c_3490
C0, C1 Variable
log D = -11.546 (-0.156 / +0.246) m2s-1
C0 = 0.291 ± 0.262 cm-2
C1 = 4.198 ± 0.432 cm-2
C0, C1 Fixed
log D = -11.505 (-0.076 / +0.093) m2s-1
C0 = 0.190
C1 = 4.200
[OH] (cm-2)
z (mm)
SC31-3a_3525
C0, C1 Variable
log D = -12.654 (-0.091 / +0.115) m2s-1
C0 = 0.815 ± 0.047 cm-2
C1 = 3.733 ± 0.446 cm-2
C0, C1 Fixed
log D = -12.785 (-0.034 / +0.037) m2s-1
C0 = 0.750
C1 = 4.760
[OH] (cm-2)
x (mm)
SC31-3b_3525
C0, C1 Variable
log D = -12.205 (-0.199 / +0.377) m2s-1
C0 = 0.316 ± 0.226 cm-2
C1 = 4.367 ± 1.109 cm-2
C0, C1 Fixed
log D = -12.428 (-0.110 / +0.148) m2s-1
C0 = 0.750
C1 = 4.760
[OH] (cm-2)
y (mm)
SC31-3c_3525
C0, C1 Variable
log D = -11.329 (-0.120 / +0.165) m2s-1
C0 = 0.753 ± 0.239 cm-2
C1 = 4.758 ± 0.254 cm-2
C0, C1 Fixed
log D = -11.328 (-0.051 / +0.058) m2s-1
C0 = 0.750
C1 = 4.760
[OH] (cm-2)
z (mm)

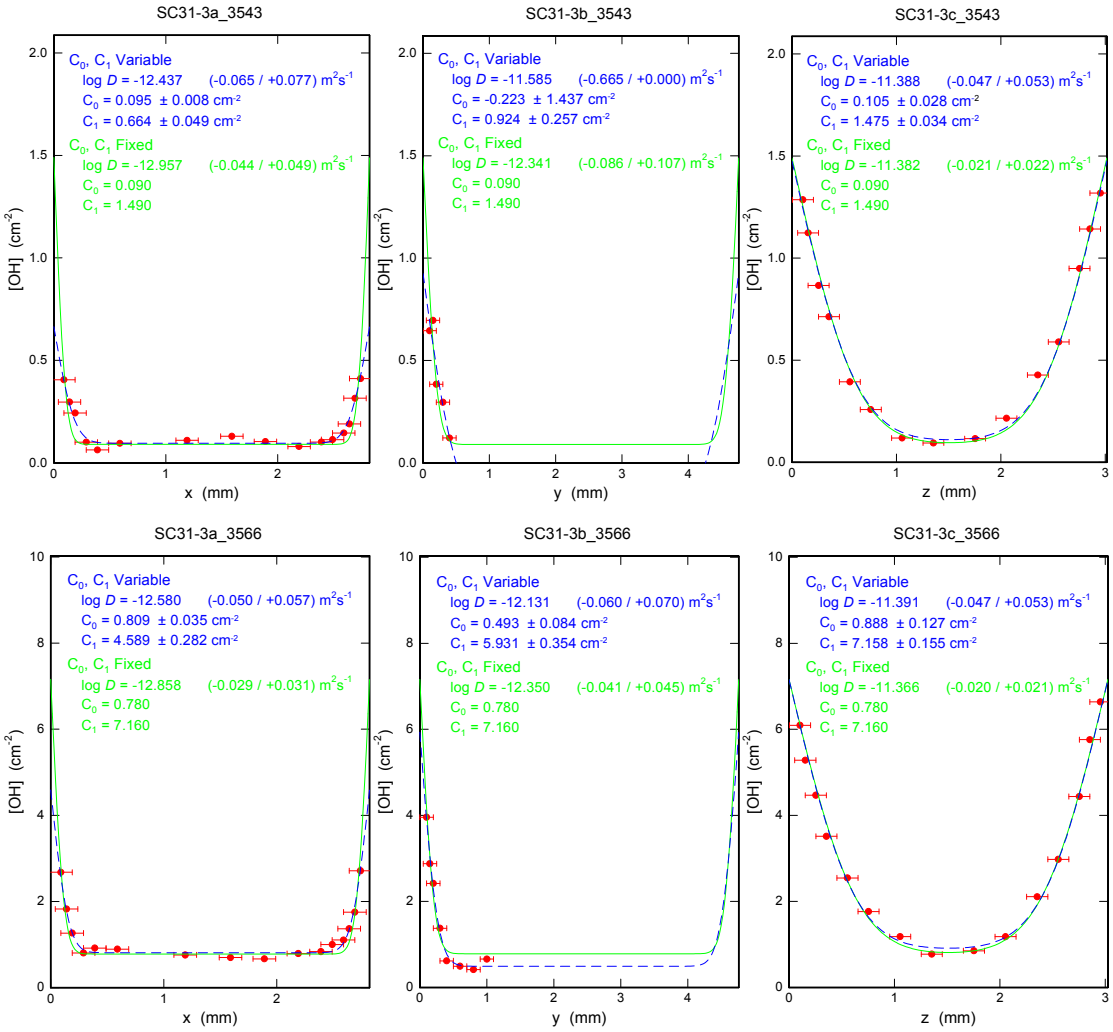
SC31-3a_3543
C0, C1 Variable
log D = -12.437 (-0.065 / +0.077) m2s-1
C0 = 0.095 ± 0.008 cm-2
C1 = 0.664 ± 0.049 cm-2
C0, C1 Fixed
log D = -12.957 (-0.044 / +0.049) m2s-1
C0 = 0.090
C1 = 1.490
[OH] (cm-2)
x (mm)
SC31-3b_3543
C0, C1 Variable
log D = -11.585 (-0.665 / +0.000) m2s-1
C0 = -0.223 ± 1.437 cm-2
C1 = 0.924 ± 0.257 cm-2
C0, C1 Fixed
log D = -12.341 (-0.086 / +0.107) m2s-1
C0 = 0.090
C1 = 1.490
[OH] (cm-2)
y (mm)
SC31-3c_3543
C0, C1 Variable
log D = -11.388 (-0.047 / +0.053) m2s-1
C0 = 0.105 ± 0.028 cm-2
C1 = 1.475 ± 0.034 cm-2
C0, C1 Fixed
log D = -11.382 (-0.021 / +0.022) m2s-1
C0 = 0.090
C1 = 1.490
[OH] (cm-2)
z (mm)
SC31-3a_3566
C0, C1 Variable
log D = -12.580 (-0.050 / +0.057) m2s-1
C0 = 0.809 ± 0.035 cm-2
C1 = 4.589 ± 0.282 cm-2
C0, C1 Fixed
log D = -12.858 (-0.029 / +0.031) m2s-1
C0 = 0.780
C1 = 7.160
[OH] (cm-2)
x (mm)
SC31-3b_3566
C0, C1 Variable
log D = -12.131 (-0.060 / +0.070) m2s-1
C0 = 0.493 ± 0.084 cm-2
C1 = 5.931 ± 0.354 cm-2
C0, C1 Fixed
log D = -12.350 (-0.041 / +0.045) m2s-1
C0 = 0.780
C1 = 7.160
[OH] (cm-2)
y (mm)
SC31-3c_3566
C0, C1 Variable
log D = -11.391 (-0.047 / +0.053) m2s-1
C0 = 0.888 ± 0.127 cm-2
C1 = 7.158 ± 0.155 cm-2
C0, C1 Fixed
log D = -11.366 (-0.020 / +0.021) m2s-1
C0 = 0.780
C1 = 7.160
[OH] (cm-2)
z (mm)

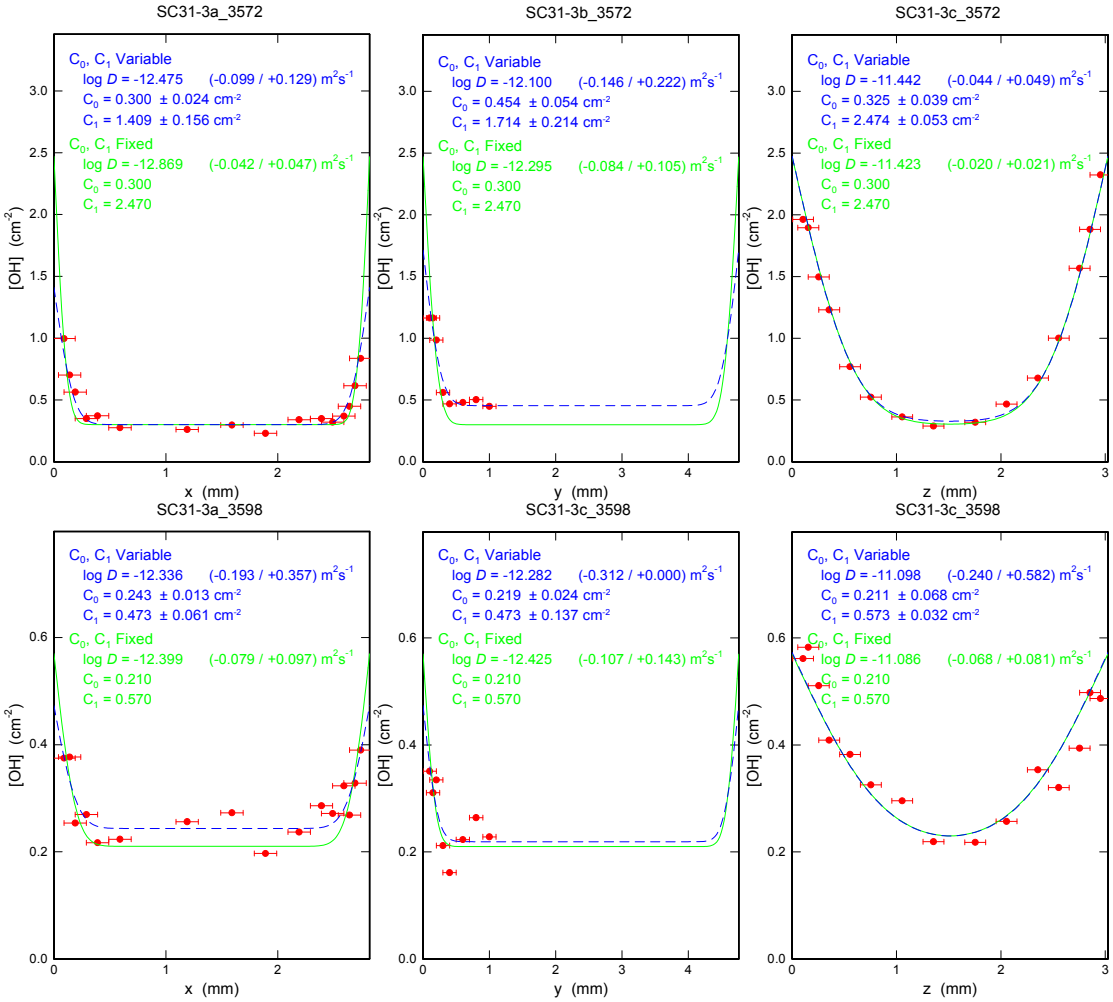
SC31-3a_3572
C0, C1 Variable
log D = -12.475 (-0.099 / +0.129) m2s-1
C0 = 0.300 ± 0.024 cm-2
C1 = 1.409 ± 0.156 cm-2
C0, C1 Fixed
log D = -12.869 (-0.042 / +0.047) m2s-1
C0 = 0.300
C1 = 2.470
[OH] (cm-2)
x (mm)
SC31-3b_3572
C0, C1 Variable
log D = -12.100 (-0.146 / +0.222) m2s-1
C0 = 0.454 ± 0.054 cm-2
C1 = 1.714 ± 0.214 cm-2
C0, C1 Fixed
log D = -12.295 (-0.084 / +0.105) m2s-1
C0 = 0.300
C1 = 2.470
[OH] (cm-2)
y (mm)
SC31-3c_3572
C0, C1 Variable
log D = -11.442 (-0.044 / +0.049) m2s-1
C0 = 0.325 ± 0.039 cm-2
C1 = 2.474 ± 0.053 cm-2
C0, C1 Fixed
log D = -11.423 (-0.020 / +0.021) m2s-1
C0 = 0.300
C1 = 2.470
[OH] (cm-2)
z (mm)
SC31-3a_3598
C0, C1 Variable
log D = -12.336 (-0.193 / +0.357) m2s-1
C0 = 0.243 ± 0.013 cm-2
C1 = 0.473 ± 0.061 cm-2
C0, C1 Fixed
log D = -12.399 (-0.079 / +0.097) m2s-1
C0 = 0.210
C1 = 0.570
[OH] (cm-2)
x (mm)
SC31-3c_3598
C0, C1 Variable
log D = -12.282 (-0.312 / +0.000) m2s-1
C0 = 0.219 ± 0.024 cm-2
C1 = 0.473 ± 0.137 cm-2
C0, C1 Fixed
log D = -12.425 (-0.107 / +0.143) m2s-1
C0 = 0.210
C1 = 0.570
[OH] (cm-2)
y (mm)
SC31-3c_3598
C0, C1 Variable
log D = -11.098 (-0.240 / +0.582) m2s-1
C0 = 0.211 ± 0.068 cm-2
C1 = 0.573 ± 0.032 cm-2
C0, C1 Fixed
log D = -11.086 (-0.068 / +0.081) m2s-1
C0 = 0.210
C1 = 0.570
[OH] (cm-2)
z (mm)

Figure B.3.5: OH concentration versus positions (x, z) along [100] and [001] of sample SC31-5. Title of each plot has the format of ”SC31-5” + ”diffusion profile direction (a or c)” + ”wavenumber”. The plot in the top row is diffusion profiles of the overall region, 3650-3200 cm^{-1}, in IR spectra along [001].

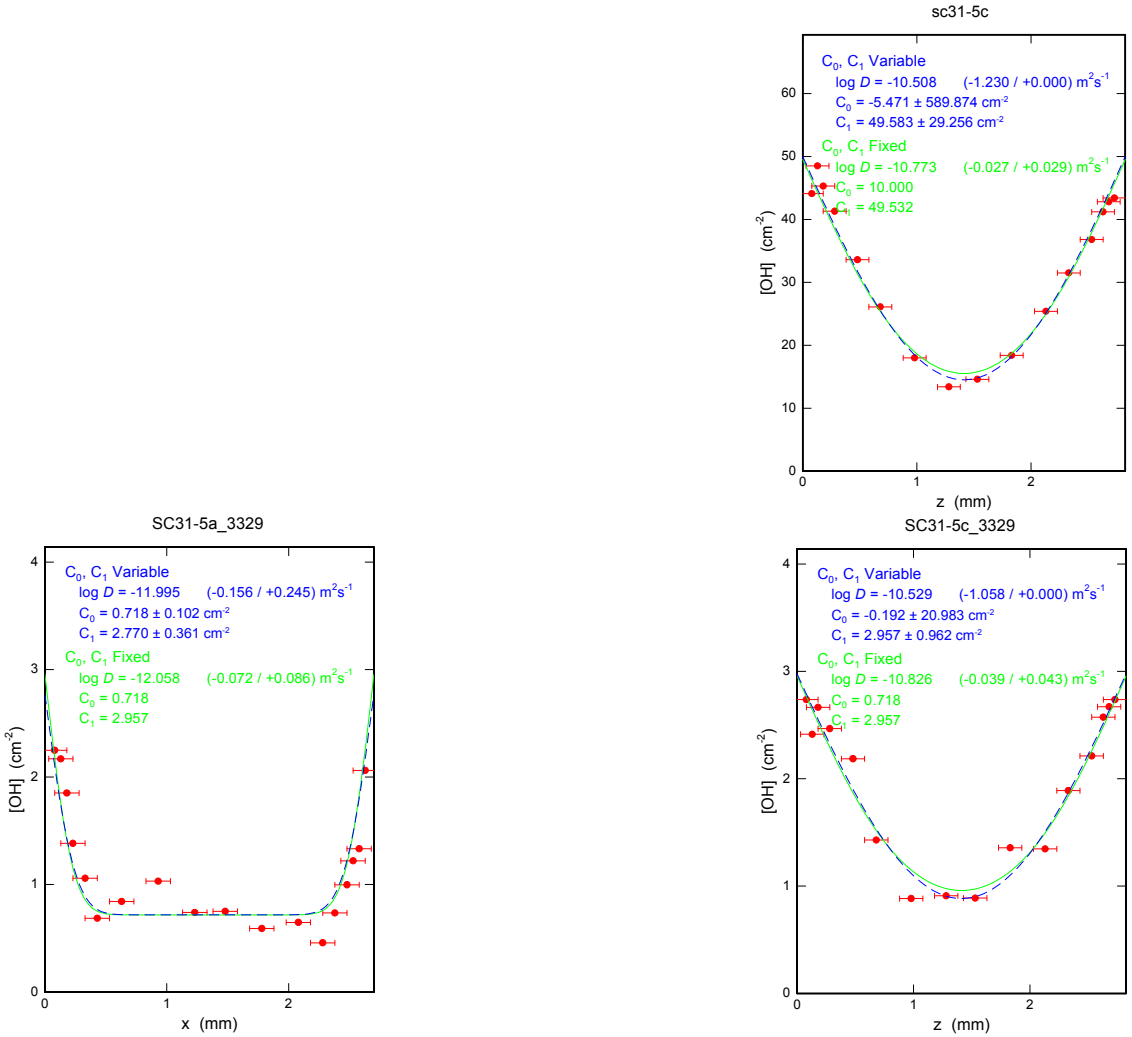

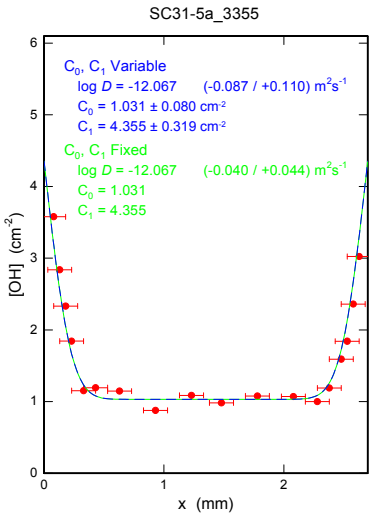
SC31-5a_3355
C0, C1 Variable
log D = -12.067 (-0.087 / +0.110) m2s-1
C0 = 1.031 ± 0.080 cm-2
C1 = 4.355 ± 0.319 cm-2
C0, C1 Fixed
log D = -12.067 (-0.040 / +0.044) m2s-1
C0 = 1.031
C1 = 4.355
[OH] (cm-2)
x (mm)

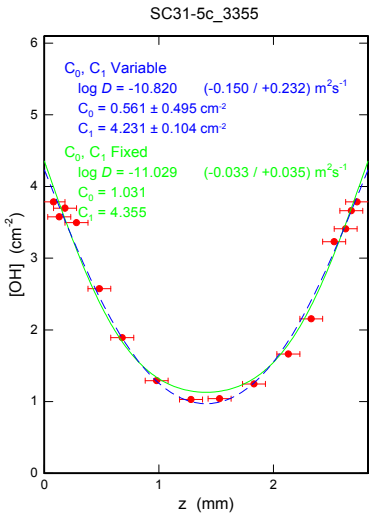
SC31-5c_3355
C0, C1 Variable
log D = -10.820 (-0.150 / +0.232) m2s-1
C0 = 0.561 ± 0.495 cm-2
C1 = 4.231 ± 0.104 cm-2
C0, C1 Fixed
log D = -11.029 (-0.033 / +0.035) m2s-1
C0 = 1.031
C1 = 4.355
[OH] (cm-2)
z (mm)

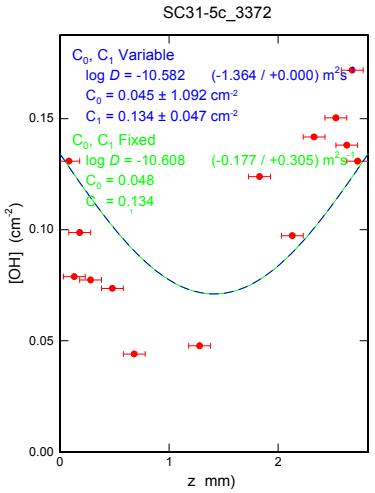
SC31-5c_3372
C0, C1 Variable
log D = -10.582 (-1.364 / +0.000) m2s-1
C0 = 0.045 ± 1.092 cm-2
C1 = 0.134 ± 0.047 cm-2
C0, C1 Fixed
log D = -10.608 (-0.177 / +0.305) m2s-1
C0 = 0.048
C1 = 0.134
[OH] (cm-2)
z mm)

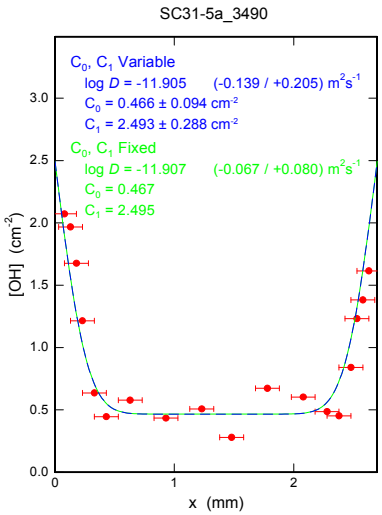
SC31-5a_3490
C0, C1 Variable
log D = -11.905 (-0.139 / +0.205) m2s-1
C0 = 0.466 ± 0.094 cm-2
C1 = 2.493 ± 0.288 cm-2
C0, C1 Fixed
log D = -11.907 (-0.067 / +0.080) m2s-1
C0 = 0.467
C1 = 2.495
[OH] (cm-2)
x (mm)

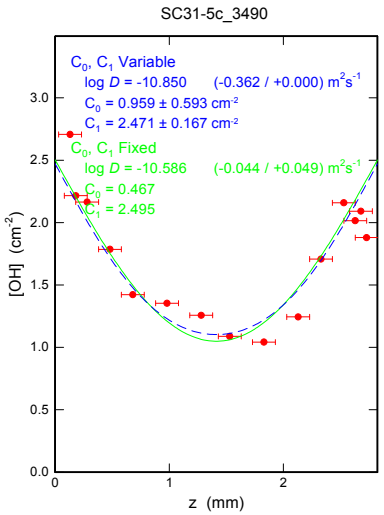
SC31-5c_3490
C0, C1 Variable
log D = -10.850 (-0.362 / +0.000) m2s-1
C0 = 0.959 ± 0.593 cm-2
C1 = 2.471 ± 0.167 cm-2
C0, C1 Fixed
log D = -10.586 (-0.044 / +0.049) m2s-1
C0 = 0.467
C1 = 2.495
[OH] (cm-2)
z (mm)

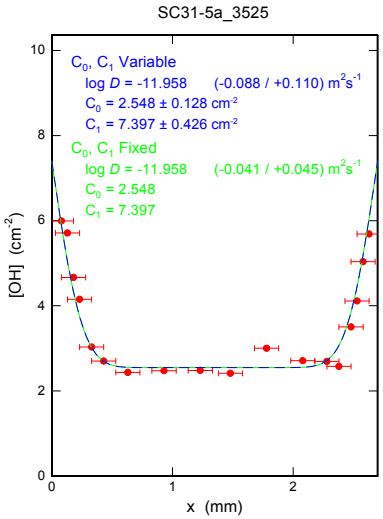
SC31-5a_3525
C0, C1 Variable
log D = -11.958 (-0.088 / +0.110) m2s-1
C0 = 2.548 ± 0.128 cm-2
C1 = 7.397 ± 0.426 cm-2
C0, C1 Fixed
log D = -11.958 (-0.041 / +0.045) m2s-1
C0 = 2.548
C1 = 7.397
[OH] (cm-2)
x (mm)

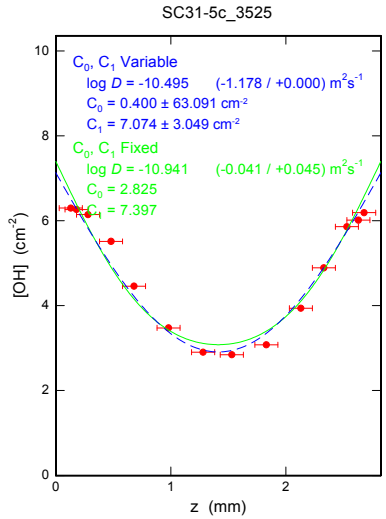
SC31-5c_3525
C0, C1 Variable
log D = -10.495 (-1.178 / +0.000) m2s-1
C0 = 0.400 ± 63.091 cm-2
C1 = 7.074 ± 3.049 cm-2
C0, C1 Fixed
log D = -10.941 (-0.041 / +0.045) m2s-1
C0 = 2.825
C1 = 7.397
[OH] (cm-2)
z (mm)

SC31-5a_3543

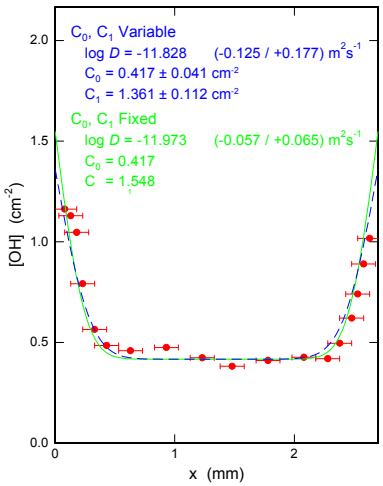

SC31-5c_3543

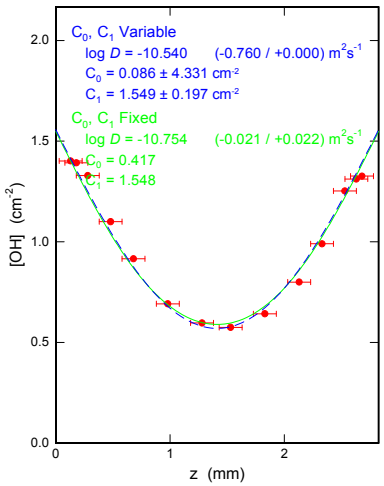

SC31-5a_3566

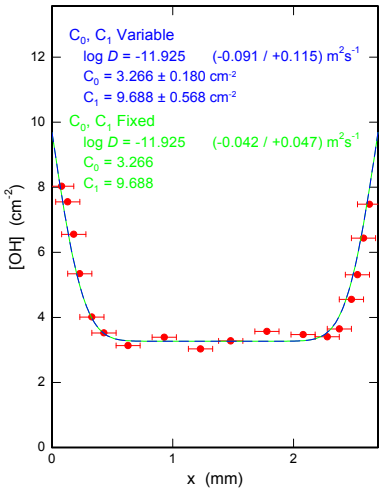

SC31-5c_3566

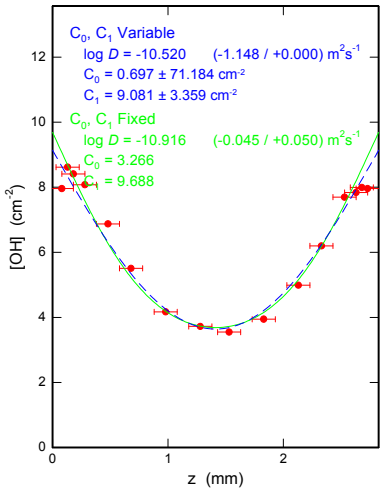

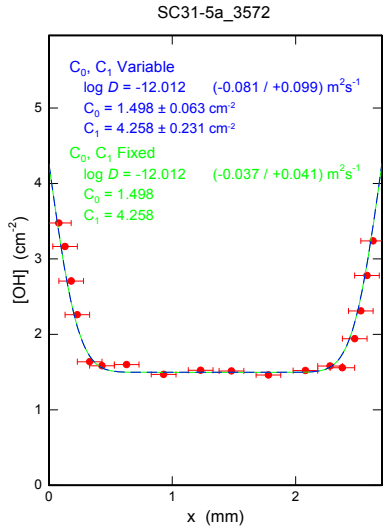
SC31-5a_3572
C0, C1 Variable
log D = -12.012 (-0.081 / +0.099) m2s-1
C0 = 1.498 ± 0.063 cm-2
C1 = 4.258 ± 0.231 cm-2
C0, C1 Fixed
log D = -12.012 (-0.037 / +0.041) m2s-1
C0 = 1.498
C1 = 4.258
[OH] (cm-2)
x (mm)

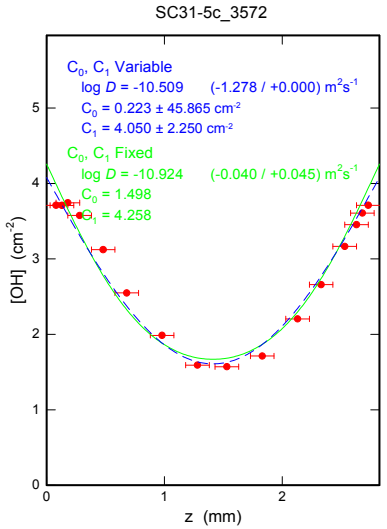
SC31-5c_3572
C0, C1 Variable
log D = -10.509 (-1.278 / +0.000) m2s-1
C0 = 0.223 ± 45.865 cm-2
C1 = 4.050 ± 2.250 cm-2
C0, C1 Fixed
log D = -10.924 (-0.040 / +0.045) m2s-1
C0 = 1.498
C1 = 4.258
[OH] (cm-2)
z (mm)

B.4 Outward chemical diffusion profiles

Figure B.4.1: OH concentration versus positions (x, z) along [100] and [001] of sample PI-1914, respectively. Plots on the left are OH concentration from separated regions, 3450-3200 (black symbols and curves) and 3650-3450 (red symbols and curves) cm $^{-1}$, versus positions on the sample; plots on the right are OH concentration from the overall region, 3650-3200 (blue symbols and curves) cm $^{-1}$, versus positions on the sample.

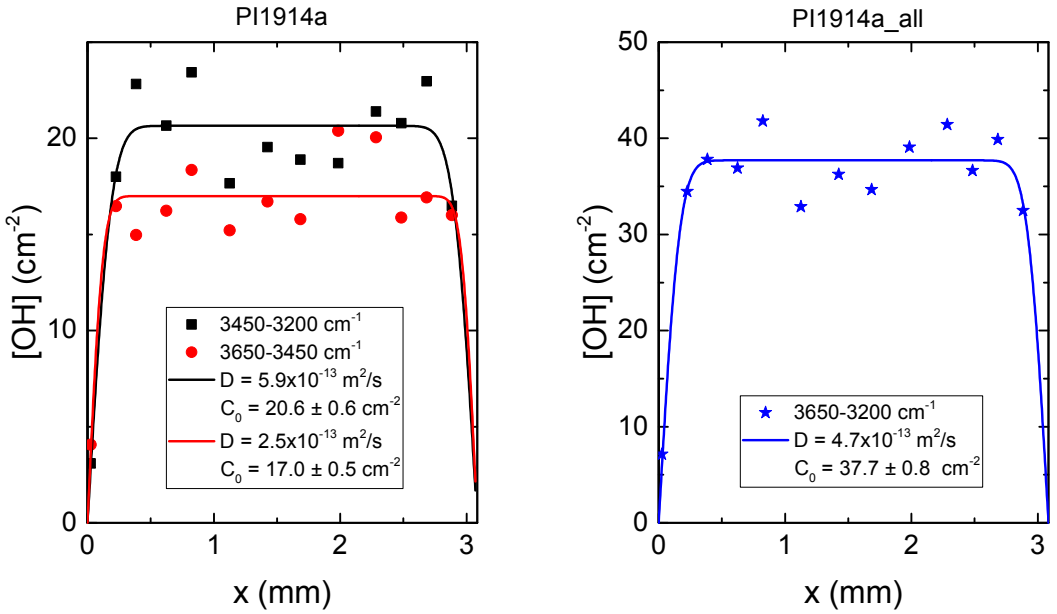

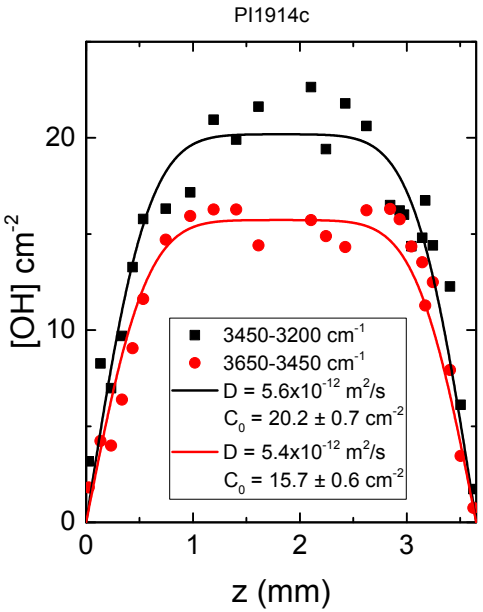
PI1914c
[OH] cm-2
z (mm)
3450-3200 cm-1
3650-3450 cm-1
D = 5.6x10-12 m2/s
C0 = 20.2 ± 0.7 cm-2
D = 5.4x10-12 m2/s
C0 = 15.7 ± 0.6 cm-2

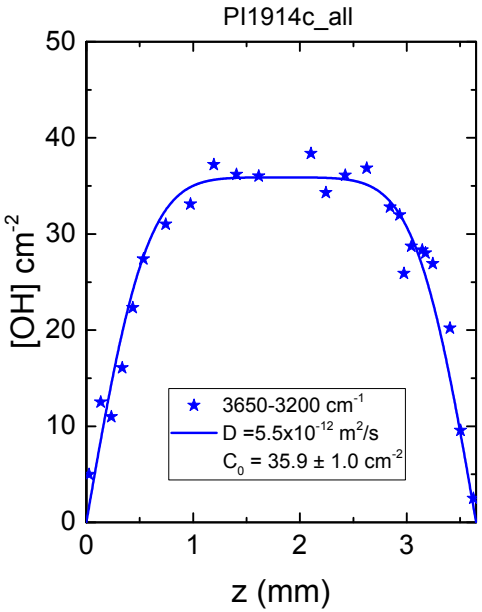
PI1914c_all
[OH] cm-2
z (mm)
3650-3200 cm-1
D =5.5x10-12 m2/s
C0 = 35.9 ± 1.0 cm-2

Figure B.4.2: OH concentration versus positions (x, z) along [100] and [001] of sample PI-1918-1, respectively. Plots on the left are OH concentration from separated regions, 3450-3200 (black symbols and curves) and 3650-3450 (red symbols and curves) cm $^{-1}$, versus positions on the sample; plots on the right are OH concentration from the overall region, 3650-3200 (blue symbols and curves) cm $^{-1}$, versus positions on the sample.

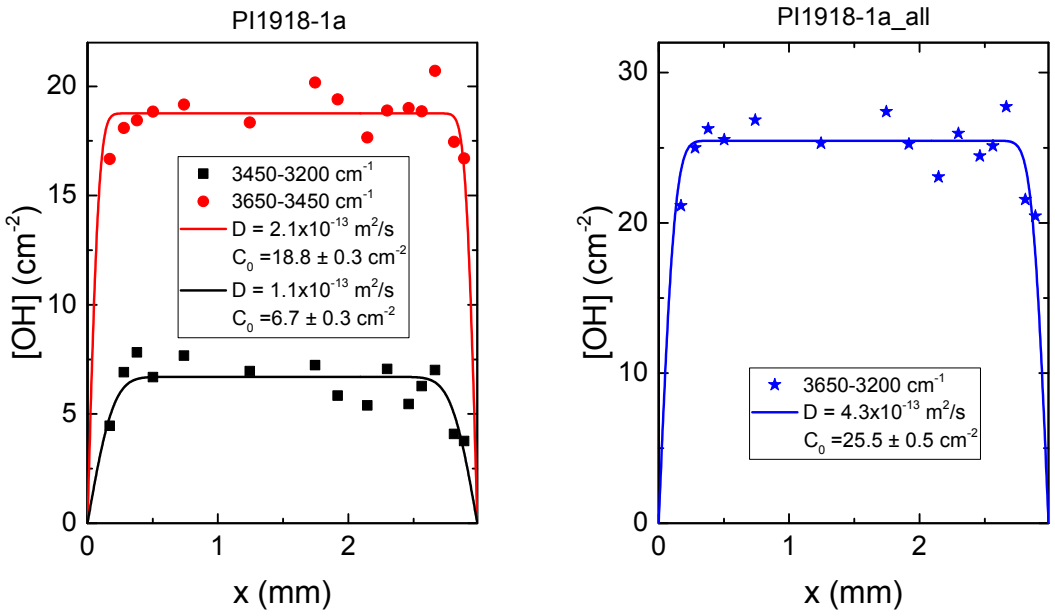

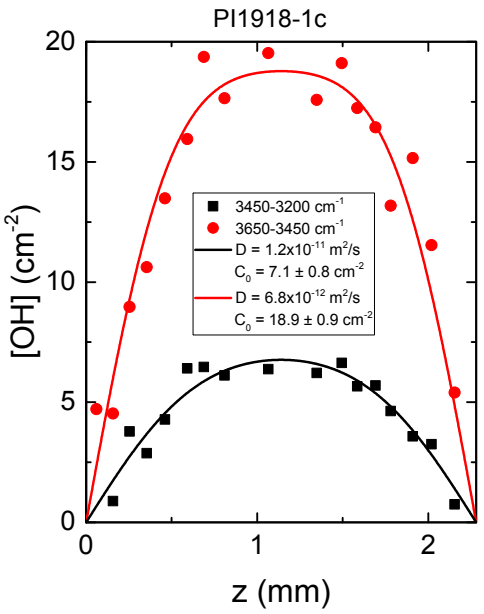
PI1918-1c
[OH] (cm-2)
z (mm)
3450-3200 cm-1
3650-3450 cm-1
D = 1.2x10-11 m2/s
C0 = 7.1 ± 0.8 cm-2
D = 6.8x10-12 m2/s
C0 = 18.9 ± 0.9 cm-2

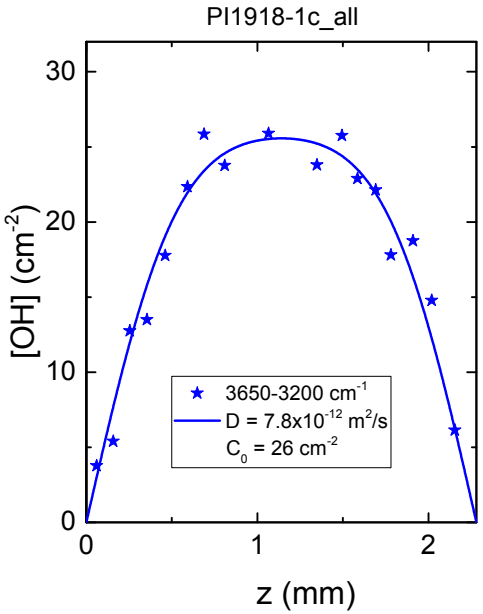
PI1918-1c_all
[OH] (cm-2)
z (mm)
3650-3200 cm-1
D = 7.8x10-12 m2/s
C0 = 26 cm-2

Figure B.4.3: OH concentration versus positions (x, z) along [100] and [001] of sample PI-1918-2, respectively. Plots on the left are OH concentration from separated regions, 3450-3200 (black symbols and curves) and 3650-3450 (red symbols and curves) cm $^{-1}$, versus positions on the sample; plots on the right are OH concentration from the overall region, 3650-3200 (blue symbols and curves) cm $^{-1}$, versus positions on the sample.

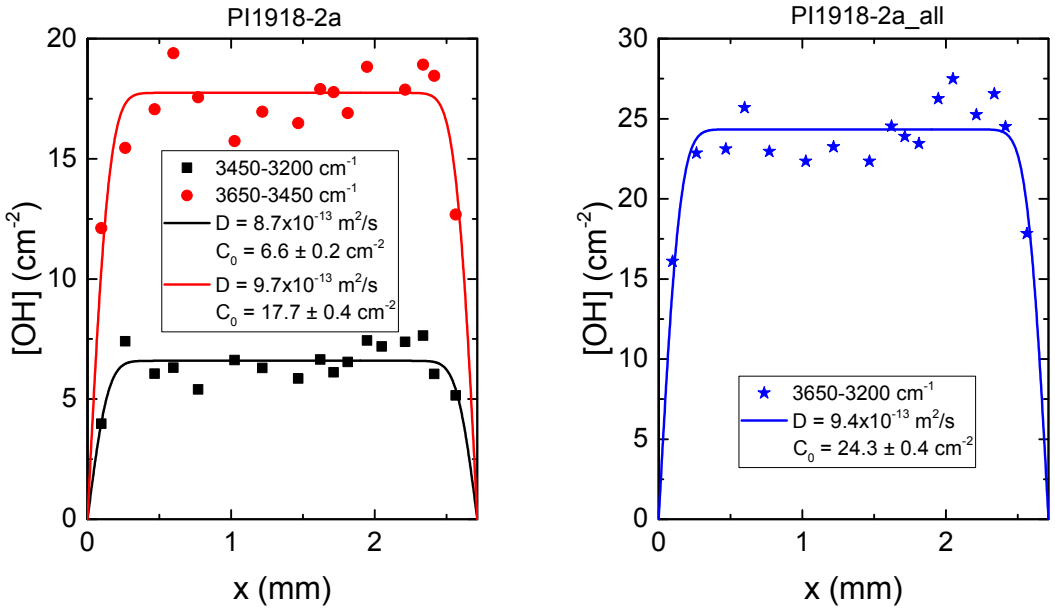

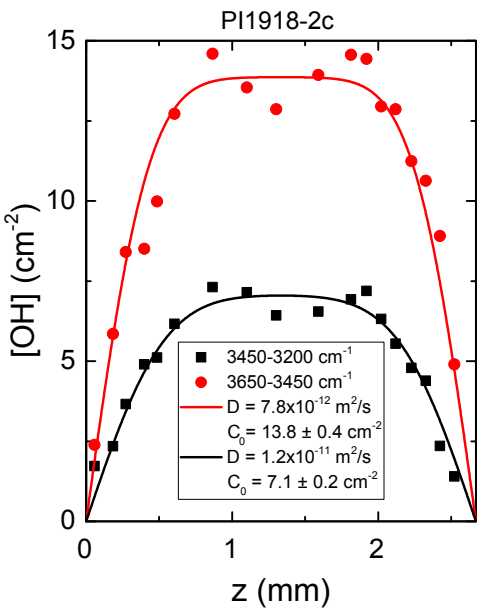
PI1918-2c
[OH] (cm-2)
z (mm)
3450-3200 cm-1
3650-3450 cm-1
D = 7.8x10-12 m2/s
C0 = 13.8 ± 0.4 cm-2
D = 1.2x10-11 m2/s
C0 = 7.1 ± 0.2 cm-2

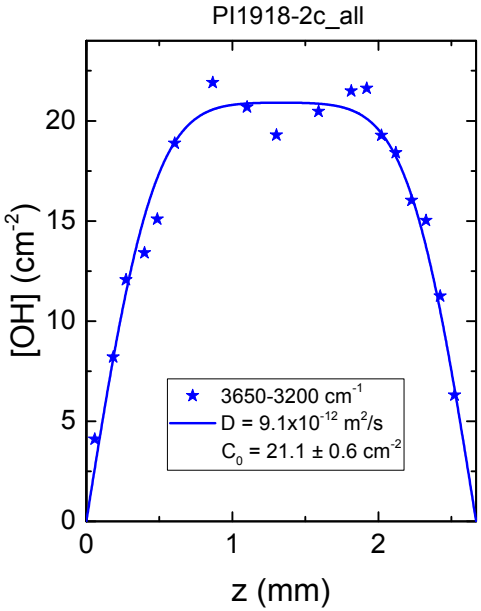
PI1918-2c_all
[OH] (cm-2)
z (mm)
3650-3200 cm-1
D = 9.1x10-12 m2/s
C0 = 21.1 ± 0.6 cm-2

Figure B.4.4: OH concentration versus positions (x, z) along [100] and [001] of sample PI-1918-3, respectively. Plots on the left are OH concentration from separated regions, 3450-3200 (black symbols and curves) and 3650-3450 (red symbols and curves) cm $^{-1}$, versus positions on the sample; plots on the right are OH concentration from the overall region, 3650-3200 (blue symbols and curves) cm $^{-1}$, versus positions on the sample.

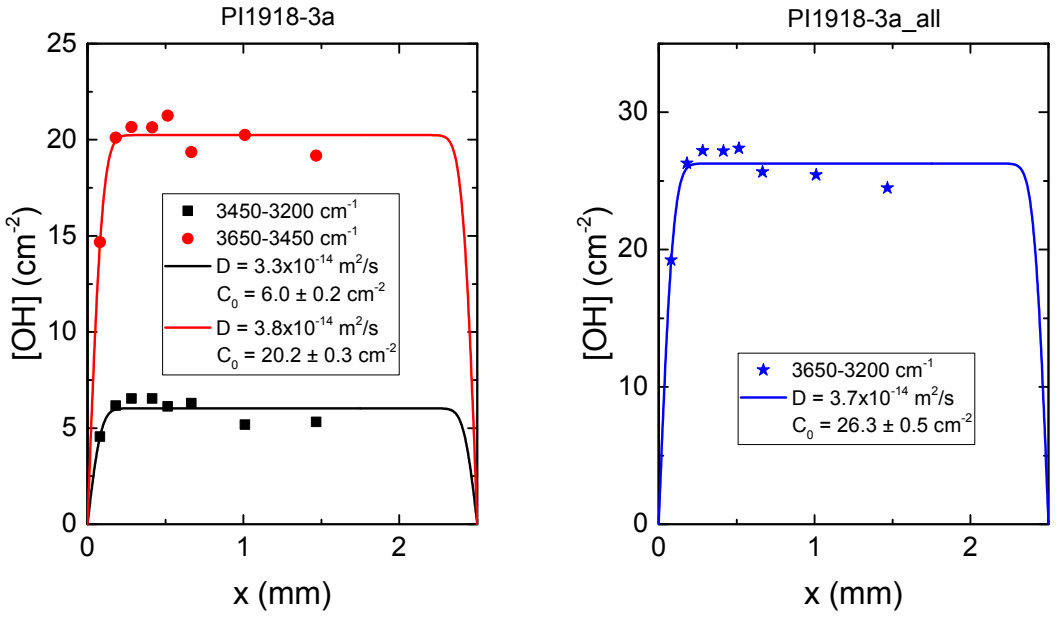

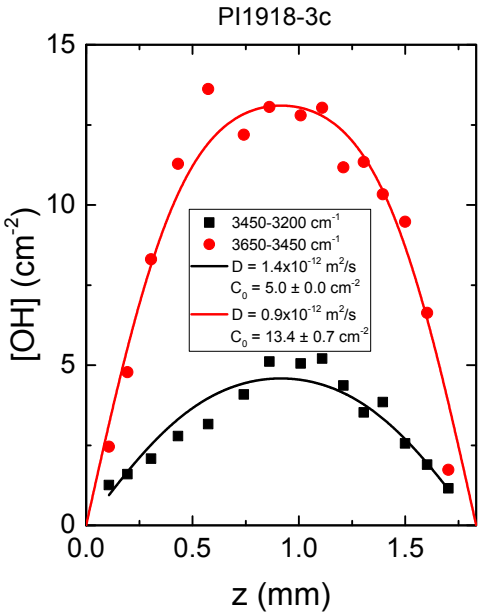
PI1918-3c
[OH] (cm-2)
z (mm)
3450-3200 cm-1
3650-3450 cm-1
D = 1.4x10-12 m2/s
C0 = 5.0 ± 0.0 cm-2
D = 0.9x10-12 m2/s
C0 = 13.4 ± 0.7 cm-2

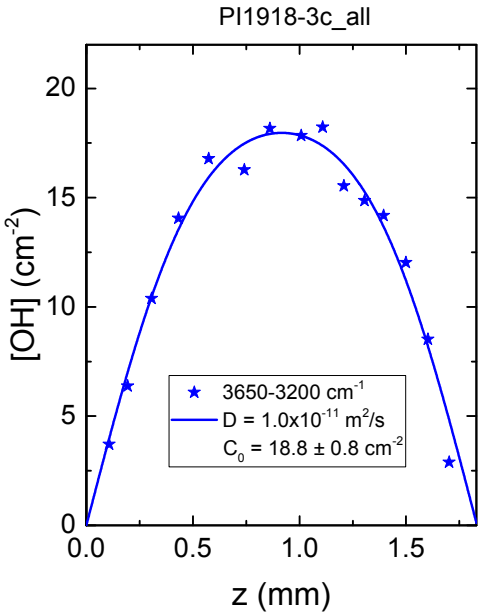
PI1918-3c_all
[OH] (cm-2)
z (mm)
3650-3200 cm-1
D = 1.0x10-11 m2/s
C0 = 18.8 ± 0.8 cm-2